DEVICE LEVEL VACUUM PACKAGED MICROBOLOMETERS ON FLEXIBLE SUBSTRATES

by

AAMER MAHMOOD

Presented to the Faculty of the Graduate School of

The University of Texas at Arlington in Partial Fulfillment

of the Requirements

for the Degree of

DOCTOR OF PHILOSOPHY

THE UNIVERSITY OF TEXAS AT ARLINGTON

August 2006

سُبْحَانَكَ لَا عِلْمَ لَنَا إِلَّا مَا عَلَّمْتَنَا إِنَّكَ أَنتَ الْعَلِيمُ الْحَكِيمُ

Glory to Thee: of knowledge we have none, save what Thou hast taught us: in truth it is Thou Who art perfect in knowledge and wisdom
(The Holy Quran 2:32)

وَفَوْقَ كُلِّ ذِي عِلْمٍ عَلِيمٌ

And over all endued with knowledge is one, the All-Knowing
(The Holy Quran 12:76)

To Samia

ACKNOWLEDGEMENTS

All praise and thanks to Allah almighty, the creator and sustainer of all creation. Peace and blessings upon his messenger Muhammad.

I am very grateful to my Ph.D. supervisor, Prof. Donald P. Butler for his guidance and support during the course of this work. His mild disposition and sound knowledge provided an atmosphere that fostered initiative in experimentation and research. I am especially thankful to Prof. Zeynep Çelik-Butler for her help and guidance. Her insightful comments and critique go a long way in improving the quality of my work.

I am thankful to the members of my dissertation committee; Prof. W. Alan Davis, Prof. Meng Tao and Prof. Dereje Agonafer for their time and effort in reviewing my work and making useful suggestions. I thank my colleagues in the microsensors and noise and reliability laboratories for their help and companionship. I am eternally indebted to my parents Mian Noor Mehmud and Haseen Mehmud for their support and prayers.

I would like to make a special mention of my wife Samia Khanum for her patience, support, help and encouragement during the course of my work. Her companionship has mitigated the enormity of many a daunting task.

July 10, 2006

ABSTRACT

DEVICE LEVEL VACUUM PACKAGED MICROBOLOMETERS

ON FLEXIBLE SUBSTRATES

Publication No. _____

Aamer Mahmood, Ph.D.

The University of Texas at Arlington, 2006

Supervising Professor: Dr. Donald P. Butler

Micromachined microbolometers on flexible substrate have been fabricated and characterized. Liquid polyimide PI5878G made by HD Microsystems has been used to form the flexible substrate. Semiconducting Yttrium-Barium-Copper-Oxide (commonly referred to as YBCO) is the temperature sensitive material. These detectors are supported by thin micromachined layers of silicon nitride on flexible polyimide PI5878G. The devices were characterized for temperature dependent resistance (R(T)), the temperature coefficient of resistance (TCR, α), responsivity $(\Re)$, detectivity (D*) and thermal conductance (G_{th}). A typical device had a resistance of 3.76 MΩ and a TCR of -2.63 %/K at 301 K. The measured thermal conductance was $G_{th} = 5.61 \times 10^{-7}$ W/K. The device displayed a voltage responsivity of 9.2×10^2 V/W. The responsivity

improved to 7.4×10^3 V/W when the same device was measured in vacuum, pointing to good thermal isolation because of the micromachining. The maximum recorded detectivity of the device was 6.6×10^5 cmHz$^{1/2}$/W. The effect of substrate heating on the detector response was also investigated and found to be negligible.

A new device-level vacuum-packaging scheme has been introduced in this work. Devices were fabricated on a rigid silicon substrate as well as a flexible polyimde substrate, packaged and characterized. A TCR of -3.7 %/K was measured. With a voltage bias of 10.1 V across the bolometer, a responsivity of 61.3 μA/W at an optical modulation frequency of 5 Hz was measured. The corresponding detectivity was 5.2×10^4 cmHz$^{1/2}$/W. The device on flexible polyimide substrate had a measured thermal conductance $G_{th} = 3.7 \times 10^{-6}$ W/K while the device on rigid silicon substrate had a measured thermal conductance $G_{th} = 1.1 \times 10^{-6}$ W/K, one hundred and eighty days after fabrication. These values compare well with the calculated minimum G_{th} using an analytic model as well as a numeric FEM model. The low thermal conductance of the devices after a lapse of six months points to an intact vacuum cavity containing functional microbolometers.

The development of a tunable infrared spectrometer for near and mid infrared region application has also been presented. A Fabry Perot cavity based design was analyzed using finite element method based simulations for optical and structural feasibility.

TABLE OF CONTENTS

LIST OF ILLUSTRATIONS

LIST OF TABLES

CHAPTER 1

INTRODUCTION

1.1 Electronics and systems on flexible substrates

At present most of the world of electronics is dominated by rigid components based predominantly on silicon. There has been considerable interest in the development of flexible electronics and systems and the current trends in the development of electronic systems point to a very important role for flexible components and systems in the development of highly integrated systems. Whether flexible electronics will replace all rigid electronics in the future has to be seen, but what is certainly very interesting and exciting is the opening up of entirely new applications that combine the features of traditional electronics as we know them consisting of transistors, LEDs, solid state sensors, detectors, energy cells, actuators with the freedom of design, flexibility and low cost of plastics. Numerous advantages of flexible electronics include freedom of design, compact portable products, cost-effective production and assembly, eco friendly materials and processes and software based printable ICs. Polytronics (Polymer+electronics), a new term describing such systems is coming into vogue[1]. Advances in integrated electronics and the advent of MEMS promises complete miniature systems comprising sensors, electronics, actuators

and power sources within the same chip. Flexible substrate systems and electronics can be made to conform to non planar host surfaces. This is useful not only for new systems designed from scratch but also for upgrades to existing platforms where at times a rigid add-on might have an adverse effect of the system performance e.g. the addition of a rigid module to a micro UAV will affect the aerodynamics of the system, or a surgeons gloves should not become rigid by adding on electronics and/or sensors.

There are two main types of flexible circuits in this realm. The first one being inorganic active materials like thin Si based integrated circuits. These are achieved chiefly by wafer thinning by employing backside grinding after the electronics have been fabricated on the front side by conventional CMOS fabrication techniques. To avoid damage to integrated circuits on the front of the wafer, a protective tape is laminated to the front side[2,3]. Ever since the discovery and development of conductive polymers by Heeger, Macdiarmid and Shirakawa in 1977 for which they were awarded the noble prize in 2000, the relatively newer area of conductive and semiconductive plastic materials is also developing fast[1]. A sub class of flexible systems overlapping the aforementioned areas employs flexible polymer substrates to host inorganic active elements.

Flexible electronic paper has been reported[4] by the electronics giant Philips. The paper is made of organic electronics printed on to a plastic film that can be folded up to a diameter of 2cm. The paper is ~ 300 μm thick and employs 'electronic ink' developed by E Ink. The refresh time for the e-paper is ~1s which is far too low to display moving objects but good enough to serve as a fully updatable newspaper.

The integrated module board (IMB) technology being developed at the Helsinki University of Technology enables very high density integration of active and passive components onto organic substrates[5]. This technique employs inorganic active elements thinned down to 50 μm embedded into a flexible substrate using elastic molding polymer. A photodefinable polymer has been used as the dielectric layer and high density wiring and interconnections have been done using electroless copper deposition.

The interest in wearable sensors in 'smart clothing' is another noteworthy catalyst in the development of flexible systems. An interesting development has been dual-band and wide-band antennas on clothing[6]. The small patch antennas are tuned to work in the Bluetooth and UMTS neighborhoods. A planar inverted F antenna (PIFA) has been implemented on flexible substrate (cloth) to be worn on a shirt sleeve for single frequency operation at 2.45 GHz as well as dual frequency operations at 1.9 GHz and 2.2 GHz. These antennas are meant to facilitate wireless communication between different sensors and a central processor embedded in different parts of a suit.

Biomedical Microsystems or BioMEMS offer tremendous possibilities for neural prostheses because of the degree of miniaturization and system complexity that can be achieved[7]. This is all the more so when implants are a method to establish contacts to the central or peripheral nervous system. Electrodes are a key component to establish a functional electrical connection to neurons to record nerve signals as well as to stimulate them for the control of limbs and organs or to elicit sensory sensations for feeling, hearing and seeing. The need for MEMS (to achieve smaller and smarter

implants) is most obvious for example in the approach to develop a system that is totally implantable in the human eye to restore vision[8]. For extremely small applications like that, there is a need for thin flexible substrates with a high number of electrode sites to obtain sufficiently high spatial selectivity and methods of encapsulation but not to alter the size of implant too much to match anatomical constraints.

Silicon based micro systems have been established as a research tool in the neurosciences to investigate the central nervous system (CNS)[9,10,11]. Flexible micromachined electrodes have been used to interface different levels of the central and peripheral nervous systems. Polyimide substrate was used to develop epidural[12] and intracortical recording arrays with compartments that deliver bioactive substances[13]. Modular, flexible biomedical microsystems have been developed at IBMT, Germany[7]. Different systems reported in the literature include a cuff electrode with integrated multiplexer circuitry and standard implantable cables representing a combination of microtechnology with precision mechanics; a sieve electrode used as an implant in peripheral nerve regeneration studies demonstrated the next level of integration density, but still uses cable connections. Work on a vision prosthesis that is completely implantable in the eye with a wireless link for energy supply and data transmission has also been reported[7]. System design, hybrid assembling technology and flexible multilayer encapsulation using parylene and silicone are the key components for creating a new generation of neural prostheses for complex and challenging new applications.

The development of organic optical sensors on a flexible substrate to form a compound eye has been reported[14]. The sensor was composed of a compound eye shaped flexible organic image sensor composed of a flexible micro-lens array and pantacene-based organic photo sensors on Kapton EN100 flexible polyimide substrate.

Electrically conductive elastomer (CE) composites show piezoresistive properties when deformation is applied. Such CE can be integrated into fabric or other flexible substrates to be used as a strain sensor[15] finding potential applications in biomechanical analysis to detect posture of a subject. The long transient time of the polymer however remains a limitation that forces complex signal analysis to extract information.

Wireless sensor nodes on flexible substrates have also been reported. As a technology demonstrator, Cu circuits on Si substrates thinned down to 50 μm have been fabricated and diced to be pasted on to polyimide ranging from 3 – 25 μm polyimide. The polyimide is then folded to form a three dimensional structure. Structures 450 μm thick with a foot print of 19 mm x 7 mm have been created and tested for use as wireless sensor modules[16].

Different semiconductor materials like CdSe, CdS, PbS, PbSe and Cu_xS films have been developed to be used on flexible substrates in different roles in "sensitive skins" – a flexible substrate housing different sensors. The films were deposited chemically using water based salt solutions at near room temperature although thermal treatment did have a marked effect on the film properties[17]. In the same area of flexible sensors, the successful development of poly-Ge based thermopiles on plastic has been

reported. Thermopiles are arrays of thermocouples that employ the Seebeck effect to measure temperature by the voltage developed across a junction. Polyethylene-terephthalate (PET) has been used as the flexible plastic substrate. The Ge film is deposited using electron beam evaporation and crystallized by annealing at temperatures between 120°C to 175°C which is within the thermal budget provided by PET as against an annealing temperature of 600°C needed with poly-Si devices[18]. The use of a micromachined thermal imaging mesh based on a flexible Kapton substrate has also been reported[19].

For truly flexible systems, there is a requirement for flexible energy sources. This is being achieved as a spin off to improvements to power generation techniques for space applications. Photovoltaic cells are widely used for power generation in space. Despite constant improvements in efficiency, a major limitation to the current use of bulk crystal materials is low mass specific power metric (MSP) which means a low power to weight ratio. Solar cells based on thin film materials like Kapton have the potential for higher MSP at a lower cost. Novel approaches adopted and reported to improve the MSP and efficiency (η) include fabricating thin film materials on Kapton and metal foil[20] as well as stacking two cells on top of each other to more efficiently absorb solar radiation by passing through non-absorbed longer wavelength light to a narrow-bandgap bottom cell material. Such PV cells promise an efficiency of 25% in space (AM0)[21].

Solar cells made of organic semiconductors are the latest generation of solar cells to have been reported. The efficiency of these plastic solar cells has reached up to

5% and were expected to enter the commercial market by 2005[22]. Extensive efforts are currently underway to produce narrow-bandgap materials to increase the light-to-electricity conversion efficiency by harvesting more photons. Polymer based photovoltaic (PV) device production would have the advantages of light weight, easy processability on flexible substrates, semi-transparence and a choice of color of the product, cost-effective roll-to-roll printing and clean processing for environmental considerations. It has been reported that once available and space qualified, moderate to relative high efficiency thin-film cells on lightweight flexible substrates will offer significant cost and weight benefits, and may become a leading alternative to currently used crystalline silicon based systems currently being used[23].

1.2 Microbolometers on flexible substrates

The development of temperature sensors on flexible substrates is part of the strategic goal of developing the 'smart skin' – a flexible substrate hosting different types of sensors to monitor ambient temperature, pressure, humidity, air speed, acceleration etc., along with the associated electronic circuitry and power sources like solar or fuel cells. This will make flexible systems-on-chip realizable. Such systems can be used in foldable electronics, form part of smart fabrics, lead to smart packaging for non planar commodities for applications in the fields of defence and surveillance, bio-medicine, industrial monitoring and testing.

Microbolometers on flexible substrates were first reported in 2002[24]. These sensors employed Kapton sheets pasted onto Si carrier wafers as the flexible substrates. Bubble formation during the adhesion process led to non-linearities in the fabrication

process. The second generation of sensors employed spin-on polyimide. The polyimide was cured after application to a carrier Si wafer to yield a substrate layer[25]. Dayeh, Butler and Celik-Butler[26] first reported the fabrication of surface micromachined microbolometers on flexible polyimide in 2005. A variant of micromachined devices on flexible substrates, albeit supported by a nitride layer was also successfully fabricated and reported by Mahmood, Butler and Celik-Butler[27]. Most MEMS devices require vacuum packaging for optimum performance. Microbolometers are no exception and need vacuum encapsulation. Being thermal detectors, they perform best when they are thermally isolated from the ambient and preserve the heat produced in them due to incident infrared radiation. Thermal conduction is the major source of heat loss and as such a low thermal conductance from the detector to the ambient/substrate is imperative for good performance. Micromachining the detector to isolate it from the ambient and using materials with low thermal conductance serves this end. Operation in vacuum further reduces the thermal conductivity by eliminating enveloping air as a conduit of heat loss. For optimum performance microbolometers fabricated in the micro sensors laboratory at the University of Texas at Arlington had to be packaged in vacuum. In the laboratory this was done using cryostats with ZnSe optical windows. For practical applications though, this would have meant one of the vacuum packaging techniques in vogue (discussed further in chapter 3). This would have meant sacrificing or limiting flexibility. The concept of a device-level vacuum-package was explored and found feasible by Mahmood, Butler and Celik-Butler[28]. The device-level vacuum-package is grown around the microbolometer during fabrication and is believed to be the first of its

kind. Ceramic Al_2O_3 has been used as the cavity window material because of its superior optical and mechanical properties. This is also believed to be the first such use of the material. The thermal conductance G_{th} is used to gauge the quality of the vacuum inside the cavity. Thermal conductances as low as $1.1x10^{-6}$ W/K have been measured one hundred and eighty days after the devices had been fabricated signifying intact vacuum cavities.

Work on the design of a tunable infrared spectrometer in the infrared spectrum is also presented. The device employs a Fabry Perot cavity and electrostatic force for actuation to change the axial dimensions of the microcavity and hence the resonant wavelength. Theoretically, the microspectrometer will be tunable over a range of ~1 μm in the mid infrared region. This is believed to be a first development of its kind.

1.3 Organization of this document

The organization of the dissertation is as follows.

Chapter 2 provides introductory information of infrared radiation and detection. Different types of infrared detectors are presented and bolometeric detectors are discussed in detail. This is followed by a brief description of flexible substrates.

Chapter 3 gives an introduction to MEMS packaging. Traditional rigid packages as well as relatively newer schemes like wafer level packaging are discussed. This is followed by MEMS packaging requirements specifically micro opto electro mechanical systems (MOEMS) packaging requirements. The concept of device level packaging is introduced and the design of an optical pressure window made of a sputtered ceramic material is discussed.

Chapter 4 discusses practical measurement techniques used for bolometer characterization.

Chapter 5 presents work done on developing micromachined microbolometers on flexible substrtaes. The chapter spans detector fabrication carried out in the clean room and electrical, optical and thermal characterization carried out in the microsensors laboratory.

Chapter 6 covers work on device level vacuum packaged microbolometers. Detectors were made on both rigid and flexible substrates. the design issues faced and addressed are presented. The structural analyses were done using CoventorWARE®. CoventorWARE® employs finite element analysis. The thermal analysis was done using analytic techniques as well as numerically with CoventorWARE®. The design of the mask as well as process flows are presented follwed by actual fabrication and characterization of the devices.

Chapter 7 presents work done on the design of a Fabry Perot cavity based tunable microspectrometer. The structural analysis is presented which has been done using FEM. A transmission line model has been used to analyze the resonance of the Fabry Perot cavity.

Chapter 8 concludes this work. It also presents areas that need to be further investigated in the future.

CHAPTER 2

BOLOMETERS AND FLEXIBLE SUBSTRATES

2.1 Introduction

Electromagnetic radiation is one of several different ways energy is transferred from one point to another. Electromagnetic radiation is classified on the basis of wavelength or frequency, with radio and microwave engineers preferring to use frequency and optics and photo engineers preferring to use wavelength based classification. Figure 2.1 shows the electromagnetic spectrum. The classification of the electromagnetic spectrum determines the types of sources and detectors used in different parts.

Infrared radiation ranges from approximately 0.7 μm to 1 mm wavelengths, and is used to image an area based on the temperature difference of different bodies in the area/frame of interest. Physical bodies absorb and emit energy in practically a continuum of wavelengths, although in reality the spectrum is discrete albeit very finely so. The magnitude of the radiation varies in different parts of the electromagnetic spectrum and is also a function of the source temperature. The blackbody - a theoretical entity representing the perfect radiator and absorber is used as a standard to model a real radiation source or sink. Radiation from a black body follows Planck's radiation law

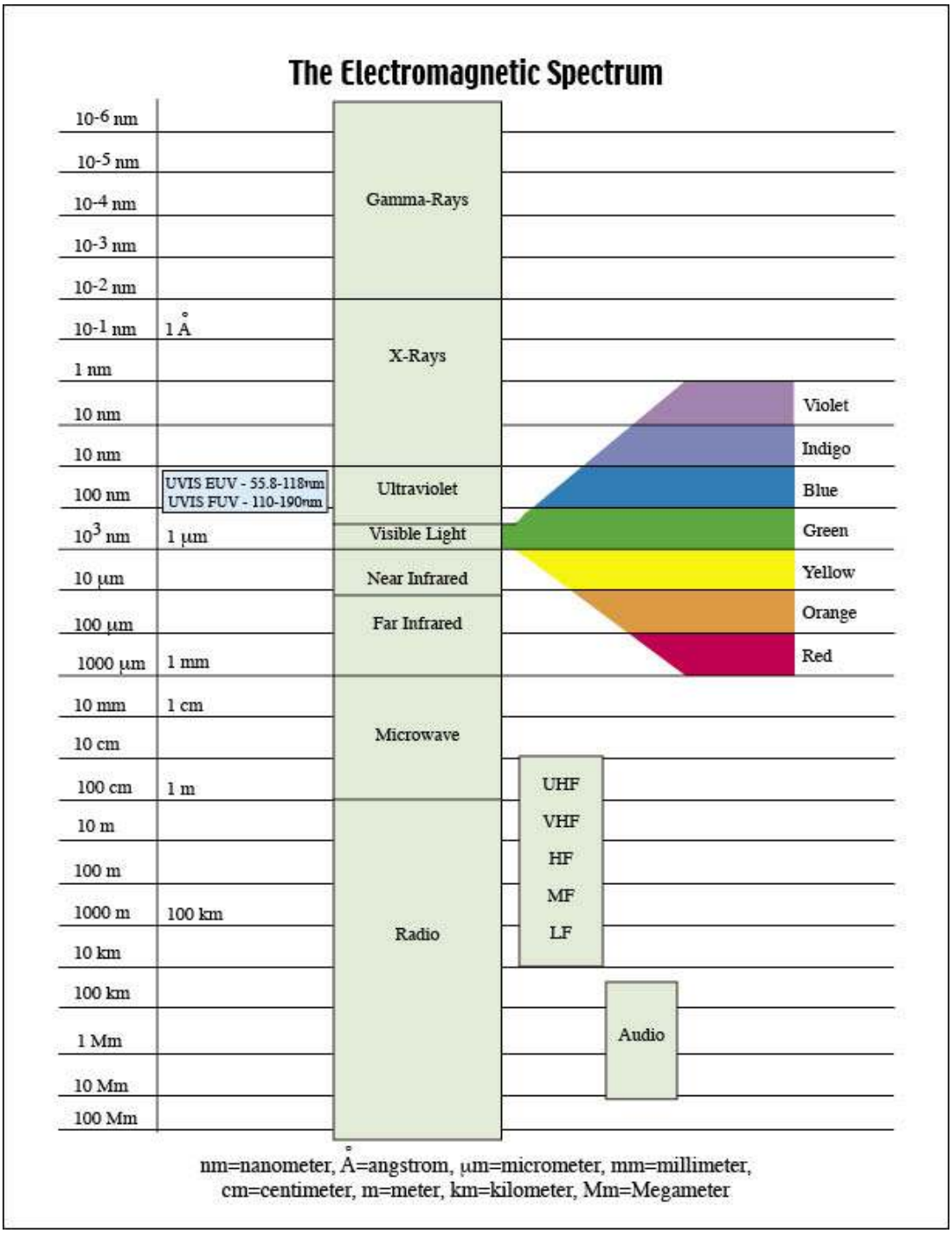

Figure 2.1 Electromagnetic spectrum. (Image reproduced with permission from Laura Bloom; Laboratory for Atmospheric and Space Physics (LASP), University of Colorado, Boulder)

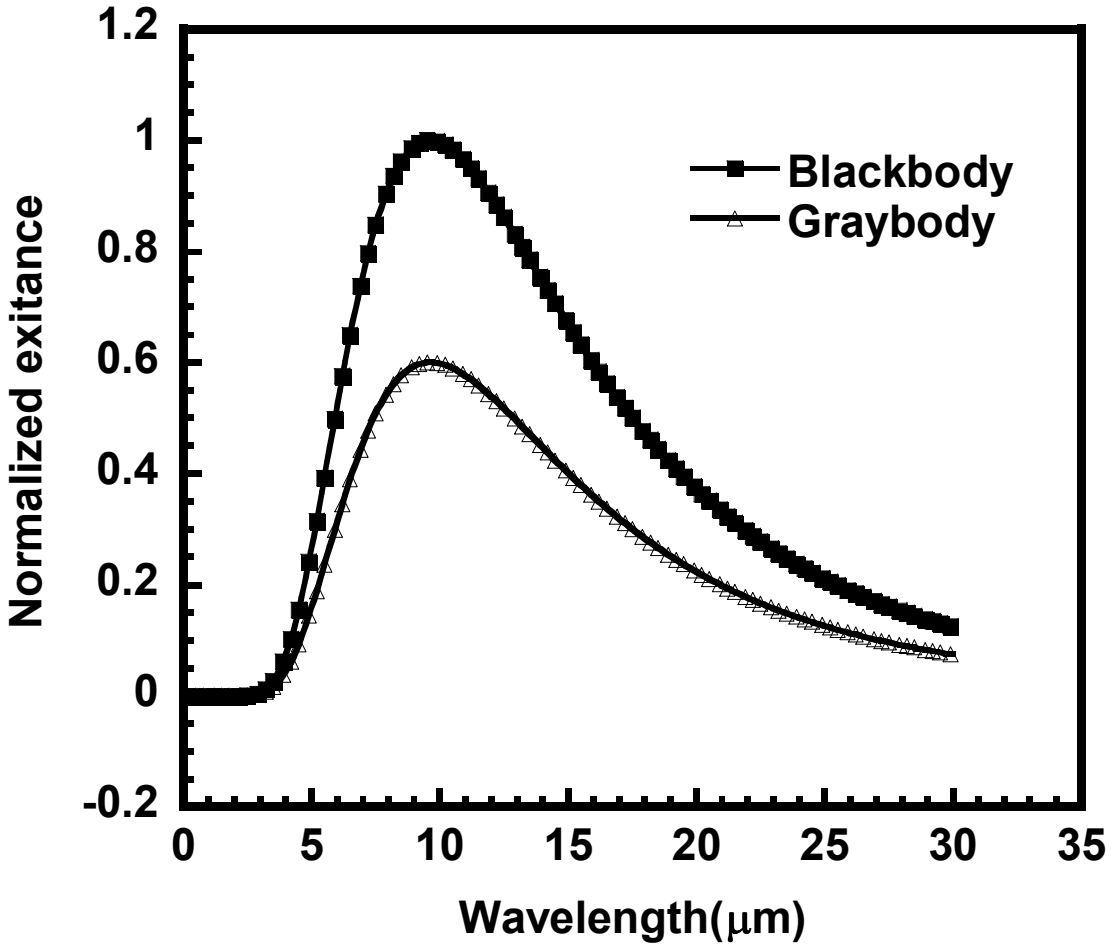

Figure 2.2 Blackbody and graybody radiation at 300 K follows Planck's radiation law.

and at 300 K peaks at 10 μm. The blackbody is an ideal radiator/absorber and a graybody can be used to represent a real life object. A graybody is a scaled down a blackbody (Figure 2.2). A more complex real life model of a radiator/absorber is the so called selective radiator/absorber. A selective radiator does not necessarily follow Planck's radiation expression.

Infrared detectors can be employed to detect bodies by detecting the infrared radiation they emit. Except for very short range applications, atmospheric attenuation is

an important factor in the transmittance of infrared radiation. There are three distinct "windows" for infrared transmission in the atmosphere; the near Infrared region that ranges from 0.7-2 μm, the mid IR region from 3-6 μm and the far IR region from 8-14 μm. Infrared detectors can be used as optical receivers for optical communication applications. Arrays of infrared detectors can be used for imaging purposes in the fields of surveillance, security, non-destructive testing, enhanced vision for motorists, industrial applications like temperature monitoring and measurement, preventive maintenance, medical imaging, military applications like night vision goggles and weapon sights.

2.2 Infrared detectors

There are two main types of infrared detectors, a) photon detectors and b) thermal detectors. Photon detectors work on the principle of an incident photon interacting with the detector crystal lattice to liberate a charge carrier. The current due to the charge carriers is a measure of the incident photons. Photon detectors have a fast response time but have a narrow spectral bandwidth. These detectors perform best when operated at low temperature. Thermal detectors work on the principle of the incident infrared energy causing the detector temperature to change. The change in temperature causes some measurable detector property like the electrical resistance or capacitance to change. This change is a measure of the incident radiation. Thermal detectors are slow but are spectrally broadband detectors and can be operated at room temperature.

2.2.1 Photon detectors

Photon detectors detect light by the direct interaction of incident photons with the crystal lattice of the detector. The photo emission causes the detector properties like resistance, inductance, voltage and current to change. These changes can be detected and measured with associated circuitry. The quantum efficiency η_{quant} is an important parameter in photon detection mechanism and is the material efficiency of converting an incident photon into an electron. It does not include any subsequent electron gain mechanisms in the material although the absorptance, scattering and reflectance as well as the recombination in the material are taken into account[29]. η_{quant} ranges from 0-1, 1 being an ideal photo sensor. The probability of a photoelectron being released only exists if the photon interacts with the detector crystal lattice; hence the smaller the Fresnel reflectance from a material, the greater the absorptance and η_{quant}. The energy of a photon is related to its wavelength as

$$E = \frac{hc}{\lambda} \tag{2.1}$$

Where h is the Planck constant = $6.6\text{x}10^{-34}$ J s , c is the speed of light = $3\text{x}10^{8}$ m/s and λ is the wavelength. To liberate an electron in the detector crystal lattice, the energy transferred to the material must be at least equal to the band gap energy E_g. For photo generated electrons, this places an upper limit on the wavelength of the incident photon as the cut off wavelength λ_c

$$\lambda_c \leq \frac{hc}{E_g}$$

Theoretically it is possible to design photon detectors for different wavelengths by engineering the band gap energy with different semiconductor material combinations and doping concentrations.

The population of electrons in a material follows $\exp(-E_g/kT)$, $k = 1.38 \times 10^{-23}$ J/K being the Boltzmann's constant and T being the temperature in Kelvin). For materials with small band gap energies, the electron population is large at any fixed temperature T. This electron population causes "dark current" - current due to thermally generated electrons and not due to photo electrons. To keep the dark current to a minimum, the temperature of the device must be reduced. Cryogenic cooling is thus essential for the operation of photon detectors, especially for long wave detectors. Different types of photon detectors include photovoltaic detectors or photodiodes (a photo sensitive p-n junction), photoconductors in which the conductance is directly proportional to the photon flux and photo emissive detectors in which photo generated electrons contribute to the external current flowing in the circuit. Photon detectors have very low time constants and have very fast response time. They have a small bandwidth and need to be cryogenically cooled especially for longer wavelength applications.

2.2.2 Thermal detectors

Thermal detectors react thermally to optical radiation. The incident eletromagnetic radiation causes the temperature of the detector to rise. The rise in temperature causes some property of the detector to change that can be measured using associated electronic circuitry. Different types of thermal detectors respond differently

to the change in temperature e.g. in bolometers; the resistance of the detector changes with temperature; in pyroelectric detectors, the capacitance of the detector changes; in thermocouples, the voltage across the detector changes; in Golay cells, there is a mechanical displacement of a membrane as a result of the change in temperature and in case of superconducting detectors, the device resistance changes. Thermal detection is a two tier process in that the temperature of the detector changes after absorbing the infrared radiation.

Conservation of energy for a body in thermal equilibrium with the ambient dictates that

$$\phi_{incident} = \phi_{absorbed} + \phi_{reflected} + \phi_{transmitted} \tag{2.2}$$

where $\phi_{incident}$ is the flux incident upon the detector, $\phi_{absorbed}$ is the flux absorbed in the detector material, $\phi_{reflected}$ is the flux reflected from the detector surface due to Fresnel reflection and $\phi_{transmitted}$ is the flux transmitted through the detector without being absorbed. Normalizing the equation with respect to $\phi_{incident}$ yields

$$a + r + t = 1 \tag{2.3}$$

where $a = \phi_{absorbed} / \phi_{incident}$ is the absorptance, $r = \phi_{reflected} / \phi_{incident}$ is the reflectance and $t = \phi_{transmitted} / \phi_{incident}$ is the transmittance. For an opaque body (transmittance = 0), there can only be absorptance and reflectance. Due to the nature of thermal detectors, the maximum energy that can be captured is desirable. For this purpose, the reflectance should be low and the absorptance as high as possible. The reflectance is maximum

when the scattering surface is smooth and polished. It can be minimized with a matte finish like that of an amorphous material.

Kirchoff's law equates the spectral absorptance a and emissivity ε, i.e. integrated over the entire electromagnetic spectrum.

$$a = \varepsilon \tag{2.4}$$

Emissivity is a material property defined as the ratio of the exitance of a real body to that of a black body at the same temperature. The exitance is the power per unit area leaving a surface. Mathematically, spectral exitance is

$$M(\lambda, T) = \frac{2\pi hc^2}{\lambda^5 (\exp(\frac{hc}{\lambda kT}) - 1)} \tag{2.5}$$

Where λ is the wavelength and T is the absolute temperature.

Materials with high emissivity are thus more suitable detector materials. Surface properties such as ε depend upon the material and do not change rapidly over the spectrum. Thermal detectors are thus broadband sensors and have a very wide spectral response up to ~100 μm wavelength. Due to the detection mechanism though, they have a slower response time compared to photo detectors.

2.3 Bolometers

A bolometer is a type of thermal detector. The resistance of a bolometer is heat sensitive. Being a thermal detector, the absorption and preservation of heat determine the sensitivity of the bolometer and the rate of heat transfer is an important factor in determining the speed of the thermal detection process. Reducing the thermal mass of

the detector serves to this end since a detector with a small thermal mass will heat up faster.

Making microbolometers – small bolometers 40 x 40 μm^2 in size - suspended above the substrate serves to reduce the thermal mass and isolating the detector from the ambient to preserve heat in the detector. This is typically done by making self supported microbolometers; where a sacrificial mesa is used to elevate the detector above the substrate. After removal by micromachining, the detector is isolated from the substrate (Figure 2.3). At times, the application dictates the use of a support membrane isolated from the substrate to support a microbolometer; called the trench geometry in the present work. Trench geometry employs a nitride membrane atop a sacrificial material to support the detector. The sacrificial material is etched by surface micromachining through trenches in the support membrane to isolate the detector from the substrate (Figure 2.4)[30,31,32].

2.3.1 Working of bolometers

Once the detector element is heated above the ambient, the temperature gradient serves as the driving force for heat flow. Of the three modes of heat transfer namely, conduction, convection and radiation, convection is insignificant. Conduction and radiation are the main heat flow mechanisms in the thermal detector. Of these, conduction dominates[33]. Thermal conduction needs to be reduced and if a detector is operating with radiation being the major source of heat loss, the detector can be operated at the background noise limit – the maximum detector performance. Being separated from the substrate not only reduces the thermal mass of the detector but also

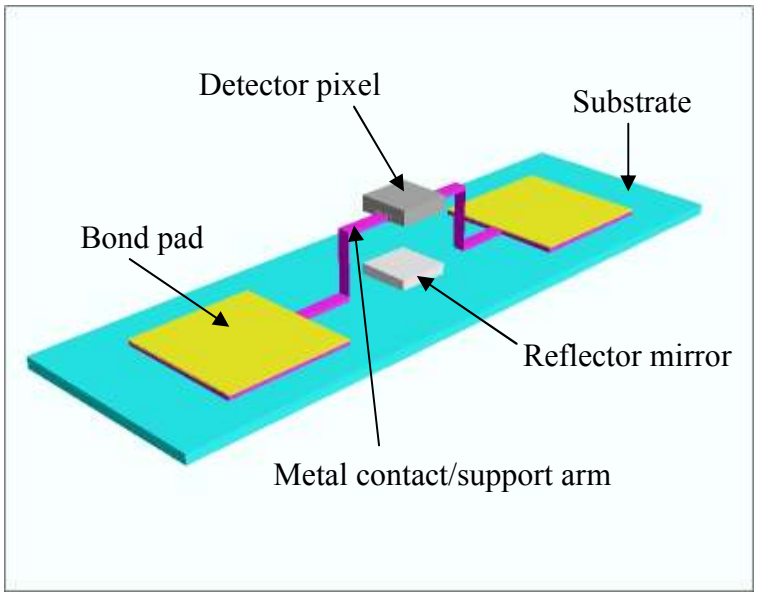

Figure 2.3 Computer generated model of self supporting micromachined microbolometer (Mesa geometry).

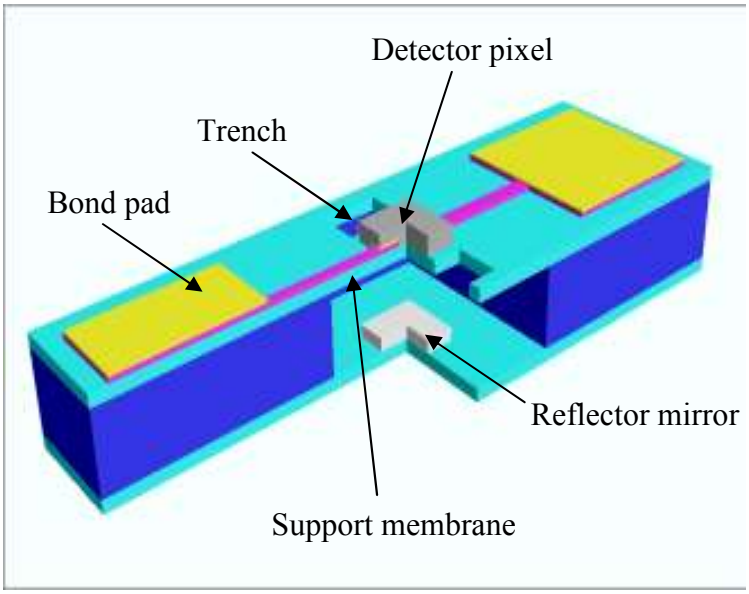

Figure 2.4 Sectioned view of computer generated model of micromachined microbolometer on support membrane (Trench geometry).

limits the loss of heat from the detector. Paths of heat loss through conduction depend on the device geometry and typically are the metal arms linking the detector pixel to the bond pads, the support layer propping up the detector and the air enveloping the detector. Judicious selection of materials with low thermal conductivity, geometry dimensions and evacuation of the air around the detector to operate the detector in vacuum greatly contribute to reducing the thermal conduction.

For the general case of a dc biased bolometer exposed to a modulated light source, the heat balance expression is

$$C_{th}\frac{dT}{dt} = \eta P_{signal} + I_b{}^2 R(T) - 2\varepsilon A_d \sigma (T^4 - T_o{}^4) - G_{th}(T - T_o) \qquad (2.6)$$

where C_{th} is the thermal mass or heat capacity (J/K), dT/dt is the rate of change of temperature, η is the optical absorption efficiency of the detector, P_{signal} is the optical signal power (W), I_b is the bias current (A), $R(T)$ is the temperature dependent device resistance (Ω), ε is the detector emissivity (assumed equal to absorptivity at all wavelengths), A_d is the detector area (cm^2), σ is the Stefan-Boltzman's constant (5.67×10^{-12} $W/(cm^2K^4)$), T is the bolometer temperature (K), T_o is the temperature of the heat sink (K), G_{th} is the thermal conductance of the detector (WK^{-1}). The term $-2\varepsilon A_d \sigma T^4$ is the optical power lost from the detector by radiation while $2\varepsilon A_d \sigma T_o{}^4$ is the optical power radiated by the ambient and absorbed by the detector. The term $G_{th}(T - T_o)$ represents the conductive heat flow. The term $I_b{}^2 R(T)$ represents the Joule

heating of the detector due to the flow of the bias current, the term ηP_{signal} shows the optical signal power absorbed by the detector. (6) can be simplified to

$$C_{th}\frac{d\Delta T}{dt}+(G_{th}+G_{rad}-\alpha_o P_I)\Delta T=\eta P_{signal}+P_I \tag{2.7}$$

Where $G_{rad}\cong 8\varepsilon A_d\sigma T_o^{\,3}$ is the radiative conductance of the material and α_o is the normalized rate of change of the detector resistance (called TCR and explained later) and P_I is the heating effect of the incident radiation. The effective thermal conductance G_{eff} takes into account the bias heating as well as the thermal radiation from the detector in addition to the thermal conductance from the detector without any bias. For a current biased bolometer, it is expressed as $G_{eff}=G_{th}+G_{rad}-\alpha_0 P_I$. The above equation reduces to

$$C_{th}\frac{d\Delta T}{dt}+G_{eff}\Delta T=\eta P_{signal}+P_I \tag{2.8}$$

This equation has a dc component as well as an ac component. The dc component is related to the dc bias of the detector and is

$$G_{eff}\Delta T_{dc}=P_I \tag{2.9}$$

which yields the change in the detector temperature due to the bias current

$$\Delta T_{dc}=P_I/G_{eff} \tag{2.10}$$

The ac component of the equation assumes a time varying signal $\exp(j\omega t)$, where ω is the chopper frequency of the incident signal, and hence a time varying change in temperature

$$C_{th}(j\omega\Delta T_{ac}) + G_{eff}\Delta T_{ac} = \eta P_{signal} \tag{2.11}$$

$$\Rightarrow \Delta T_{ac} = \frac{\eta P_{signal}}{G_{eff}(1 + j\omega\frac{C_{th}}{G_{eff}})} \tag{2.12}$$

This is usually expressed as a magnitude as

$$\Delta T_{ac} = \frac{\eta P_{signal}}{G_{eff}\sqrt{1 + (\omega\tau_{eff})^2}} \tag{2.13}$$

Where $\tau_{eff} = C_{th}/G_{eff}$ is the thermal time constant of the detector.

Thermal detectors have a high response time and are slow. Their main advantage stems from the fact that they are spectrally broadband detectors and do not need to be cooled below the surrounding temperature although cooling can serve to limit noise and improve performance.

2.3.2 Bolometer materials

In the current project, the radiation sensitive material used is semiconducting Y-Ba-Cu-O, also referred to as YBCO. It is polycrystalline to amorphous. The structural, electrical and optical properties of the material vary with the oxygen content x[34,35]. For $0.3 \le x \le 0.5$, $YBa_2Cu_3O_{6+x}$ behaves as a semiconductor. Amorphous YBCO thin films deposited on Si wafers with a buffer layer have exhibited a TCR of ~ -3.1

%/K. YBCO can be rf sputtered from a target at room temperature to yield thin films for use as microbolometers[7].

Another commonly used material is VO_x. It is extensively used in present day thermal imagers[36,37,38,39,40,41]. VO_x is deposited by low temperature ion beam sputtering of mixed oxides (VO_2, V_2O_5, V_2O_3) and undergoes a rapid thermal annealing to oxidize and achieve the desired resistance. This mixed phase results in a family of thin films that are employed in microbolometer arrays with a TCR ~ -2 %/K at 25°C. This material has low flicker noise if the metal contacts are properly applied. It has high IR absorption due to superior optical properties[42,43,44,45].

Amorphous Si is also used for bolometer applications[46,47,48]. It is deposited using standard deposition techniques. It requires high doping with impurities and should be partially crystallized in order to obtain a low tensile stress thin film layer to obtain a stable structure. This is done by applying a high temperature annealing process. The material has a TCR of -2.7 %/K at 300 K[49]. Flicker noise can be reduced with high temperature annealing[22, 23].

Poly Si doped with As, P or B is another material used for bolometric detection. It also requires a high temperature annealing process ~ 925°C for a wide range of resistivities and a desired TCR of 1-2 %/K and a mechanically stable structure[50, 51].

Poly Si-Ge alloy can be used as a bolometer material. The materials are deposited in reduced pressure chemical vapor deposition system at 600-700°C. The Si-Ge active area is doped with a moderate dose of B by ion implantation followed by high

temperature annealing. This is done to tune the TCR, thermal conductance and resistivity of the active area. The TCR is ~ 2 %/K. The reduced pressure deposition eliminated compressive stress and implies a mechanically stable structure[52,53]. This material has properties similar to poly Si but with a lower G_{th}, depending on the amount of Ge in the alloy.

Thin film metals like Ti (TCR ~ 0.2-0.25 %/K at 300 K)[54, 55], Nb (TCR ~ 0.21 %/K)[56], Pt (TCR-0.2 %/K)[57,58] have also been reported. All of these materials have a low thermal conductance G_{th} and flicker noise.

2.3.3 Noise in bolometers

Inherent to detector operation is noise in the detector. Different noise mechanisms of importance in microbolometers include the flicker $(1/f)$ noise, the Johnson noise, the temperature fluctuation noise, and the background noise.

The flicker noise is associated with the flow of direct current and is mainly caused by the traps associated with crystal defects and contamination. These traps capture and release electrons in a random fashion and the time constants associated with the process give rise to a noise signal. The flicker noise power varies inversely with frequency[59] hence the name $1/f$ noise. For microbolometers, the flicker noise is given as

$$V_{1/f} = \sqrt{\frac{\alpha_H V_{dc}^2 \Delta f}{Nf}} \tag{2.14}$$

where α_H is the Hooge parameter, V_{dc} is the dc bias voltage across the detector, Δf is the noise frequency bandwidth, N is the number of fluctuators, f is input signal optical

modulation frequency. Δf is in the vicinity of f and much smaller than f. The factor α_H / N is empirically determined.

The Johnson noise is caused by the random thermal motion of electrons and is not affected by the direct current flow in the circuit. Mathematically the Johnson noise voltage V_J across a resistance R at temperature T is given by

$$V_J = \sqrt{4kTR\Delta f} \tag{2.15}$$

where k is the Boltzman's constant and Δf is the frequency bandwidth over which the noise is measured.

The temperature fluctuation noise is noise due to the heat conduction and is a function of the thermal conduction G_{th}. Mathematically, it is expressed as

$$V_{TF} = \frac{R_V \sqrt{4kT^2 G_{th} \Delta f}}{\eta} \tag{2.16}$$

where R_v is the voltage responsivity of the material (defined in section 2.3.4), G_{th} is the thermal conductance of the detector and η is the optical absorption efficiency of the material.

The background noise is the noise associated with random fluctuations in the radiative exchange with the detector. It is given as

$$V_{BG} = \frac{R_V \sqrt{4kT^2 G_{rad} \Delta f}}{\eta} \tag{2.17}$$

where G_{rad} is the radiative conductance and is mathematically given as

$$G_{rad} = 4\varepsilon A_d \sigma (T^3 + T_o^{\ 3}) \tag{2.18}$$

The total noise in the detector ΔV_n is given as

$$\Delta V_n = \sqrt{V_{1/f}{}^2 + V_J{}^2 + V_{TF}{}^2 + V_{BG}{}^2} \tag{2.19}$$

If the detector is operating in the background noise limit, it will have least noise and maximum performance.

2.3.4 Bolometer figures of merit

The change in the detector resistance with temperature is characterized by the temperature coefficient of resistance (TCR);

$$TCR = \alpha = \frac{1}{R}\frac{dR}{dT} \tag{2.20}$$

Here R is the resistance of the detector/bolometer and dR/dT is the rate of change of resistance with temperature.

A figure of merit for detector performance is the responsivity $\Re$ which is the detector output voltage or current per unit input infrared power. The detector output voltage is expressed as

$$V_{out} = I_b \frac{dR}{dT}\Delta T_{ac} \tag{2.21}$$

Where I_b is the bias current flowing through the detector. Using (13) and (20), the general expression for voltage responsivity is

$$\Re_V = \frac{\eta\alpha R_{bol} I_b}{G_{eff}\left(1+\omega^2\tau_{eff}^2\right)^{1/2}} \quad \left(\frac{V}{W}\right) \tag{2.22a}$$

The expression for current responsivity is

$$\Re_I = \frac{-\eta\alpha V_b}{(R_s + R_{bol})G_{eff}\left(1+\omega^2\tau_{eff}^2\right)^{1/2}} \left(\frac{A}{W}\right) \tag{2.22b}$$

In (22b), V_b is the voltage across the bolometer and $R_s << R_{bol}$ is a resistance in series with the bolometer through which the current fluctuation is measured. For a voltage biased bolometer, the effective thermal conductance is given as $G_{eff} = G_{th}\left\{1+\alpha\Delta T\left(\frac{R_{bol}-R_s}{R_{bol}+R_s}\right)\right\}$[33], where ΔT is the change in detector temperature due to bias heating. The input power in case of blackbody responsivity $\Re(T,\omega)$ is the radiation from a black body at temperature T and ω is the angular modulation frequency of the input power. The spectral responsivity $\Re(\lambda,\omega)$ on the other hand is the output signal (voltage or current) per unit input monochromatic power. The responsivity is a useful figure of merit but doesn't provide the full picture as it considers neither the noise nor the area of the detector.

The detectivity D^* is an important figure of merit and is a form of area normalized signal-to-noise ratio. In case of a current biased detector, detectivity is expressed as:

$$D^* = \frac{\Re_V\sqrt{A_d\Delta f}}{\Delta V_n} \left(\frac{cm-Hz^{\frac{1}{2}}}{W}\right) \tag{2.23a}$$

In case of a voltage biased detector, detectivity is expressed as

$$D^* = \frac{\Re_I\sqrt{A_d\Delta f}}{\Delta I_n} \left(\frac{cm-Hz^{\frac{1}{2}}}{W}\right) \tag{2.23b}$$

where A_d is the area of the detector, Δf is the electrical bandwidth and ΔV_n and ΔI_n is the total noise voltage or current respectively measured over Δf. Being area and noise normalized, the detectivity is useful in comparing different detectors. Depending on the type of responsivity used, detectivity can be correspondingly spectral or blackbody.

The noise equivalent power (NEP) is another important figure of merit. The NEP is defined as the absorbed power change in a detector that produces an output signal equal to the total rms noise of the detector. Depending on the type of biasing, the NEP is mathematically expressed as

$$NEP = \frac{\Delta V_n}{\Re_V} \ (W) \tag{2.24a}$$

or

$$NEP = \frac{\Delta I_n}{\Re_I} \ (W) \tag{2.24b}$$

2.4 Flexible substrates

Polyimides and polyesters are the two main materials used for flexible substrate applications. Of the two, polyimides are the more popular with about 80% of the market share [Stearns]. A polyimide is basically a polymer of imide monomers. It is known as a thermoplastic or a thermal polycondensate. Typically a polyimide is produced by a condensation reaction like polymerizing aromatic dianhydride and aromatic diamine. It is not a true thermoplastic though because it degrades before its glass transition temperature. It is not considered a true thermoset because it is not cross

linked. Notable characteristics of polyimides are good mechanical properties including fatigue resistance, excellent high temperature resistance, excellent chemical resistance and excellent electrical properties particularly dielectric strength.

Although the most common method of applying polyimides is spin coating, a consequence of its excellent resistance to chemical reaction is that most polyimides are impossible to dissolve in common solvents. This makes it impossible to apply a film of polyimide by dissolving the polyimide in a solvent and applying it to a surface. Generally, a coating of a polyimide precursor is applied to a surface and is subsequently converted to a polyimide by curing. Curing a polyimide usually involves the removal of the solvent carrier and other volatile materials from the layer and the final imidization or hardening of the polymer into an intractable polyimide film. Curing is generally a multi step process involving a post application bake immediately on hot plates. This is followed by loading the wafer into an oven preheated to the hot plate temperature. The temperature is ramped up to a temperature between 280-400°C, depending on the type of application. In the current application, post application bake on hot plates was done at 130°C for 6 minutes followed by a curing in an oven at 270°C for 4-6 hours.

Although the use of adhesion promoters has been reported for optimal adhesion, for the present requirements, this was not necessary as the polyimide was to be subsequently peeled off the carrier wafer. To facilitate peeling off, the use of sacrificial Al has also been reported[60].

2.5 Conclusions

This chapter presents an introduction to infrared radiation, bolometers and flexible substrates. Two main types of infrared detectors namely photon detectors and thermal detectors are discussed. Photo detectors have a fast response time but need cryogenic cooling for during operation to get a good signal to noise ratio. They are also narrow band devices. Thermal detectors on the other hand are slow but have a broadband response and can be operated at room temperature.

The working of bolometers has been discussed. Different materials employed in bolometric roles have been discussed. Noise sources in bolometers have also been discussed.

Bolometer figures of merit have been discussed. These include the temperature coefficient of resistance (TCR), the responsivity, the detectivity and the noise equivalent power (NEP).

The final part of this chapter presents a brief introduction to flexible substrates.

CHAPTER 3

PACKAGING

3.1 Microsystems packaging

Microsystems packaging encompasses the fields of microelectronics, systems engineering and systems packaging. Microelectronics refer to devices which have dimensions less than a micrometer like integrated electronic circuits, photonic devices, rf devices and MEMS. All electronic products fall within the purview of systems engineering while packaging is the interconnection between electronic systems and other components to form a complete electronic product.

Microelectronic devices are made by performing a series of fabrication steps on a large piece of a semiconductor substrate like Si called a wafer. A wafer is generally circular in shape and can vary from 2" to 12" in diameter. Integrated electronics were the first type of microsystems and processing techniques were developed for integrated circuit fabrication. Semiconductor fabrication is a mature field and process details and guidelines are well documented[61]. Other Microsystems like MEMS have borrowed heavily from these fabrication techniques. Depending upon the size of the individually integrated circuit or system, there can be hundreds to thousands of them on a single wafer. After completion of the fabrication process, the wafer is cut into pieces to yield

the individual microsystems. This process is called dicing. To make this system usable requires packaging so that they can be tested and assembled on to a system board. The functions of a typical package are to protect, power and cool the microsystem and also to provide a mechanical and electrical connection between the microsystem and the outside world. Depending on the microsystem requirements, packages can be uniquely adapted. A typical package like a quad-in-line-package is shown in Figure 3.1. A more renowned cousin is the dual-in-line-package (DIP) which has two rows of connector leads instead of four. The package is generally fabricated separately and the die containing the microsystem is placed in it. We have been using silver colloidal paint to bond the die to the package. Electrical connections are then made from the bond pads on the die to the posts on the package with Au or Al wires by e.g. ultrasonic bonding. These connections pass electrical signals to and from the microsystem. After wire bonding, the entire structure is sealed with a plastic material. Only the leads are visible which are cut out of the frame and bent so that they can be inserted into slots in a system board. This may not be needed for surface mount devices. Excellent details on microsystems packaging technology are available in references[62,63].

In contrast to the conventional packaging technique described above is the wafer level packaging (WLP) scheme[64, 65, 66, 67, 68, 69, 70, 71, 72, 73, 74]. Whereas conventional packaging techniques are essentially a two part process with the microsystem and the package fabricated separately, wafer level packaging employs steps subsequent to completion of system fabrication but prior to dicing to build a package as part of the

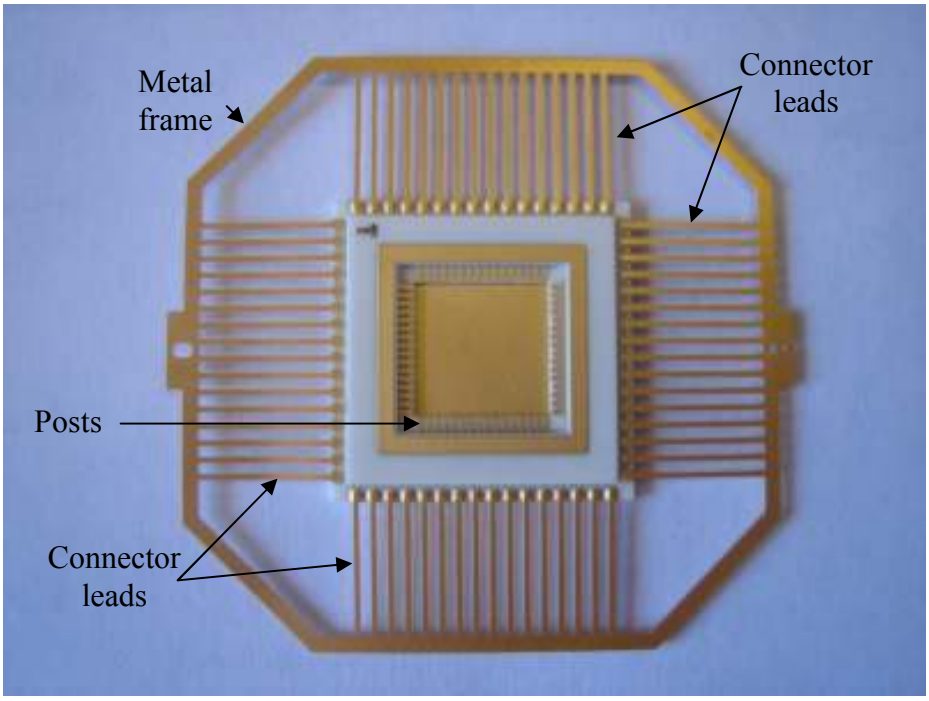

Figure 3.1. Quad-in-line package

fabrication process. The WLP forms the electrical connections on the wafer, assembled face down on a carrier substrate or board using surface mount technology (SMT) followed by encapsulating, testing and then dicing. The biggest advantages of wafer level packaging are a reduction in size and cost. Shortcomings include a limited number of input/output channels as the electrical connections have to be within the die active area. This is more of an issue in VLSI systems that require a large number of input/output channels. Another disadvantage is that the device is tested after packaging. This leads to a lower yield[62,63].

3.2 MEMS packaging

Microelectomechanical systems enable the integration of integrated electronics with sensors and actuators. Despite the minute dimensions of MEMS devices, the

extremely small mass per unit volume makes the microstructures quite robust. This is very appealing to technology developers as it enables the realization of a complete system-on-chip. MEMS packaging is especially challenging because the packaging not only has to perform the traditional duties like protecting the device, providing an electrical interface between the device and the outside world and dissipate heat, but do so while not interfering with the capabilities of the enclosed MEMS device e.g. the packaging of a pressure sensor must ensure that the sensing device is in contact with the pressurized medium yet protected from any harmful effects in that medium, or the packaging for valves has to provide interconnects for both the electrical signals as well as the fluid conduits. A general requirement for MEMS packaging is that the minimum volume required by the device to operate must not be obstructed. While in case of actuators, this means free space for physical motion, in the current work it means unobstructed sight of the heat source for the thermal sensor. MEMS packaging like fabrication, has borrowed heavily from techniques developed for IC packaging; a field that is well established. Designing packages for MEMS involves considering a number of factors. Some of these are common with electronic IC packaging while others are unique to MEMS applications. Issues unique to MEMS devices include wafer stack thickness, where standard IC fabrication industry wafer thickness for particular wafer diameters is a fixed standard. In contrast, a stack of bonded Si or glass wafers for MEMS can have a thickness exceeding the IC fab standards. This can pose challenges for packaging foundries. Another cause for concern are micromachined components in MEMS devices subjected to often violent and random vibrations during dicing.

Whereas a post processing type release step can be employed to release the micromachined layer after dicing, this comes at the cost of batch processing making it an expensive option.

Relatively simpler optical MEMS devices have been reported to have been packaged on a ball grid array format[62]. MEMS chips mostly need vacuum packaging provided by costly hermetic packages for different reasons. For devices employing a cantilever type member for example, the presence of gas molecules can cause unwanted friction and damping. The presence of gases can also cause metal wear degrading device performance while moisture can fog optics[62,63]. Atmosphere control agents like getters have also been employed that keep the MEMS device ambient clear of specific target chemical species.

The major packaging issues a micro optoelectromechanical system (MOEMS) like a thermal detector faces, include, minimum absorption of infrared energy in the sensor optical window, a sealed vacuum environment and in case of a detector on flexible substrates, a robust enough package that retains its integrity despite being bent.

3.3 Traditional Micro Opto-Electro-Mechanical Systems (MOEMS) packaging

An obvious solution to the requirement of an optically transparent window for MOEMS sensors is an optical porthole in the package cap. This has been a satisfactory solution for traditional MOEMS devices like the Texas Instruments micromirror array. Most MEMS packages are standard sealed hermetic containers such as ceramic-dual-in-line package (Cerdip). While high in cost, ceramic and metal packages provide adequate protection. An optical porthole in the protective cap over a MEMS device serves the

purpose of protecting the device without obstructing view. Another possibility is the use of flip chip bonding. In this case the chip active surface is placed face down on a substrate creating a natural protective zone. The gap can be controlled accurately by controlling the chip bump height. A conduit of light like an optical fiber can be fixed to a port in the Si substrate.

Encapsulation using organic overcoats or sealing with an inorganic material have been the traditional ways to vacuum package[62]. Encapsulation is cheaper but has a limited lifespan primarily due to the permeation properties of the resin used. Inorganic seals are longer lasting but more expensive. Wafer and die level packaging[64, 65] are employed within this realm.

The atmosphere control inside the sealed cavity is another issue of importance. The package atmosphere is affected because the package can absorb materials as well as emit (outgas) materials into the cavity. A package may thus provide acceptable vacuum to start with but the quality of the vacuum may degrade with the passage of time. Getters have been known to be employed towards this end. Theoretically getters can be employed for all kinds of pollutants. Most optical systems use a high-vacuum hermetically sealed package.

3.4 Device level vacuum packaging

Traditional packaging techniques discussed hitherto are used in conventional rigid Si based systems. While the same packaging techniques may be applied to devices on flexible substrates, it would most probably mean sacrificing flexibility. A new device-level vacuum-package scheme is presented here in which an optical cavity

transparent in the infrared spectrum of interest is grown around a micronmachined thermal detector. An example of such a packaging scheme is shown in Figure 3.2. A polyimide superstrate can be added to provide additional protection and also help keep the detector in a zero stress plain[25]. Different issues in the design of such a packaging scheme include the transmission properties of the optical cavity, the quality of the seal, the thermal conductance in the vacuum package as well as the quality of the atmosphere inside the vacuum cavity. These parameters are investigated subsequently in chapter 6 where the cavity design is presented in detail. However, before the detailed design is proceeded with, two important issues need to be investigated. They are the pressure window design and the permeation of gases through the cavity walls.

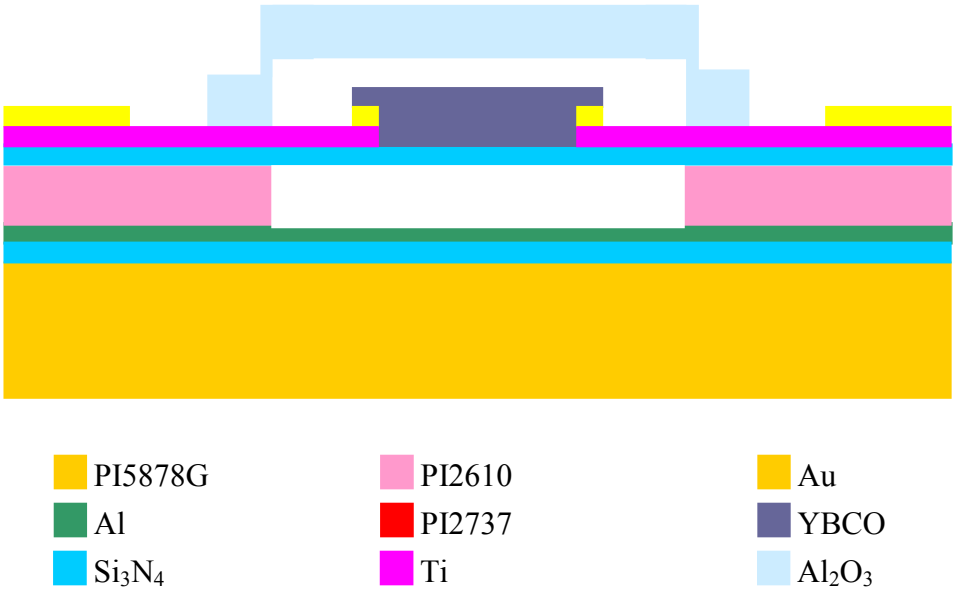

Figure 3.2 Cross-sectional view of a device-level vacuum cavity.

3.4.1 Pressure window

The material properties as well as the window dimensions have a bearing on the window thickness. The design of optical windows used in vacuum or pressure applications[75] is made use of. The maximum stress on a uniformly loaded circular window is

$$S_{\max} = \frac{KD^2P}{4T^2} \tag{3.1}$$

where $S_{\max} = F_a/SF$ is the maximum stress, SF is the safety factor, F_a is the apparent elastic limit, K is an empirical constant, D is the unsupported window diameter, T is the window thickness and P is the load per unit area on the window.

The value of K depends on the method of support of the window as well as the window material properties. A value of $K = 0.75$ is used for clamped windows while $K = 1.125$ is found to be suitable for unclamped windows.

Equation (3.1) is used to find the window thickness. For a rectangular window

$$T = L\sqrt{SF \times K/2}\sqrt{P/(F_a(1+W^2))} \tag{3.2}$$

where L and W are the window unsupported length and width respectively. The fracture strength can be used as F_a in case of ceramics. In the current work though, the tensile strength of the material has been used as F_a .

3.4.2 Gas permeation through the cavity walls

As shown in figure 3.1, the proposed vacuum cavity is bounded by a metal Al film (the cavity base), very short sections of cured PI2610 sacrificial polyimide (the

vertical walls), a thin segment of Si_3N_4 and the optical window material. The cured PI2610 has a very low vapor pressure and along with the very small dimensions outgassing into the cavity is not being considered a source of leakage. As such the optical window properties need to be examined to see how long the vacuum can be sustained in the cavity.

Many physical and chemical processes are controlled by the permeation, diffusion and solubility of gases in materials[76]. The formation of bubbles in glasses, oxidation of metals via diffusion controlled processes (often controlled by surface oxide films), diffusion of gases through films and the outgassing of various gases from a variety of organic materials like polyimide are common examples. In most of the above mentioned cases, a gas surrounding the material is absorbed in it or a gas present in the material is desorbed to the ambient. This process may be chemical in nature where gases bond with the host material or be purely physical in nature as in the case of gases in glass or polymers. Mass transport of the gas occurs when the gas atoms or molecules diffuse through the material with the formation of a concentration gradient in the materials from the region rich in the gas to the region poor in the gas. The vacuum cavity in the proposed design is formed using a combination of sputtering and micromachining. The vacuum cavity is formed by rf sputtering carried out in an Ar environment at 10 mT. As such the cavity internal pressure is expected to be 10mT whereas the optical layer is exposed to 1 atm. pressure externally. Thus, a pressure differential of ~ 1 atm. exists across the thin optical membrane. The actual concentration of the gas in the material is determined by the solubility coefficient,

usually called just the solubility and the partial pressure of the gas in the surrounding atmosphere. The flow rate of a gas through a material is controlled by the permeability of the gas in the material.

The terms diffusivity, solubility and permeability are related through the expression

$$K = DS \tag{3.3}$$

where K is the permeability, D is the diffusivity and S is the solubility. The permeability of a material determines the flow rate through a specimen once steady-state flow is attained. The diffusivity or diffusion coefficient refers to the rate of movement of individual atoms or molecules and determines the time needed to reach steady-state flow. The solubility refers to the dissolved gas concentration per unit of applied pressure of the gas under consideration and not just to the dissolved concentration.

Gas diffusion and permeation in partially or entirely crystalline ceramic materials (ala a sputtered layer of Al_2O_3 forming an optical layer in the vacuum cavity) can occur either by migration through an amorphous phase or migration through the crystalline lattice itself. In general, diffusion through an amorphous boundary phase will be much faster than the crystalline lattice. Many common ceramics used for tubing, crucibles etc. contain a significant portion of a vitreous phase that bonds the crystalline phase together to form a solid material. The morphology of such material closely resembles those of glass-ceramics. The sputtered Al_2O_3 used in this work is also expected to be of this type.

The value of He permeability through different types of ceramic Al_2O_3 (ranging from 94% to 99.5%) ranges from ~100-1000 atoms/(s-cm-atm) at room temperature. Using the general gas law

$$P = \frac{nRT}{V} \tag{3.4}$$

where n is the number of moles, $R = kN_A = 8.314 J/(mole.K)$ is the universal gas constant, k being the Boltzmann constant and N_A being the Avogadro's number. The corresponding pressure for a cavity 100 x 100 x 4 μm^3 is shown in Figure 3.3. Common atmospheric constituent gases like H_2, N_2, O_2 have larger molecules than He and a corresponding lower permeability through Al_2O_3.

3.5 Conclusions

This chapter presents an introduction to microelectronics and Microsystems/MEMS packaging. Conventional packages like dual-in-line and quad-in-line are discussed as well as wafer level packaging schemes. MEMS packaging requirements are discussed in light of the commonalities and differences between MEMS and traditional integrated circuit technologies. MOEMS packaging is also discussed. Conventional solutions like an optical porthole in the package cap or flip chip bonding for devices employing a light port like an optical fiber port are discussed. The new concept of device-level vacuum packaging and its necessity for flexible substrates is presented. Different issues involved in the design of device–level vacuum packages include the transmission properties of the optical window, the quality of the

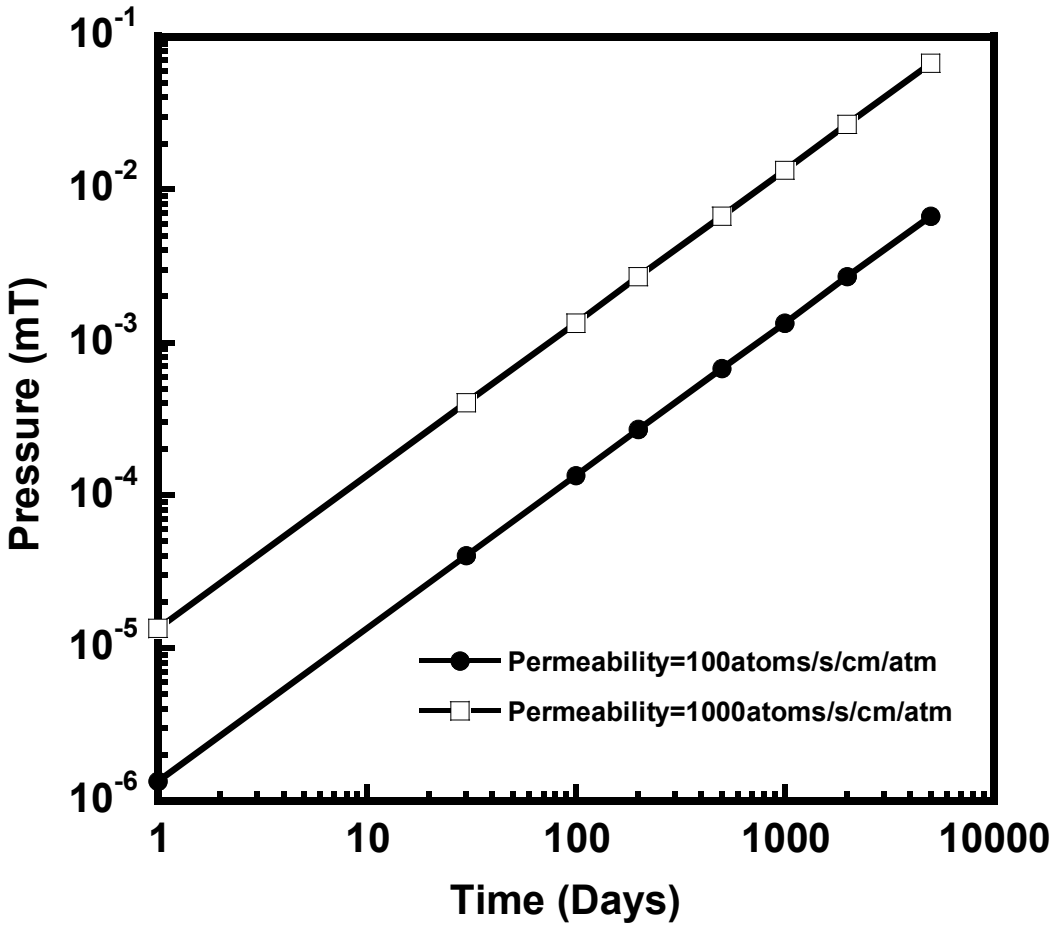

Figure 3.3 Cavity pressure due to He permeation as a function of time.

vacuum seal, and the thermal conductance from the detector to the ambient in the vacuum cavity. Some design issues are addressed in detail in chapter 6 when the cavities are actually fabricated but the design of a micro pressure window as well as the permeation properties of gases through the optical window are analyzed in detail. It was seen that a diffusion model using small He atoms predicts an increase of ~10^{-1} mT in the cavity pressure after 6000 days.

CHAPTER 4

BOLOMETER CHARACTERIZATION

Various infrared detector figures of merit have been discussed in chapter 2. This chapter presents the experimental measurement of these figures of merit. Measurements were carried out in the microsensors laboratory at the University of Texas at Arlington. Primary measurements included the device voltage versus current (VI) characteristics, the device resistance as a function of temperature (R(T)), the device responsivity ($\mathcal{R}$) and detectivity (D*). Secondary quantities like the temperature coefficient of resistance (TCR) α, the thermal conductance G_{th} and the device noise equivalent power (NEP) are calculated from the above mentioned primary measurements.

4.1 Voltage-Current (VI) characteritics

The VI measurement is done by sweeping a current through the bolometer and simultaneously measuring the voltage developed across it. An Agilent 4155B semiconductor parameter analyzer is employed for this purpose. During fabrication or prior to packaging after fabrication, the bolometers can be checked under a probe station by probing directly on the bond pads. After packaging and bonding though, the electrical contact needs to be made with the package pins. For VI measurements in vacuum, the device is packaged, bonded and mounted inside a cryostat and evacuated

using a vacuum pump to pressures ranging between 50-90 mT. The current is typically swept from -2 μA to 2 μA in 100 nA steps. In case the device resistance is high, the current is limited to smaller sweeps to limit the power dissipation and thus heating up of the device. A 500 ms delay is introduced between consecutive current steps to achieve thermal equilibrium between the bolometer and the ambient substrate before measurements. Considering the geometery of the devices, the VI characteristic can tell us if the metal-semiconductor (Au-YBCO) contact is an Ohmic contact or a junction. Joule heating causes non linearity in the VI curve at higher currents. This will be seen when measurement results are discussed in subsequent chapters.

4.2 Temperature dependant resistance (R(T))

The resistance is measured as a function of the temperature. This data is used to calculate the temperature coefficient of resistance (TCR), α. The packaged microbolometer is mounted on a controllable temperature platform in a cryostat. A thin layer of thermal conducting paste like Dow Corning 340 heat sink compound ™ is used to ensure a smooth contact between the package and the host platform. The temperature of the variable temperature head is controlled with a Lakeshore DRC-91C temperature controller. The temperature controller uses a combination of a heater coil and a Helium charged Leybold-Heraeus closed cycle refrigerator to control the temperature. Temperature sensing is done though a diode attached to the variable temperature platform. The resistance measurement is done indirectly using three HP34401A digital multimeters set up as shown in Fig. 4.1. One multimeter is used as an Ohmmeter and serves as the fixed current source. The other two multimeters are used as voltmeters and

measure the voltages V_1 and V_2 across known resistances R_1 and R_2 respectively. The resistance of the bolometer (R_{DUT}) can be calculated as

$$R_{DUT} = \left(\frac{V_1 - V_2}{V_2} \right) R_2 \tag{4.1}$$

The bolometer temperature is varied from ~250 K to 320 K using the temperature controller in steps of 1 K and the bolometer resistance R_{DUT} is calculated at each step using (1). For such measurements an evacuated cryostat is used to avoid vapor condensation on the devices.

R(T) measurements can also be done using the Micromanipulator™ variable temperature shielded probe station in the noise lab. This setup does not allow measurements in vacuum. The temperature controller has a smaller temperature range from ~295-313 K. The temperature range on that setup is limited also because of condensation of water vapor on the bolometer package at lower temperatures.

4.3 Thermal conductance G_{th}

The thermal conductance is a measure of the loss of heat from the bolometer. The R(T) as well as VI data is used to experimentally determine the value of G_{th}. From chapter 2 (2.9) we know that

$$G_{eff} \Delta T = P_I \tag{4.2}$$

where G_{eff} is the effective thermal conductance from the bolometer to the substrate, $\Delta T = T - T_0$ is the change in temperature due to the bias heating. P_I is the power dissipated in the bolometer due to the bias and is given as

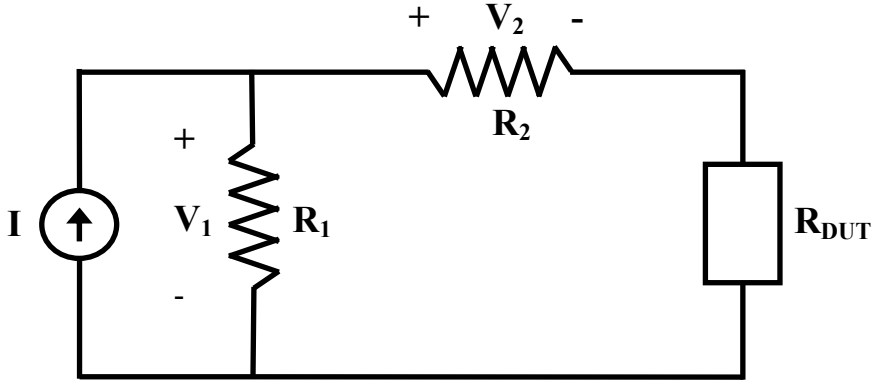

Figure 4.1. Circuit to measure the resistance of the bolometer.

$$P_I = VI \tag{4.3}$$

In case of a bolometer biased with a fixed current (Figure 4.2(a)), the effective thermal conductance G_{eff} incorporates the thermal conductance from the device to the substrate, the thermal radiation from the device and also the effect of the bias current heating

$$G_{eff} = G_{th} + G_{rad} - \alpha P_I \tag{4.4}$$

In case of a fixed voltage bias applied to a bolometer (Figure 4.2(b)), the relation between the effective thermal conductance and the physical thermal conductance from the device to the ambient is expressed as [33]

$$G_{eff} = G_{th}\left\{1 + \alpha\Delta T\left(\frac{R_{bol} - R_s}{R_{bol} + R_s}\right)\right\} \tag{4.5}$$

where R_{bol} is the bolometer resistance, R_s is the series resistance with the bolometer through which the current fluctuations are measured. Ideally, $R_s < R_{bol}$. ΔT is the change in the detector temperature due to the bias. G_{th} is the physical thermal conductance between an unbiased bolometer and the surroundings.

In case of semiconducting bolometers the resistance varies non linearly with temperature following the Arrhenius relation

$$R(T) = R_0 e^{\frac{E_a}{kT}} \tag{4.6}$$

where E_a is the activation energy of the material, k is the Boltzmann constant and T is the temperature. R_0 and E_a are determined from the measured resistance versus temperature data by plotting $\ln(R)$ versus $1/kT$. Correspondingly, the TCR is also nonlinear and is given as

$$\alpha = \frac{1}{R}\frac{dR}{dT} = -\frac{E_a}{kT^2} \tag{4.7}$$

To incorporate the effects of non linear resistance and TCR, the resistance of the device is used to calculate the resulting temperature of the device due to bias heating using (4.6)

$$T = \frac{E_a}{k}\frac{1}{\ln(R(T)/R_0)} \tag{4.8}$$

where $R(T) = V/I$ is calculated from the measured VI characteristics. Correspondingly, $\Delta T = T - T_0$ is calculated and (4.2) is used to find G_{eff} at each current bias (the bias current is swept from -2 μA to 2 μA in increments of 100 nA). The

thermal conductance G_{th} is calculated from G_{eff} using (4.4) or (4.5) depending on the type of bias, with the TCR α and the power dissipated in the bolometer P_I calculated using (4.7) and (4.3) respectively at each current bias.

The coefficient of thermal radiation is calculated as

$$G_{rad} = 2\varepsilon A_d \sigma (T^4 - T_0^4) \cong 2\varepsilon A_d \sigma (4T_0^3 (T - T_0)) = 8\varepsilon A_d \sigma T_0^3 (T - T_0) \qquad (4.9)$$

where ε is the emmisivity of the detector assumed equal to the absorptivity η of the material over all wavelengths, A_d is the area of the detector and σ is the Stefan-Boltznmann constant. For the current geometries this is orders of magnitude smaller than the other kinds of thermal conductance[28]. The calculation of absorptivity η from the measured data is discussed in the section 4.4.

The heat capacity C_{th} depends on the device geometry and the thermal capacities of the constituent materials. It can be determined experimentally from the measured data using

$$C_{th} = G_{eff} \tau_{eff} \qquad (4.10)$$

where $\tau_{eff} = 1/2\pi f_{-3dB}$, f_{-3dB} being the modulation frequency at which the device output is half the maximum output[41]. C_{th} can also be calculated using the heat capacity per volume of the materials used and the dimensions of the device.

4.4 Responsivity ($\mathcal{R}$) and Detectivity (D*)

Responsivity ($\mathcal{R}$), of a bolometer is defined as the device output signal (voltage change across it or current change through it) per incident input power.

Experimentally, $\mathcal{R}$ is measured by biasing the detector and exposing it to infrared energy from an infrared source like a QTH lamp or a mock blackbody source. A mechanical chopper is placed between the source and the detector to modulate the incident radiation at different frequencies, f. Figure 4.2 shows the two bias conditions used in the current work. In case the detector is biased with a fixed current bias (Figure 4.2(a)), the voltage across the detector output is measured. The output voltage is fed to a low noise preamplifier to improve the signal to noise ratio before being input to a signal analyzer. The signal analyzer displays output voltage across the detector as a function of frequency. Fig. 4.3 shows a typical signal spectrum. The power incident on the detector is found by employing a calibration detector with a known responsivity. In the current work, an Oriel 70124 pyroelectric detector 5 mm in diameter with a responsivity of 1000 V/W is used for calibration. A bipolar junction transistor (BJT) operating in saturation serves as a constant current source. During the course of the current work, some devices with very high resistance could not be biased with this constant current source as they caused the BJT to operate in the linear region instead of the saturation region. A fixed voltage bias was thus applied across the bolometer in series with a resistor of known value as shown in Figure 4.2(b). The current change in the bolometer due to the incident radiation is found by measuring the voltage across the resistance in series with the bolometer. Figure 4.3 shows a typical signal spectrum. In addition to the signal, the noise is also measured using the signal analyzer. The noise measurement in conjunction with the responsivity measurement is used to calculate the detectivity of the bolometer using equations 2.23(a)) or (2.23(b) in chapter 2.

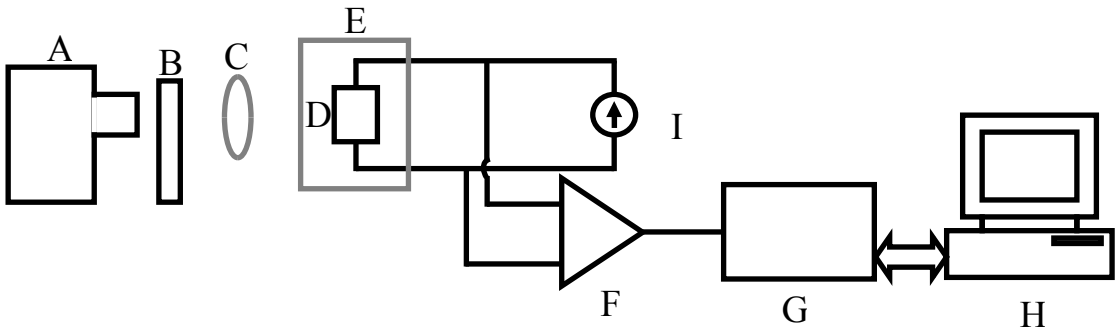

(a)

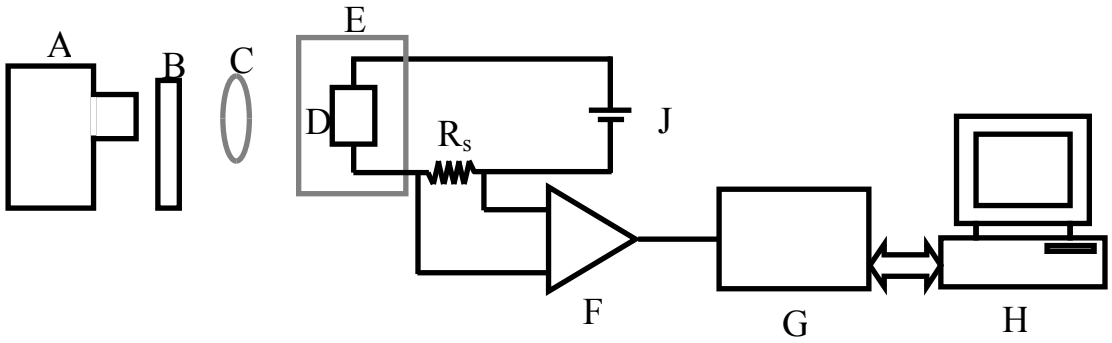

(b)

A Infrared source **B** Chopper **C** Optical lens **D** Bolometer

E Cryostat **F** Low noise preamplifier **G** Signal analyzer **H** Computer

I Constant current source **J** Constant voltage source

Figure 4.2 (a) Constant current bias setup for voltage responsivity measurement (b) Constant voltage bias setup for current responsivity measurement.

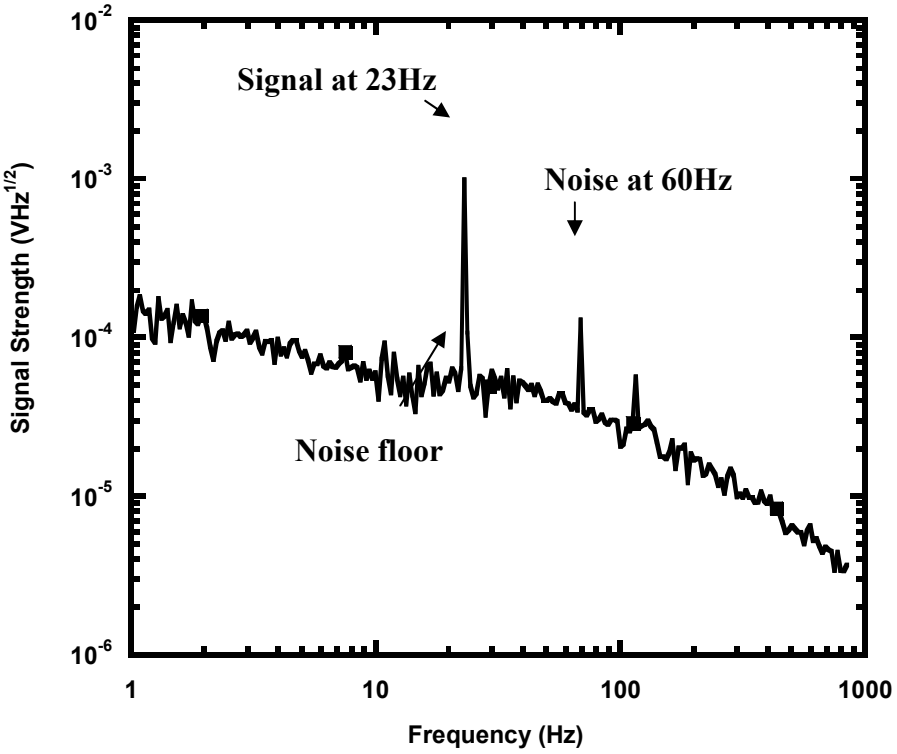

Figure 4.3 Typical signal spectrum

A ZnSe lens may be used to focus infrared energy on to the bolometer. This will improve the signal to noise ratio of the bolometer output signal. Bolometers perform best when operated in vacuum. As such, the devices were mounted in a cryostat with a ZnSe optical window to illuminate the detector. The cryostat was evacuated to pressures of ~20-70 mT during measurements. In case of device level vacuum packaged devices though, there was no need for such and arrangement and the devices were mounted and measured in air. The noise equivalent power (NEP) can be calculated using equations 2.24(a) or 2.24(b) in chapter 2.

The absorptivity of infrared energy in the bolometer can be calculated from the expression for the responsivity. From (2.22(b)), the maximum current responsivity is expressed as

$$\Re_I^{\max} = \frac{-\eta\alpha V_b}{(R_s + R_{bol})G_{eff}} \tag{4.11}$$

where R_{bol} and R_s are the bolometer and series resistance respectively (Figure 4.2(b)). α , G_{eff} , $\Re_{I,\max}$ and the associated V_b can be calculated as discussed in the preceding sections.

Likewise, from 2.22(a), the expression for absorptivity for a current biased microbolometer is

$$\eta = \frac{\Re_V^{\max} G_{eff}}{\alpha I_b R_{bol}} \tag{4.12}$$

4.5 Conclusions

This chapter presents the experimental techniques employed to characterizre microbolometers. Primary measurements included the device voltage versus current (VI) characteristics, the device resistance as a function of temperature (R(T)), the device responsivity ($\mathcal{R}$) and detectivity (D*). Secondary quantities like the temperature coefficient of resistance (TCR) α, the thermal conductance G_{th} and the device noise equivalent power (NEP) are be calculated from the above mentioned primary measurements.

CHAPTER 5

MICROBOLOMETERS ON FLEXIBLE SUBSTRATES

5.1 Introduction

Flexible substrates facilitate conformal electronics, enabling foldable systems-on-a-chip, made of sensors, electronics and actuators, with possible applications as electronic fabrics, smart tags and conformal sensor arrays among others in the fields of defense, medicine, industrial monitoring and testing. Microbolometers on flexible substrates are part of a strategic goal of making a "smart skin" – a flexible substrate housing a plethora of sensor systems for measuring parameters like temperature, moisture, pressure, fluid flow and acceleration. Microbolometers on flexible substrates have been successfully fabricated and tested in the past[24, 25, 26]. These devices were self supporting microbolometers.

This chapter presents work on the development of microbolometers supported by thin micromachined membranes on flexible polyimide substrates. The main difference between the present work and the previously reported is that these bolometers are fabricated on a micromachined support membrane since these sensors are part of an effort to develop smart skin and will have to be integrated with other sensors. Typically, the performance optimization of each type of sensor would put contradicting

requirements on design parameters. For example, if pressure and thermal sensors are to be integrated on a single micromachined bridge, as would be required in case of the "smart skin", the mass, dimensions, material properties (thermal conductivity, specific heat etc.) of the bridge structure need to be optimized as a shuttle mass for the pressure sensors and as a support with low thermal conductivity and mass for the thermal detectors. Therefore, it is essential to investigate the performance of such flexible bolometers on a micromachined membrane.

5.2 Detector fabrication

All material depositions during fabrication were done using 3-inch targets in an rf-magnetron sputter system in a pure Ar environment at 10 mT pressure. To achieve a pure Ar sputter environment, the chamber is first evacuated down to ~ $5x10^{-6}$ T using a combination of a mechanical diaphragm pump and a turbo vacuum pump. Positive photolithography was used throughout the process with Shipley 1813 being the photoresist used along with MF319 developer. A computer generated three dimension model of a bolometer is shown in Figure 5.1. A cross sectional view of the device at XX' is shown in subsequent illustrations along with a computer generated three dimensional model. The first layer to be formed is 4000 Å of Si_3N_4. This layer serves to improve the adhesion of subsequent layers to the Si wafer. This is followed by spin-coating liquid polyimide PI5878G onto the wafer to develop what will ultimately become the flexible substrate. The thickness of the polyimide film depends on the spin speed of the wafer at the time of application. The liquid polyimide was poured onto the wafer which was then spun at 2000 rpm for ~50 s. It was then pre baked at 110°C for 6

min. The process was repeated 5 times before the polyimide coated wafer was loaded into an oven preheated to 110°C for post bake. The oven temperature was steadily increased to ~265°C over the next hour and kept at that temperature for about 5 hours. The expected final polyimide thickness was ~ 40 µm. A layer of Si_3N_4 was sputtered on the polyimide. This layer serves the same purpose as the previous one i.e., to promote adhesion between the polyimide and the subsequent layers sputtered during fabrication. The nitride is resistant to the wet etchants but not to the CF_4 used for dry etch downstream. To provide protection from dry etchants, a 500 Å layer of $SrTiO_3$ was sputtered on to the nitride. 4000 Å of Al was sputtered to form a reflecting mirror as part of a resonant cavity beneath the detector to improve infrared radiation absorption in the bolometer. Theoretically, the Al needs only be in the shape and size of the subsequent thermistor, but in the current device it was patterned and etched using the

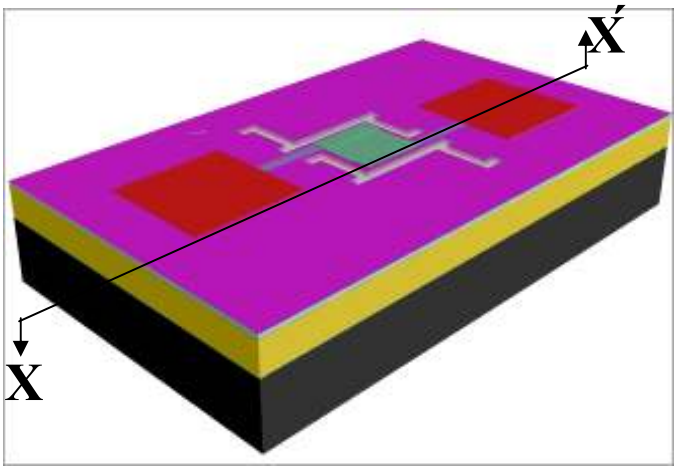

Figure 5.1 Computer generated three dimensional model of a typical microbolometer. The device cross sections are shown at section XX' in subsequent figures illustrating various fabrication steps.

"trench mask". This was done solely to facilitate alignment when the trench mask is used to create trenches straddling the bolometers in the support nitride layer (Figure 5.2). Dilute commercial Al etchant (Al etchant:DI::1:15 ml) heated to 40°C was used to etch the Al. PI2610 was subsequently spun on to form the sacrificial layer. After curing, the final sacrificial polyimide thickness was 0.5 μm (Figure 1(c)). The thickness of the sacrificial PI2610 is significant as it determines the length along the optical axis of the resonant cavity backing the microbolometer. This dimension determines the resonant frequency of the bolometer. In case of a broadband device like a bolometer, this can be used to maximize power absorption in certain parts of the electromagnetic spectrum in the infrared region. A 4000 Å thick layer of Si_3N_4 was then sputtered onto the polyimide followed by 500 Å of $SrTiO_3$. The nitride was to form the support membrane for the bolometer while $SrTiO_3$ acted as a dry etch stop as explained earlier. Ti was used to make the electrodes because of its low thermal conductivity among metals (21.9 W/m/K). This is important because as explained earlier in chapter 2, the thermal conductance from a bolometer has to be kept at a minimum to maximize detector performance. It will be seen in later thermal analysis that the metal conductor is a major source of heat loss from the bolometer to the substrate. 1500 Å of Ti was used as the electrode material, followed by deposition and patterning of 750 Å of Au as bonding pads as well as contacts between the detector material and the electrodes. The Au is used to provide an Ohmic contact between the Ti and the YBCO semiconductor. Ideally, Au should be deposited immediately after Ti without breaking the system

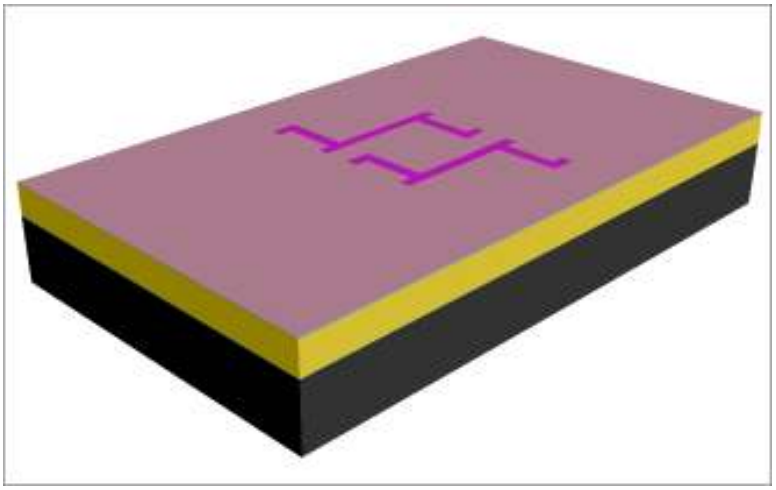

(a)

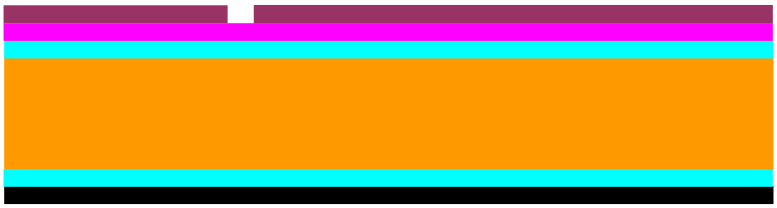

(b)

Figure 5.2 Deposition of Al mirror showing trench shape etch to facilitate subsequent alignment (a) Computer generated three dimensional model, and (b) cross section view (layer thicknesses not to scale).

vacuum as Ti oxidizes very rapidly thus degrading the electrical properties of the Ti metal contacts. Due to system limitations though (the sputter system has only a single target capability), this could not be done and the vacuum had to be broken to replace the Ti sputter target with a Au target. Au was patterned using a standard ($KI:I_2$) gold etch solution. Adhesion of Au to the Ti has been problematic and depositing Au at a higher temperature of ~280 °C has been observed to improve adhesion fairly consistently. Ti was then patterned by dry etching in $CF_4:O_2$::40:2 sccm (pressure = 100 mT, temperature = 60°C), forming the electrode arms between the aforementioned Au pads and contacts (Figure 5.3). The dry etching was done is short bursts of ~ 6min for a cumulative etch time of ~46min. The last deposition in the fabrication process was 3600 Å of YBCO. The YBCO forms the bolometer. The YBCO was patterned and etched using dilute Al etchant (Al etch:DI::1:10 ml) (Figure 5.4).

Surface micromachining was performed to remove the sacrificial layer, thus releasing the Si_3N_4 membrane supporting the detectors. Trenches were opened around each pixel in the $SrTiO_3$. This was done using 49%HF:DI::1:10 ml as the etchant. This exposed the underlying layer of Si_3N_4. The wafer was put in a reactive ion etcher and the exposed nitride was dry etched with $CF_4:O_2$::40:2 sccm (Pressur = 100 mT, Temperature = 60°C) in short 10 min bursts. The cumulative etch time was 50 mins. The $SrTiO_3$ served as a hard mask. Nitride was thus removed in the trench area exposing the underlying sacrificial polyimide PI2610 (Figure 5.5). The sacrificial polyimide was removed by oxygen plasma ashing using 100-125 W of rf power. The oxygen pressure was kept at 1500 mT. The polyimide was removed in multiple steps of

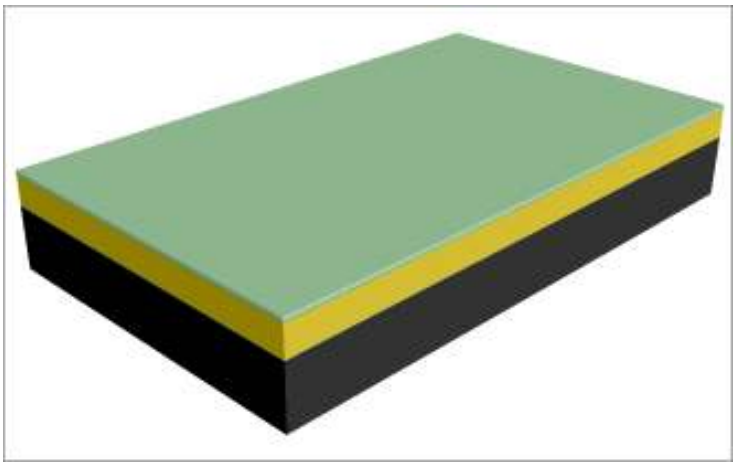

(a)

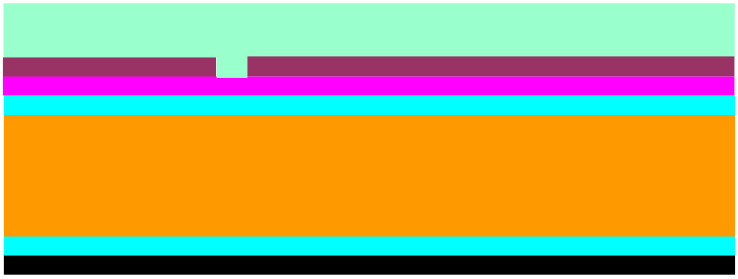

(b)

Figure 5.3 Deposition of PI2610 sacrificial polyimide (a) Computer generated three dimensional model, and (b) cross section view (layer thicknesses not to scale).

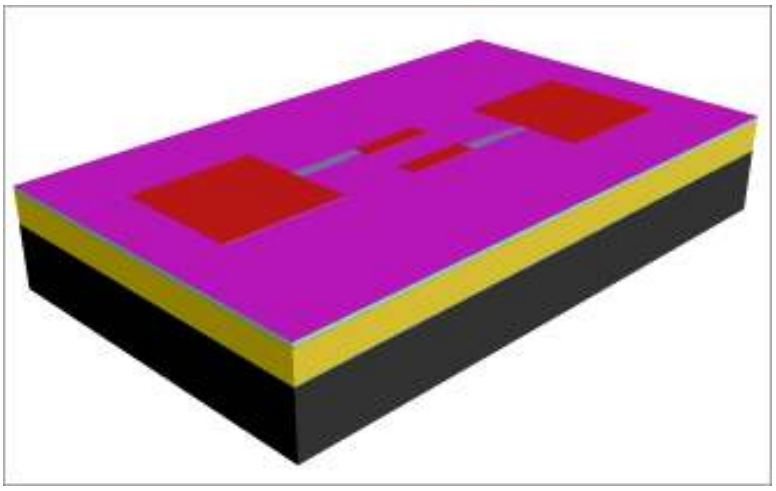

(a)

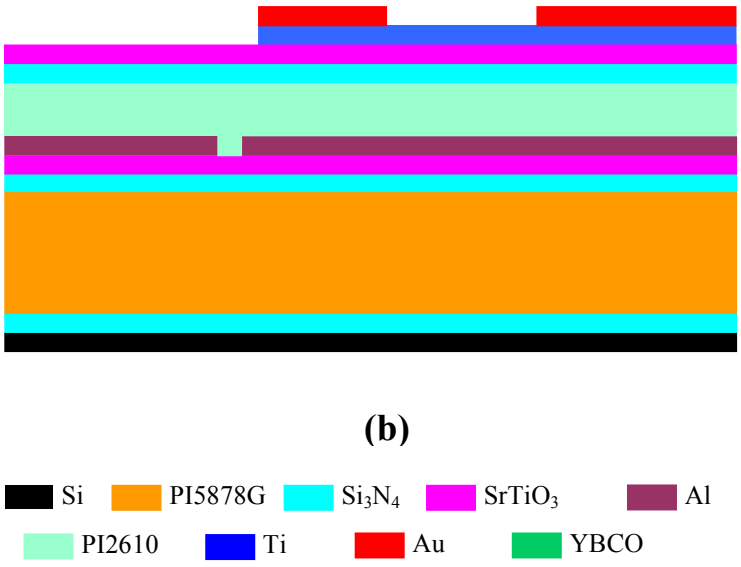

(b)

Figure 5.4 Deposition of Ti arms, Au bond pads and Au contact pads. (a) Computer generated three dimensional model, and (b) cross section view (layer thicknesses not to scale).

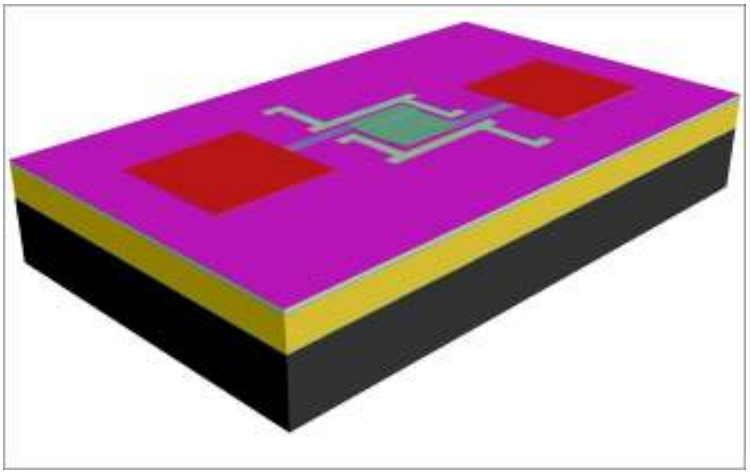

(a)

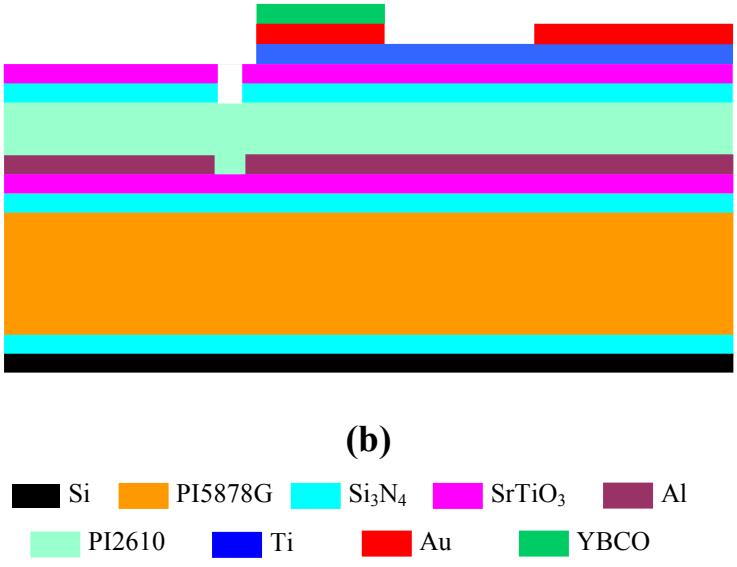

(b)

Figure 5.5 Deposition of YBCO bolometer (a) Computer generated three dimensional model, and (b) cross section view (layer thicknesses not to scale).

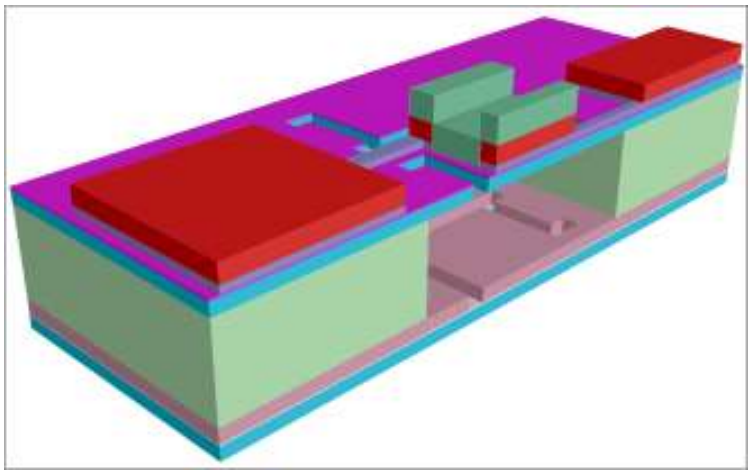

(a)

(b)

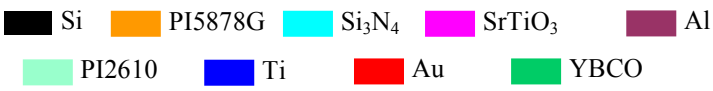

Figure 5.6 Completely micromachined microbolometer (a) Computer generated three dimensional model, and (b) cross section view (layer thicknesses not to scale).

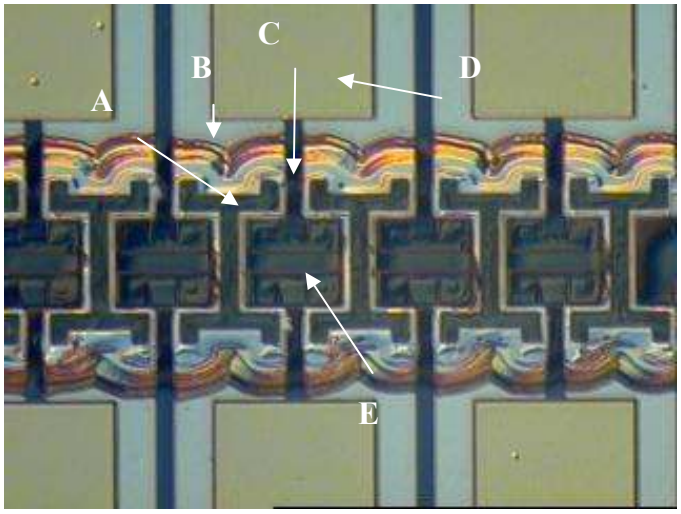

(a)

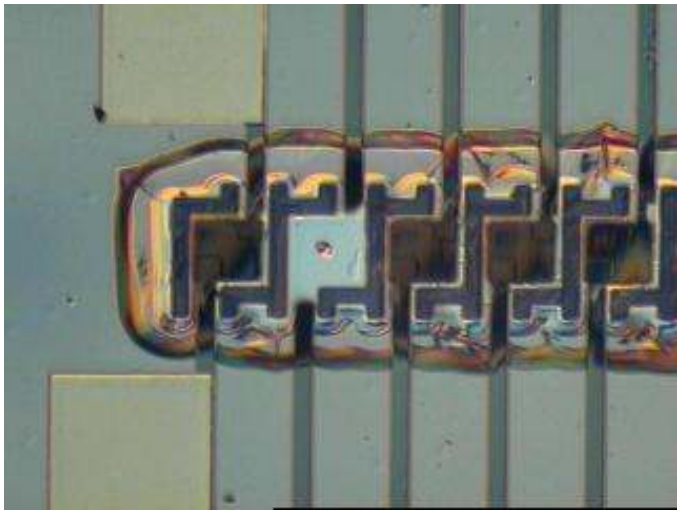

(b)

Figure 5.7 Completed microbolometers on a flexible substrate showing (A) A trench in the supporting Si_3N_4 layer, (B) Supporting Si_3N_4 layer, (C) Ti arm, (D) Au bond pad, (E) YBCO pixel and (F) Al reflecting mirror in; (a) Array of 60x60 μm^2 microbolometers under a microscope, showing the extent of lateral micromachining of sacrificial PI2610 after 10 hours of ashing, (b) Array of 40x40 μm^2 detectors after 10 hours of ashing. The second pixel from the left has been removed and shows Al reflector surface without polyimide.

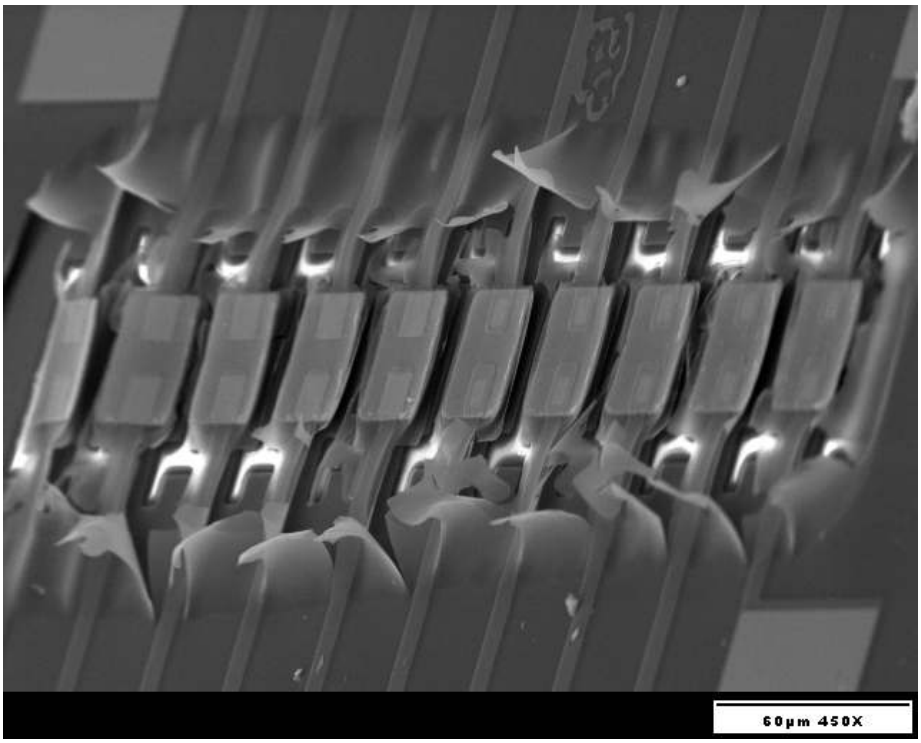

Figure 5.8 SEM graph of an array of 40x40 μm^2 detectors after 10 hours of ashing. The $SrTiO_3$ flakes are clearly visible in this picture.

20 mins of oxygen ashing, followed by 20 mins of cooling (Figure 5.6). It had been observed that heating caused by continuous ashing for long periods of time produced thermal stresses in the nitride layer supporting the detector. The short bursts of ashing were employed to circumvent this problem. The cumulative ashing time was approximately 10 hours. Figure 5.7 shows a computer generated model of the micromachined bolometer as well as an SEM micrograph. of an array of 40 x 40 μm^2 microbolometers. It was seen that the $SrTiO_3$ flaked off the support nitride membrane. The nitride support layer is optically transparent, and at this stage, it was seen that the

PI2610 beneath the smaller 40 x 40 μm^2 pixels was removed completely (Figure 5.8). The polyimide can be peeled off the host wafer to yield sensors on a flexible substrate. Optical photos of 1x10 arrays are shown in Figure 5.7. Different detector sizes and trench geometries are also evident. Figure 5.8 shoes and SEM graph of a similar array.

5.3 Detector characterization

Electrical and optical characterization of the packaged and bonded devices was carried out. Results presented here are for a 40x40 μm^2 device unless otherwise specified. The dc resistance at 301K was measured to be ~3.76 MΩ. Resistance of the device was measured from 240 to 320K (Figure 5.9) and the temperature coefficient of resistance $TCR = \alpha = (1/R)(dR/dT)$, was evaluated. A TCR of -2.63 $\%K^{-1}$ at 301K was measured. The detector VI characteristics were measured using an HP4155B semiconductor analyzer. The non linear VI curve shows the effect of Joule heating (Figure 5.10).

The resistance of the device is non-linear and the Arrhenius relation $R(T) = R_0 \exp(E_a/kT)$ was used to extract the values of $R_0 = 1341\,\Omega$ and the activation energy $E_a = 0.21\,\text{eV}$ of semiconducting YBCO from the data. The thermal conductance from the detector to the substrate, G_{th}, was measured using the Joule heating method detailed in chapter 3. The mean value of G_{th} was 5.61×10^{-7} W/K. The mean calculated G_{th} was used to calculate the resistance of the bolometer using the Arhenius relation. Figure 5.11 shows that the data fit agrees well with the measured data.

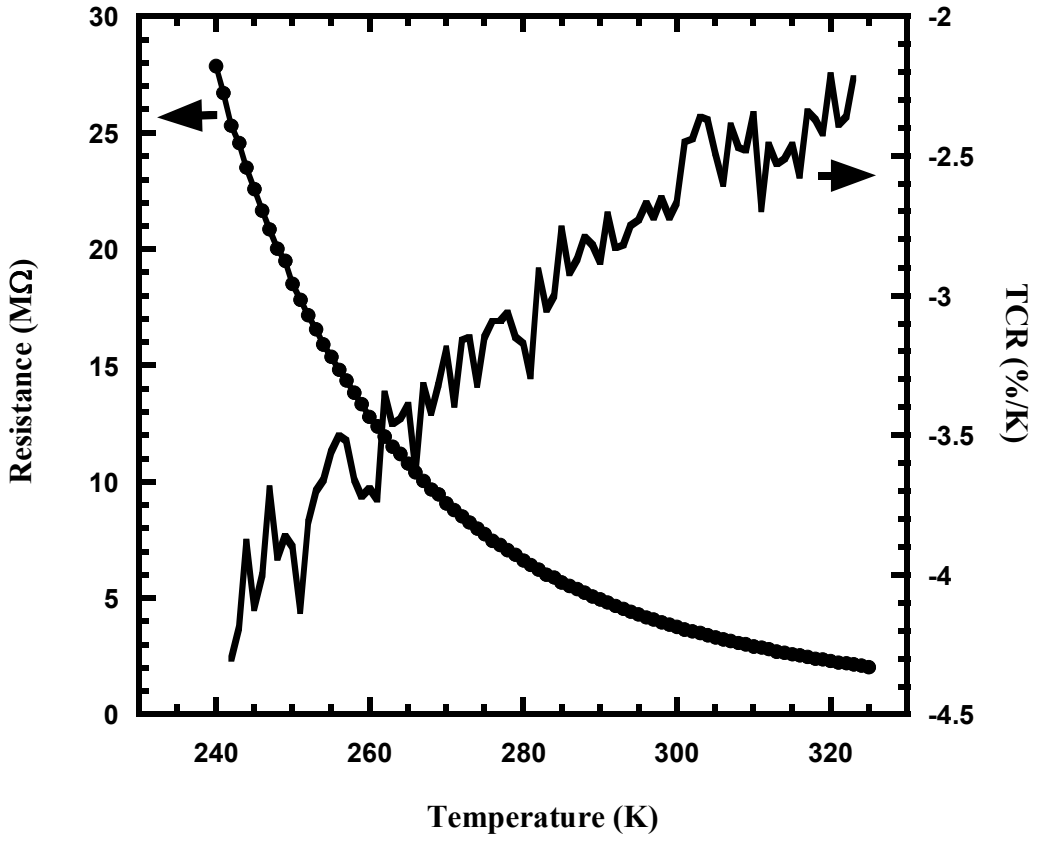

Figure 5.9 Bolometer resistance and temperature coefficient of resistance (TCR) versus temperature.

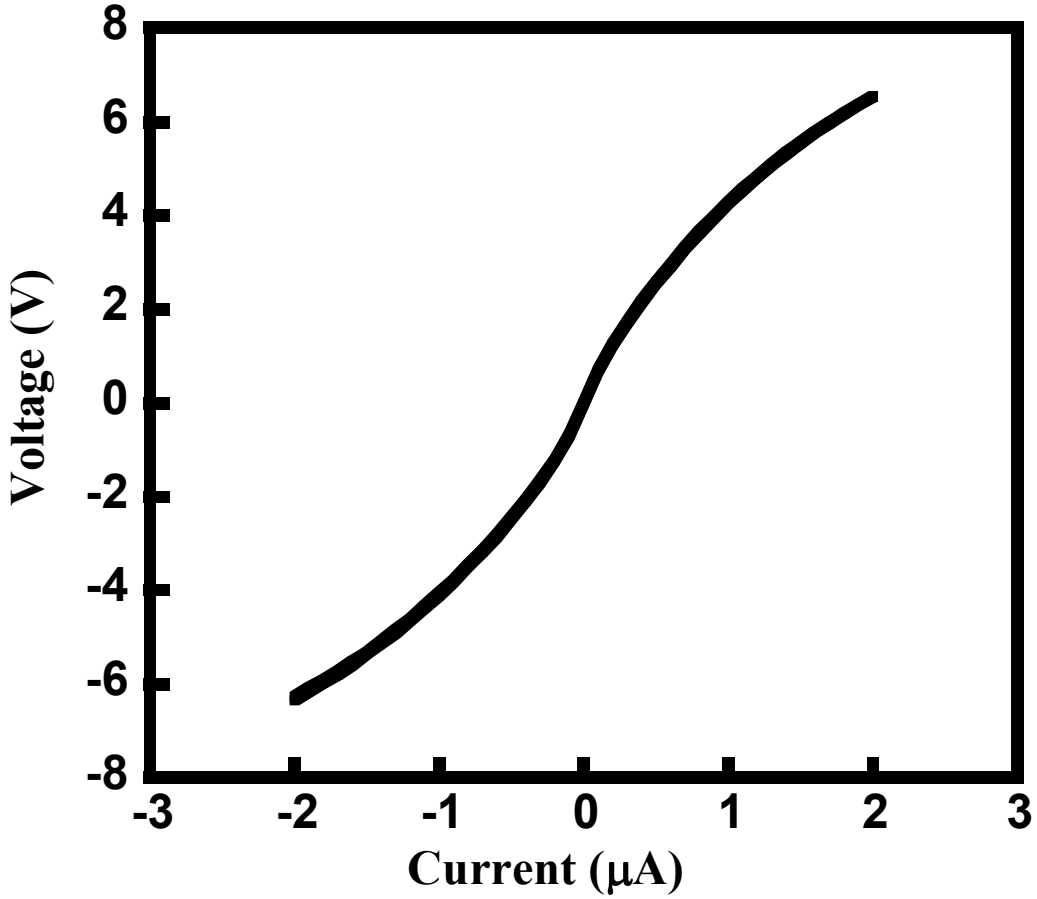

Figure 5.10 Bolometer VI characteristics. The current was swept between ±2 μA in increments of 100 nA using an HP 4155 semiconductor analyzer. Non linearity due to Joule heating is evident.

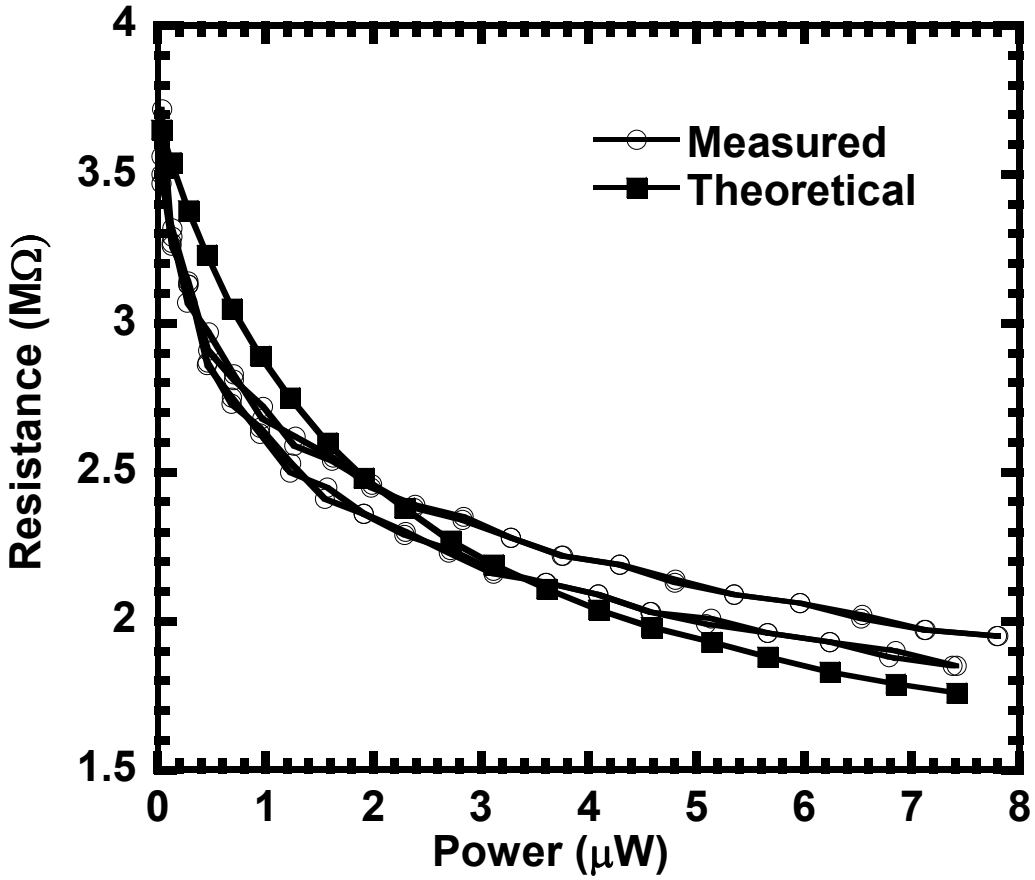

Figure 5.11 Microbolometer resistance versus power dissipated in it. The theoretical value of resistance was calculated using the mean value of $G_{th}=5.61x10^{-7}$ W/K calculated over the range of power dissipation.

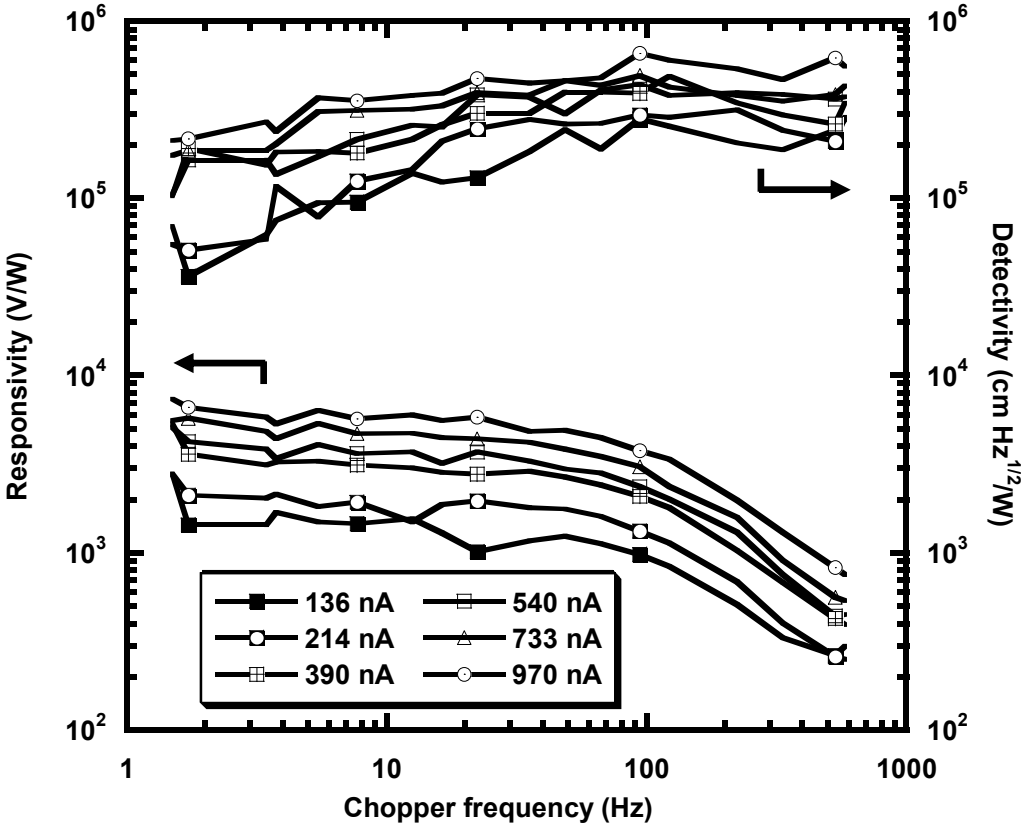

Figure 5.12 Blackbody responsivity $\mathcal{R}$ and detectivity D* of the microbolometer versus chopper modulation frequency at different bias currents.

The optical characterization was done using a blackbody IR source kept at 900°C. The detector was biased at different currents ranging from 214 nA to 970 nA. The device output was measured by a dynamic signal analyzer through a low noise preamplifier. For calibration purposes, an Oriel 70124 pyroelectric detector with a responsivity of 1000V/W was used. The device was mounted inside a cryostat and the measurements were made in air as well as in vacuum with the cryostat evacuated to ~ 100 mTorr pressure. A chopper was used to modulate the infrared signal incident on the detector. The device had a maximum voltage responsivity R_V of 9.2×10^2 V/W and 7.4×10^3 V/W in air and vacuum, respectively. The fact that there is an appreciable improvement in the detector responsivity with evacuation of air points to good thermal isolation achieved between the detector and the substrate by micromachining. The highest measured detectivity of the device in vacuum was 6.6×10^5 cmHz$^{1/2}$/W at 94.4 Hz with a bias current of 970 nA. Figure 5.12 shows the responsivity and detectivity measured in vacuum as a function of chopper frequency.

The effect of substrate heating on detector performance was also investigated. The detectors were placed in a cryostat with a ZnSe window. The cryostat was evacuated to 50mT pressure. To emulate a point source, a small aperture was placed in front of the blackbody source and a ZnSe lens was used to focus the infrared energy onto the detector. A smaller aperture would have been desirable as it would have meant higher image resolution. However, the infrared power incident on the detector was a limiting constraint. The aperture was kept at 400-500μm to keep the power incident on

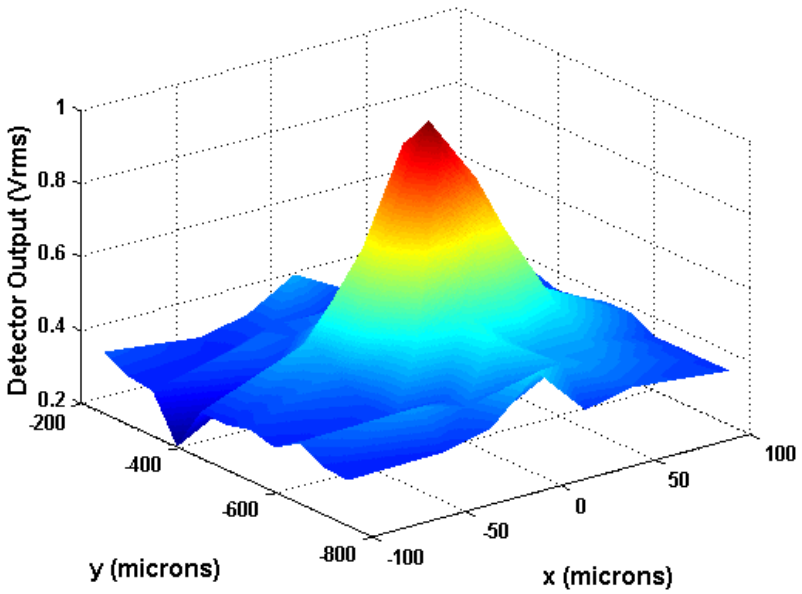

(a)

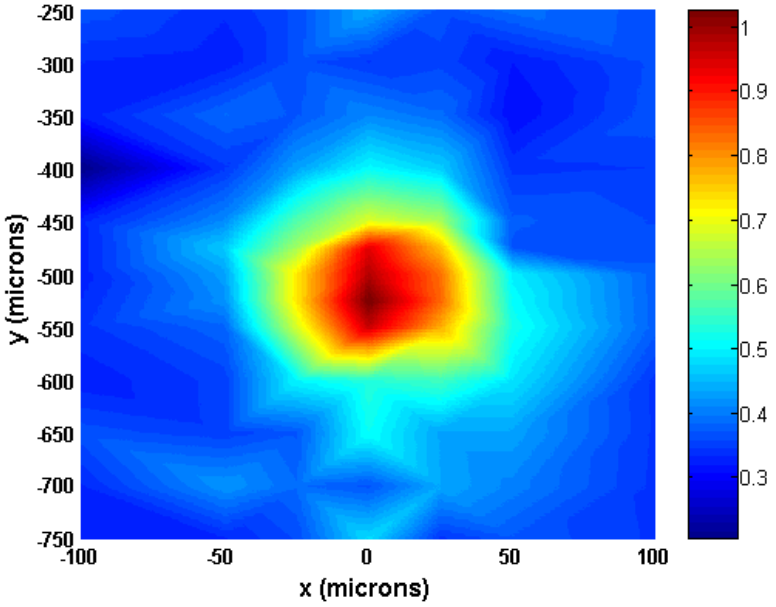

(b)

Figure 5.13 60x60 μm^2 self supporting device scanned by a point source of infrared light. (a) Isotropic view and (b) top view

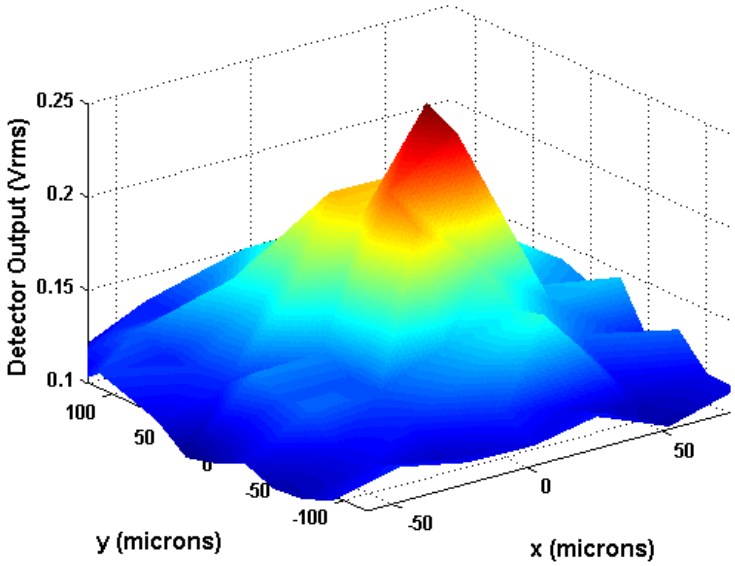

(a)

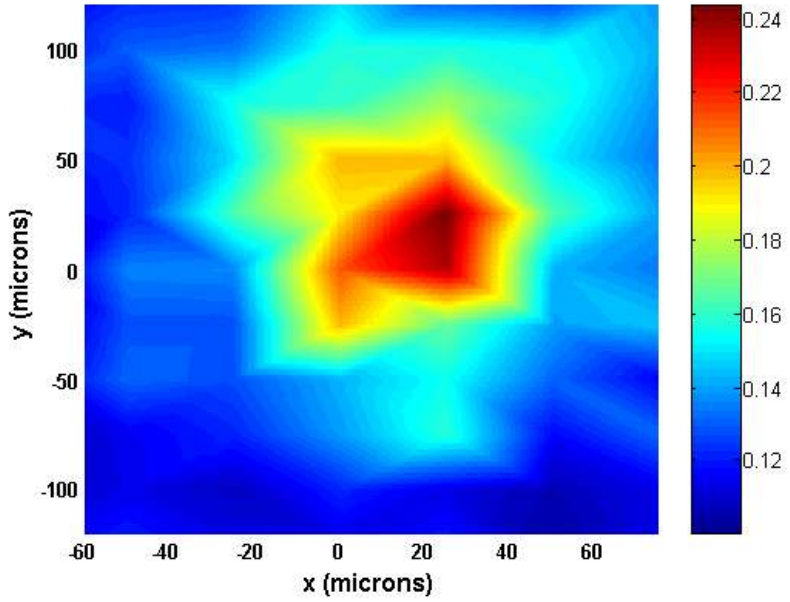

(b)

Figure 5.14 40x40μm^2 device on Si_3N_4 support membrane scanned by a point source of infrared light (a) Isotropic view and (b) top view.

the detector greater than the noise equivalent power (NEP). The lens was mounted on an XYZ-axes translational stage controlled by a Newport MM3000 motion controller. This made it possible to traverse a small spot of light on the surface of the detector while keeping the detector on the plane of optical focus. The detector was biased with 0.97 μA of current. An HP 3561A dynamic signal analyzer was used to record the detector output. A SRS 560 low noise amplifier was used to improve the signal to noise ratio before the signal analyzer. The area in the vicinity of the detector was scanned in steps of 25 μm and the detector output signal was plotted using MATLAB. The experiment was performed on two devices; a self supported 60x60 μm^2 device[30] and a 40x40 μm^2 micromachined bolometer supported by a Si_3N_4 membrane presented in this work. The images in Figures 5.13 and 5.14 show a convolution of the spot of infrared light over the area of the detector. The dimensions of the images are comparable to those of the microbolometer pixels. In vacuum environment, the self supported device is thermally connected to the ambient by the Ti arms, while the trenches in the supporting Si_3N_4 membrane isolate the detector from the ambient and minimize the effect of substrate heating. Because of good thermal isolation from the ambient, the detectors respond only to direct incident infrared radiation.

This experiment goes to prove the suitability of these devices for use in large imaging arrays. The fact that substrate heating is not a source of output signal from the detector makes them suitable candidates for larger arrays on polyimides without compromising image resolution due cross-talk between adjacent pixels.

5.4 Conclusions

The fabrication and characterization of microbolometers on flexible substrates has been presented in this chapter. These detectors were supported by thin micromachined layers of silicon nitride on flexible polyimide PI5878G. The devices were characterized for R(T), TCR, responsivity, detectivity and thermal conductance.

The device had a resistance of 3.76 MΩ and a TCR of -2.63 %/K at 301 K. The measured thermal conductance was $G_{th} = 5.61 \times 10^{-7}$ W/K. The device displayed a voltage responsivity of 9.2×10^{2} V/W. The responsivity improved to 7.4×10^{3} V/W when the same device as measured in vacuum, pointing to good thermal isolation because of the micromachining. The maximum recorded detectivity of the device was 6.6×10^{5} $cmHz^{1/2}/W$.

The effect of substrate heating on the detector response was also investigated and found to be negligible. This becomes significant in case these detectors are employed in imaging arrays where cross talk between adjacent pixels is an undesirable property.

CHAPTER 6

DEVICE LEVEL VACUUM PACKAGING

6.1 Introduction

MEMS devices generally require vacuum packaging for optimum performance. This could be for different reasons like reducing fluid viscosity and damping to cantilever beam type micro devices or to reduce thermal conductance from thermal sensors as in the present work. Vacuum packaging has been discussed in detail in chapter 3 and is generally carried out in rigid packages. The process consists of dicing the wafer, mounting the device on a suitable package, wire bonding using thermo-ionic or ultrasonic techniques followed by capping under vacuum. In case of optical/thermal detectors, the capping has to be done with a cap that is transparent in the part of the electromagnetic spectrum of interest. Chip-scale packaging has also been reported. An example is demonstrated among others by and Lee et. al.[64] and Cheng et. al.[65]. The process consists of fabricating devices on a Si wafer and applying a top glass structure in vacuum. The joints can be sealed to yield a vacuum package. Both these techniques provide satisfactory vacuum but are not suitable for use on flexible substrates since it costs the flexibility of the system. The idea of building a cavity around a detector during fabrication is presented in this chapter. Such a vacuum package shall provide a local

vacuum environment to the enclosed thermal sensor without sacrificing the flexibility of the system. Design issues addressed in this work include selection of different materials in different roles in the vacuum cavity, design of a pressure window that is optically transparent in the infrared spectrum of interest. The integrity of the vacuum element despite bending and flexing of the substrate is also investigated.

6.2 Design of a flexible vacuum cavity

A new device level packaging scheme was investigated based on the bolometers on flexible substrates explained in detail in chapter 5. The vacuum packaging is completed during the fabrication process, using a combination of conventional micromachining and deposition techniques and is fully CMOS compatible. Figure 6.1 details the process flow subsequent to the completion of the device fabrication (detailed in chapter 5). After fabricating the detector pixel, trenches are opened in the supporting nitride layer to expose the underlying sacrificial polyimide. A 1μm thick photo definable polyimide PI2737 is spun on to the wafer and patterned to form a mesa above the detector (figure 6.1(a)). A suitable lateral etch stop (LES) is then deposited on and patterned to be etched above the polyimide mesa. 0.5 μm of PI2737 is again spun on and patterned to make a larger mesa than the previous one. Another layer of the lateral etch stop (0.5 μm) is deposited and patterned to be removed above the larger mesa (Figure 6.1(b)). These steps facilitate the fabrication of a stepped LES well filled with polyimide. SOG (Spin-on-glass) and Si_3N_4 are suitable candidates in the role of the LES as they are resistant to oxygen plasma ashing used to micromachine the sacrificial PI2737 once the cavity has been formed. A layer of a mechanically strong, albeit

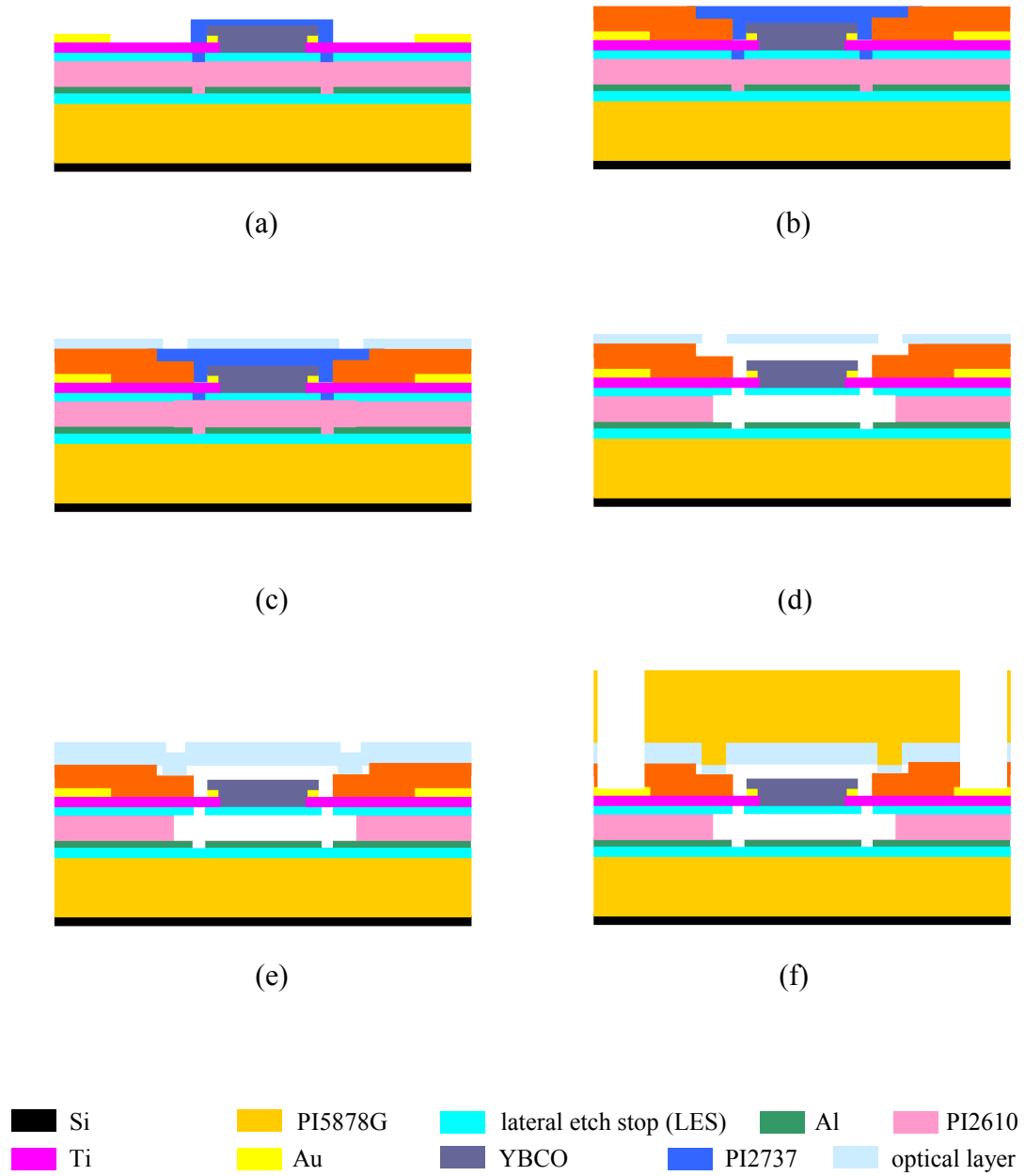

Figure 6.1 Fabrication steps of device level vacuum encapsulation (a) Sacrificial mesa (PI2737), (b) Sacrificial PI2737 filling up lateral etch stop (LES) well, (c) First layer of optical window with open trenches, (d) Fully micromachined cavity before sealing, (e) Sealed vacuum cavity, (f) Bond pads opened through superstrate PI5878G, optical layer and lateral etch stop (Dimensions not to scale).

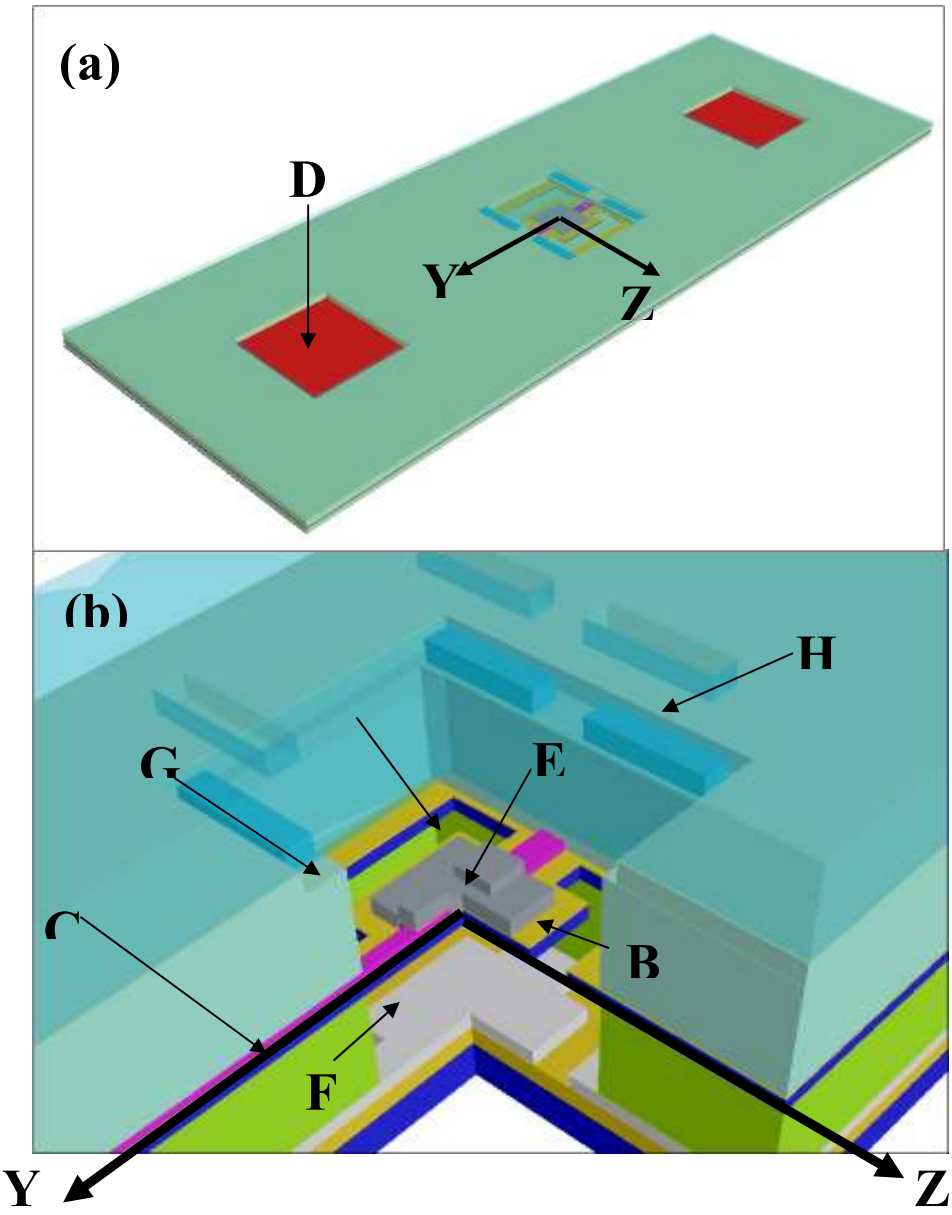

Figure 6.2 (a) Computer generated model of a device level vacuum packaged microbolometer, (a) Optical window rendered transparent and cavity magnified 20x to show detail and (b) section of a complete microbolometer showing Au bond pads. (A) Trench in support layer of Si_3N_4 and $SrTiO_3$ to facilitate micro machining under the bolometer (B) Support layer of Si_3N_4 and $SrTiO_3$, (C) Ti arm, (D) Au pad, (E) YBCO detector element, (F) Al reflecting mirror, (G) Lateral etch stop and step geometry to facilitate cavity formation above the detector, (H) Optically transparent layer of Al_2O_3 and plugs to seal the vacuum cavity.

optically transparent material, can then be deposited to form the optical window. Slits can be opened in the optical layer to expose the sacrificial polyimide that can be removed by oxygen plasma ashing (Figure 6.1(c)). The lateral etch stop (LES) will limit lateral micromachining and direct the ashing through the open trenches towards the sacrificial polyimide supporting the detector from underneath (Figure 6.1(d)). Upon completion of the micromachining process, the slits opened in the optical layer can be sealed shut by sputtering some more of the same material. This yields a vacuum cavity evacuated to the sputtering pressure of 10 mT and encapsulated by an optical window (Figure 6.1(e)). Polyimide PI5878G can then be spun onto the wafer to yield the superstrate. The polyimide superstrate provides mechanical strength to the vacuum cavity. It will also help keep the detector close to the zero-strain plane[25]. Bond pads can be opened for subsequent characterization (Figure 6.1(f)). Figure 6.2(a) shows a computer generated model of a device level vacuum packaged micromachined microbolometer, while the interior details of the proposed vacuum cavity can be seen in Figure 6.2(b). Given the glass transition temperatures of 400°C and 360°C of PI5878G and PI2610 polyimides respectively, the detectors could be baked at a suitable lower temperature prior to vacuum sealing. This would reduce outgassing in the vacuum cavity without affecting the stoichometry of the sensitive YBCO. The impact of baking on the quality of the vacuum over an extended period of time would need to be investigated in subsequent work.

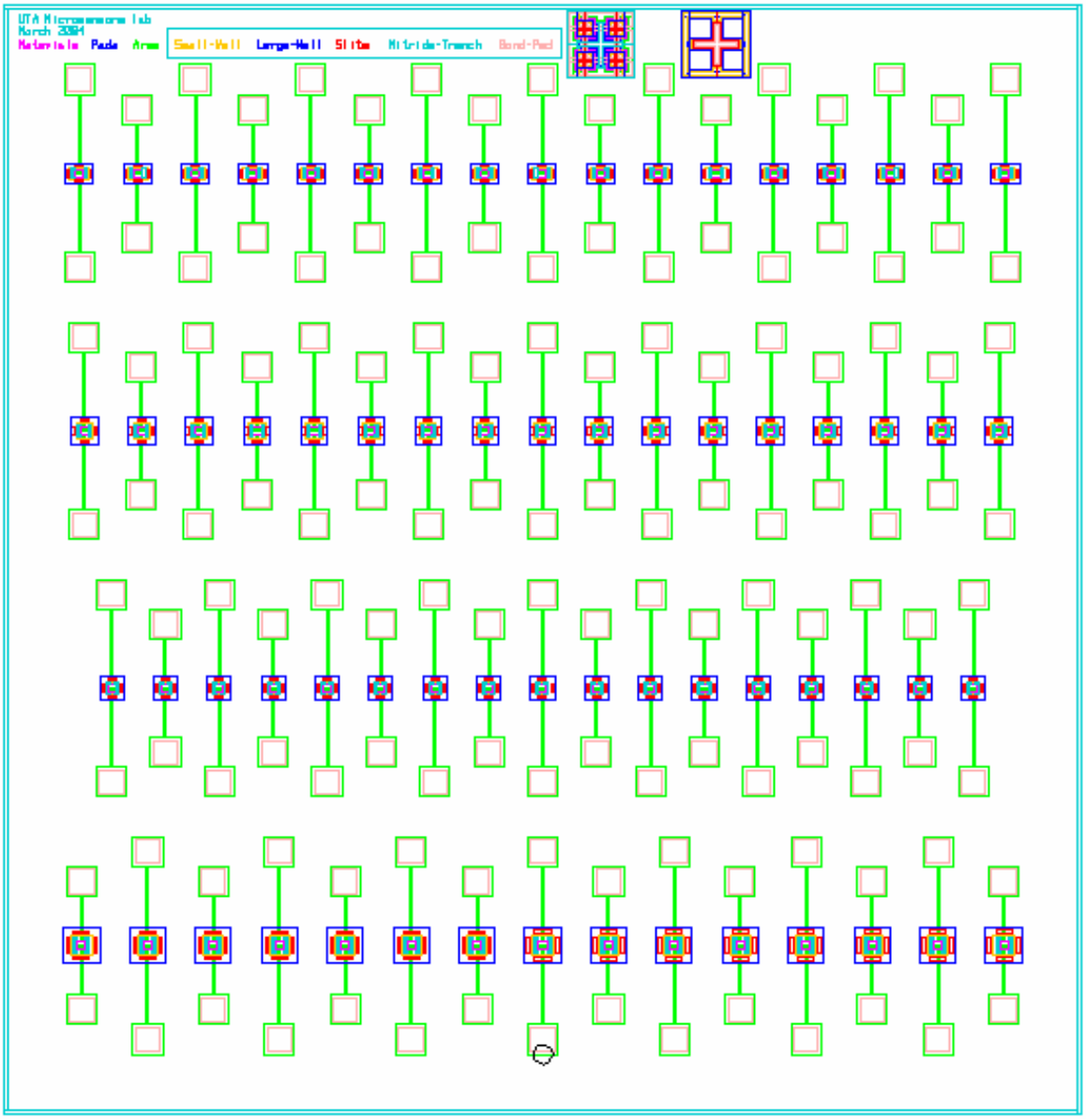

Figure 6.3 Die layout

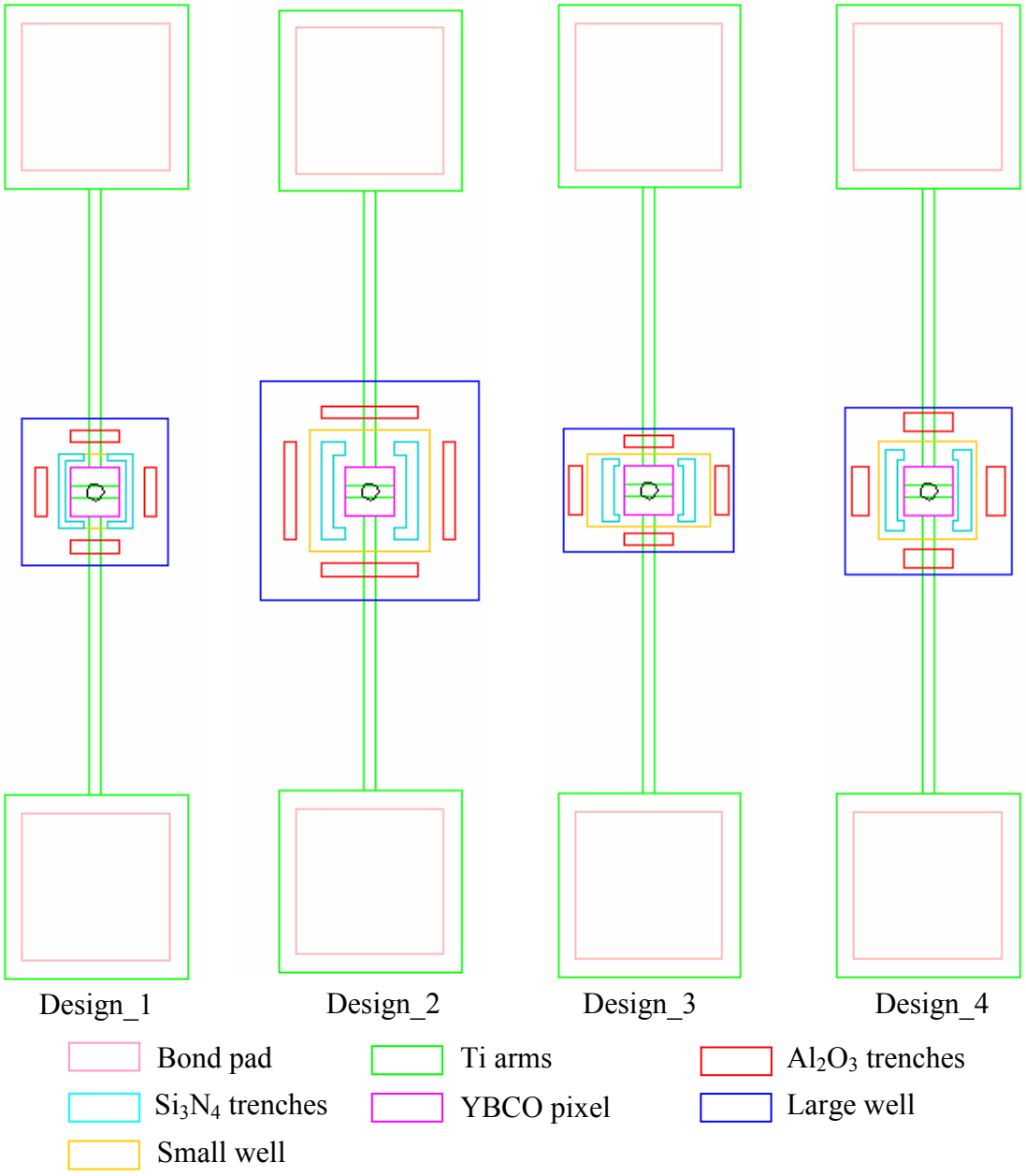

Figure 6.4 Different cavity layouts.

6.3 Mask design

A set of eight 5" optical masks were prepared for the fabrication process. The masks were designed using CoventorWare® and were fabricated by a commercial firm. The bolometer size was kept at 40x40 μm^2. Four different types of vacuum cavities were designed to observe different rates of micromachining through the different trenches of different polyimide masses. There were a total of 380 dies in the 5" mask arranged in a grid of 19 rows and 20 columns. Each die was 5360 μm wide and 5536 μm high. Adjacent dies were separated by a 20 μm scribe line. Each die was uniquely numbered from 1 to 380. Figure 6.3 shows the layout of a single die. Figure 6.4 shows the four different device layouts.

6.4 Design analyses

The design was analyzed for the optical transmission properties of the pressure window as well as the structural integrity of the vacuum cavity. The thermal conductance from the detector to the substrate was also investigated.

6.4.*1 Design of the pressure window*

The design of the vacuum cavity largely depends on the optical and mechanical properties of the material chosen to form the optical window. The optical window will have to withstand a pressure differential of approximately 1 atm across a thickness of 2-3 μm. From chapter 4 we see that the thickness of an unclamped pressure window is given as

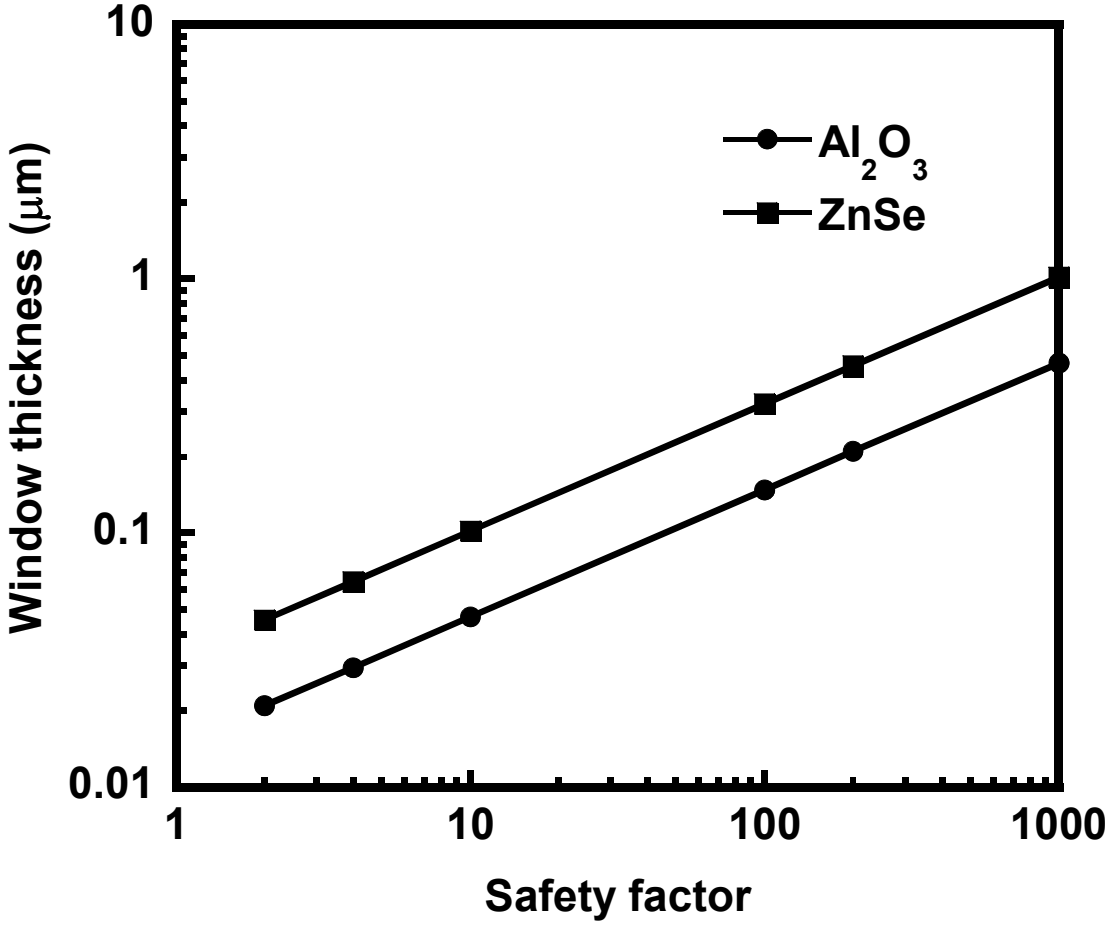

Figure 6.5 Pressure window thickness as a function of safety factor.

$$T = L\sqrt{\frac{SF \times K}{2}}\sqrt{\frac{P}{F_a(1+W^2)}} \tag{6.1}$$

where T is the window thickness, L and W are the window lateral dimensions (length and width), $K = 1.125$ is an empirical constant depending upon the method of support of the pressure window (clamped or unclamped), P is a uniform pressure applied to the window surface, SF is the safety factor, $F_a = SF \times S_{\max}$ is the apparent elastic limit of the window material with a maximum allowable stress of $S_{\max}$. The window thickness depends upon the window dimensions and also upon the material used to make the window. For 100x100μm^2 windows made of ceramic Al_2O_3 and ZnSe, Figure 6.5 gives the pressure window thickness as a function of the safety factor for a constant uniform pressure of 1 atm. The apparent elastic limit of 260 MPa (the tensile strength of ceramic Al_2O_3) and 55 MPa (the apparent elastic limit of ZnSe) have been used for the materials respectively. There was negligible change in the design thickness on increasing the window area to up to 200x200 μm^2 in size. Equation (6.1) gave an initial guess to the minimum window thickness required for the vacuum cavity.

6.4.*2 Optical properties of the pressure window*

The optical transmission properties of thin Al_2O_3 films have been reported by Fuertes et. al[77] . These films were prepared by spray pyrolisis. Different samples of Al_2O_3 were prepared locally in the University of Texas at Arlington nanofab cleanroom. The films were deposited on Si wafers by rf magnetron sputtering in a pure Ar environment. The rf power was kept at 100W to prevent overheating of the ceramic

Al_2O_3 target. The Ar was introduced into the chamber at a rate of 37 standard cubic centimeters per minute (sccm) and the sputtering was carried out at 10 mT pressure. The sputter rate for the above settings was determined to be ~ 750-800 Å/hr. Two samples of different thicknesses were prepared. In one sample the sputtering was done for 30 mins while for the second sample, the sputtering was done for 10 min in the same conditions. The expected thickness of the two samples were around 400 Å and 114 Å respectively. Infrared variable angle spectroscopic ellipsometery was used to extract the constituent parameters (relative permittivity $\varepsilon_r = \varepsilon' - i\varepsilon''$). The data fit was achieved for thicknesses of 390 Å and 110 Å respectively. Figure 6.6 shows the two parameters plotted as a function of wavelength. The extracted film thicknesses are also close to the expected thicknesses based on rates established using the same deposition parameters with a step profile with a profilometer.

The optical transmission characteristics of the polyimide PI 5878G were also measured using a QTH infrared source and a Oriel monochromator. The thickness of the polyimide film depends on the spin speed of the wafer at the time of application. The liquid polyimide was poured onto the wafer which was then spun at 2000 rpm for ~50 s. It was then pre baked at 110°C for 6 min. The process was repeated 5 times before the polyimide coated wafer was loaded into an oven preheated to 110°C for post bake. The oven temperature was steadily increased to ~265°C over the next hour and kept at that temperature for about 5 hours. The expected final polyimide thickness was ~ 40 μm. The polyimide film was peeled off the wafer for characterization. Figure 6.7

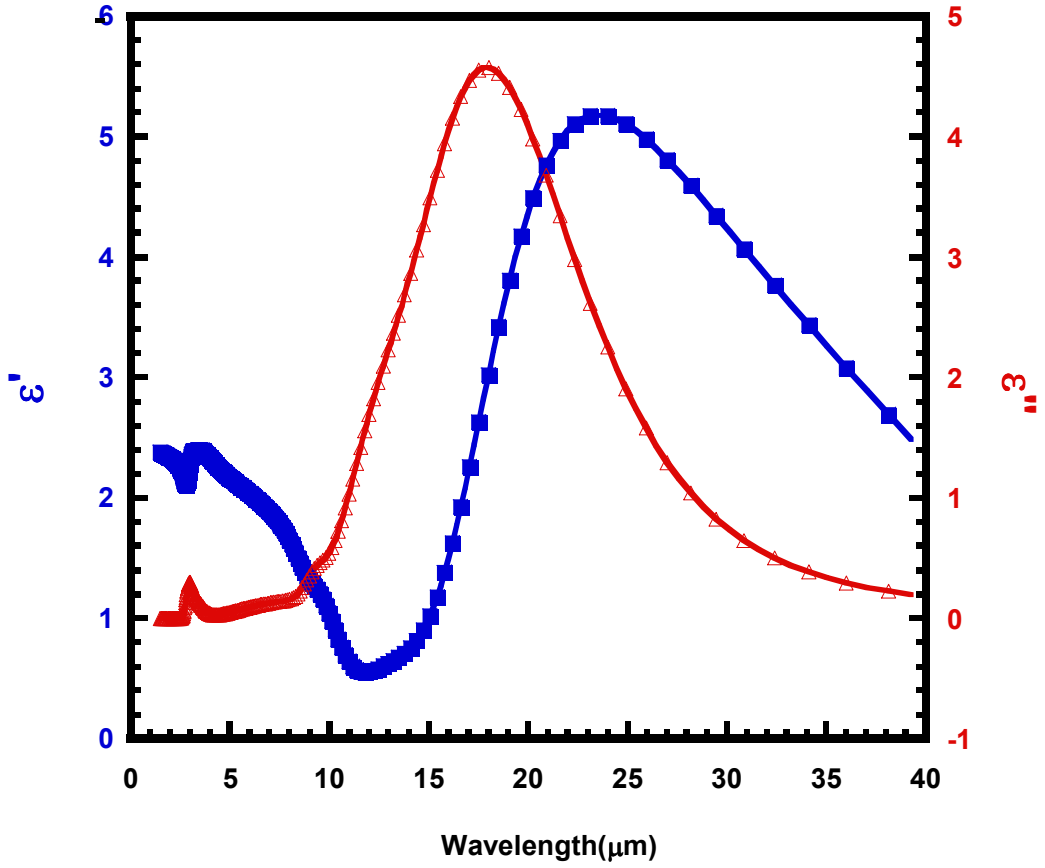

Figure 6.6 Real (ε′) and imaginary (ε″) parts of the complex relative permittivity (ε_r) of ceramic Al_2O_3 sputtered in a pure Ar environment at room temperature. Data was extracted using infrared variable angle spectroscopic elipsometery using a J.A. Woollam IRVASE system.

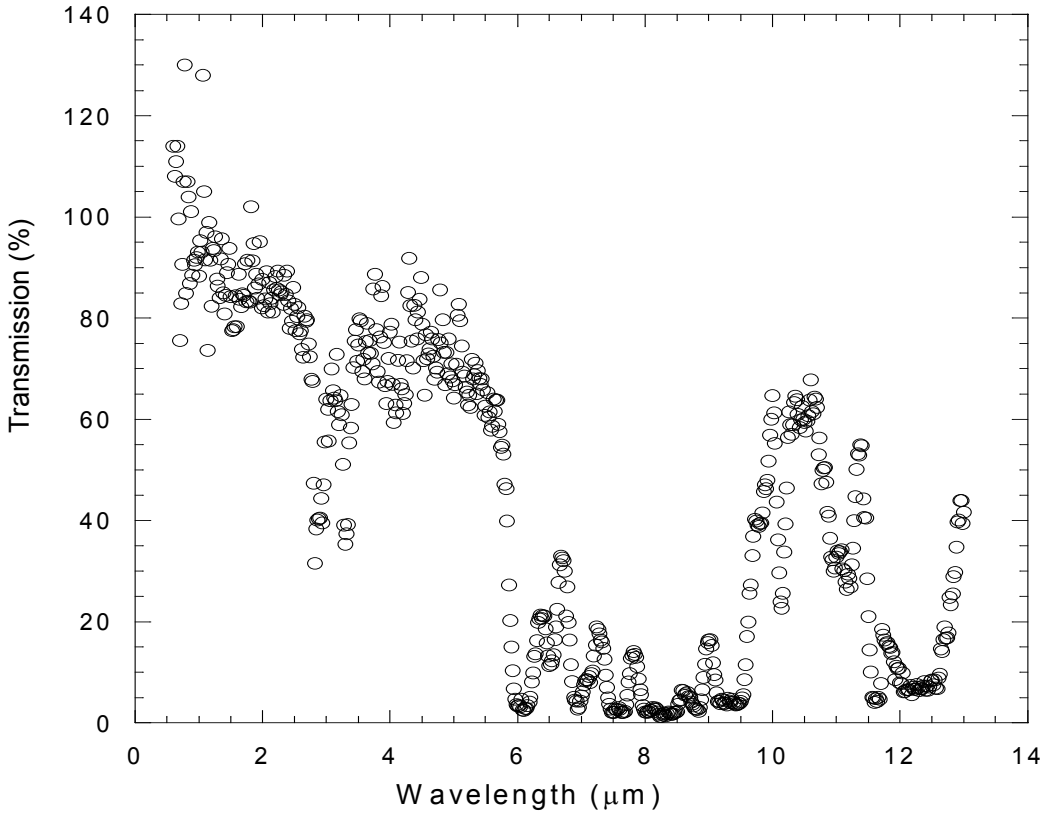

Figure 6.7 Measured optical transmission characteristics of 40μm PI5878G.

shows the transmission properties of the film. There are transmission windows in the near to mid infrared region up to 5μm as well as another transmission window in the far infrared region around 11 μm. Future work to tune the bolometer for maximum absorption in one of the transmission windows of the superstrate material needs to be done.

6.4.3 Thermal analysis

The thermal conductance G_{th} from the bolometer to the substrate was also calculated from the model. The equation used was

$$G_{th} = k\frac{A}{l} \tag{6.2}$$

Where k is the material thermal conductivity, l and A are the heat conduit length and cross sectional area respectively. Figure 6.8 shows the cross section of a device-level vacuum-packaged microbolometer. The microbolometer serves as a heat source while the bulk of the device package acts as a heat sink. Keeping in view the fabrication process, the extent of micromachining, and the presence of air in the vacuum cavity are factors that can affect G_{th}. Different conditions ranging from perfectly micromachined microbolometers in vacuum (called the best case), to microbolometers resting atop residual sacrificial polyimide (due to incomplete micromachining) and surrounded by air (due to a ruptured cavity and called the worst case) have been analyzed. There are different paths for heat flow from the source to the sink as have been shown in Figure 6.8. An equivalent thermal circuit is shown in Figure 6.9.

G_A is the thermal conductance from the bolometer (thermal source) to the top of the Al_2O_3 column (thermal sink) resting on top of the Ti electrode and the support Si_3N_4 layer. To simplify the thermal analysis, the top of the Al_2O_3 columns is assumed

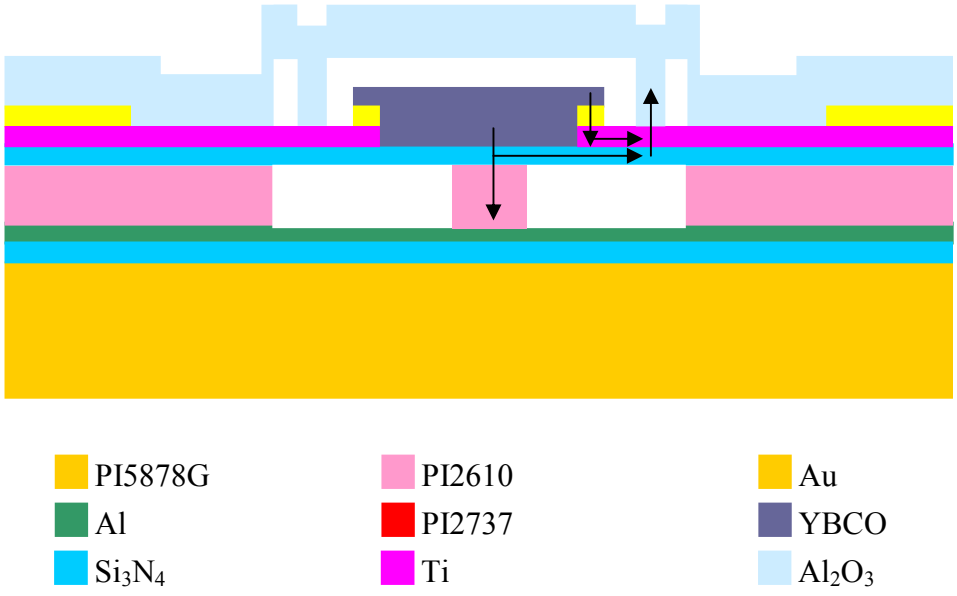

Figure 6.8 Cross sectional view of a device level vacuum packaged micromachined microbolometer. Different paths of heat transfer are also shown.

to be the thermal sink. The heat conduit consists of the Au pad between the YBCO pixel and the Ti arm, the Ti arm and the Al_2O_3 column.

The heat conduit used for calculating G_B consists of the Au pad between the YBCO pixel and the Ti arm, the Ti patch between the Au patch and the support Si_3N_4, the support Si_3N_4 and the Al_2O_3 column.

The heat conduit used for calculating G_C consists of the support Si_3N_4 and the Al_2O_3 column.

G_D is the thermal conductance that comes into play in case of incomplete micromachining resulting in a column of residual sacrificial polyimide between the support Si_3N_4 membrane and the Al mirror. The heat conduit consists of the support nitride layer and the sacrificial PI2610 column. The YBCO bolometer is the heat source while the heat sink is the Al mirror.

In case of the presence of air in the vacuum cavity, there will be additional thermal conductance in addition to the above mentioned.

G_E is the thermal conductance from the microbolometer to the cavity Al_2O_3 optical window. The heat conduit is a column of air between the thermal source and sink.

G_F is the thermal conductance from the bolometer to the Al mirror. The Au and Ti patches, the support nitride and the column of air between the support nitride and the Al mirror constitute the heat conduit.

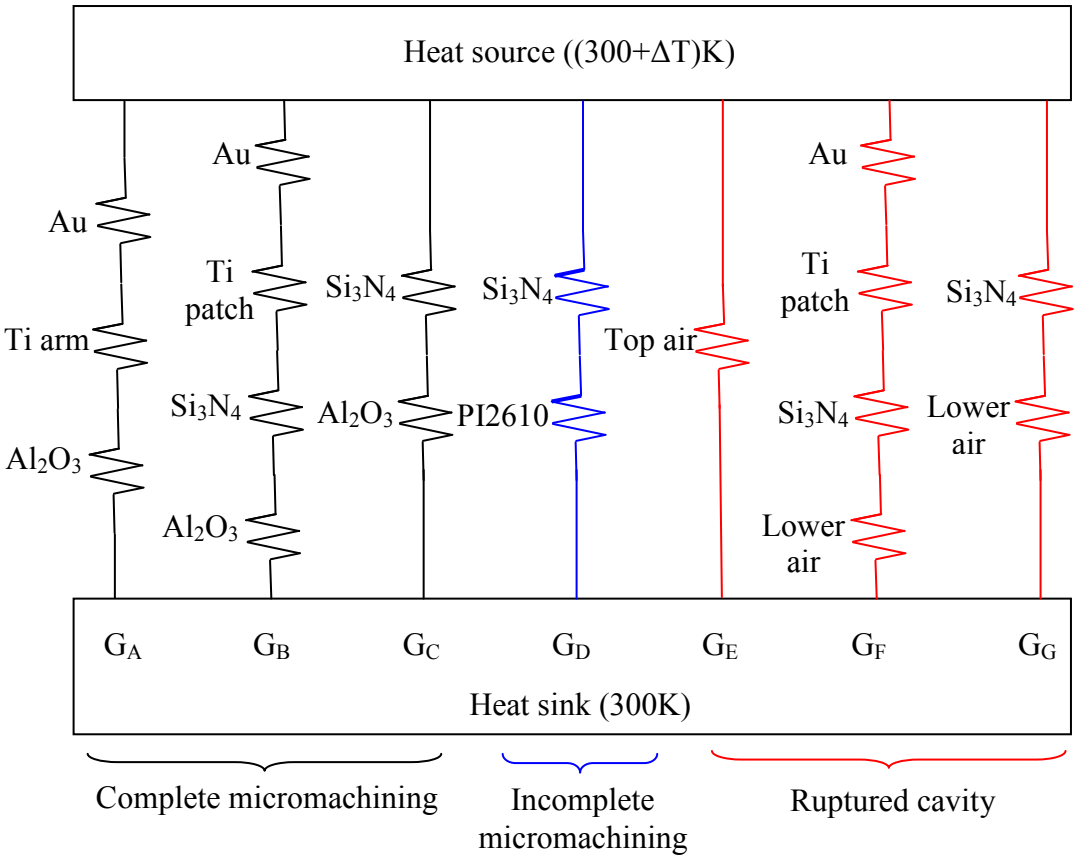

Figure 6.9 Thermal equivalent circuit of a device level vacuum packaged microbolometer.

G_G is the thermal conductance from the bolometer to the Al mirror. The support nitride and the column of air between the support nitride and the Al mirror constitute the heat conduit.

The results of the analytic thermal calculations are summarized in Table 6.1. Design_1 showed best and worst case thermal conductances of 4.01×10^{-6} W/K and 2.36×10^{-4} W/K respectively. Design_2 had best and worst case thermal conductances of 5.10×10^{-6} W/K and 2.38×10^{-4} W/K respectively. Due to the short heat conduit in Design_3, the best and worst case thermal conductances were 1.12×10^{-5} W/K and 2.44×10^{-4} W/K respectively. Design_4 had best and worst case thermal conductances of 6.16×10^{-6} W/K and 2.39×10^{-4} W/K respectively. Another important finding of these calculations was that the thermal conductances for fully micromachined devices in a ruptured cavity (device surrounded by air) were in the range of 1.43×10^{-4} W/K to 1.50×10^{-4} W/K. The best case thermal conductance was also calculated to be 5.1×10^{-6} W/K using FEM (Figure 6.10). This was done by fixing the bolometer temperature at 301K and that of the sink at 300K. The heat (power in Watts) flow through the sink boundary was measured. The result is in good agreement with the analytic calculation from the thermal model. The very obvious difference between the thermal conductances from the device to the substrate due to the presence or absence of vacuum are a useful gauge of the quality of the vacuum cavity after it is fabricated.

Table 6.1. Calclated thermal conductances G_{th} for different vacuum packaged microbolometers

	Device_1		Device_2		Device_3		Device_4	
	Vacuum	Air	Vacuum	Air	Vacuum	Air	Vacuum	Air
Ti, Si_3N_4 (complete micromahining)	4.01×10^{-6}	1.43×10^{-4}	5.10×10^{-6}	1.44×10^{-4}	1.12×10^{-5}	1.50×10^{-4}	6.16×10^{-6}	1.45×10^{-4}
Ti, Si_3N_4, $100\mu m^2$ PI2610	1.20×10^{-5}	1.48×10^{-4}	1.31×10^{-5}	1.50×10^{-4}	1.92×10^{-5}	1.56×10^{-4}	1.42×10^{-5}	1.51×10^{-4}
Ti, Si_3N_4, $400\mu m^2$ PI2610	3.60×10^{-5}	1.66×10^{-4}	3.71×10^{-5}	1.67×10^{-4}	4.32×10^{-5}	1.73×10^{-4}	3.81×10^{-5}	1.68×10^{-4}
Ti, Si_3N_4, $900\mu m^2$ PI2610	7.59×10^{-5}	1.95×10^{-4}	7.70×10^{-5}	1.97×10^{-4}	8.31×10^{-5}	2.03×10^{-4}	7.80×10^{-5}	1.98×10^{-4}
Ti, Si_3N_4, $1600\mu m^2$ PI2610	1.32×10^{-4}	2.36×10^{-4}	1.33×10^{-4}	2.38×10^{-4}	1.39×10^{-4}	2.44×10^{-4}	1.34×10^{-4}	2.39×10^{-4}

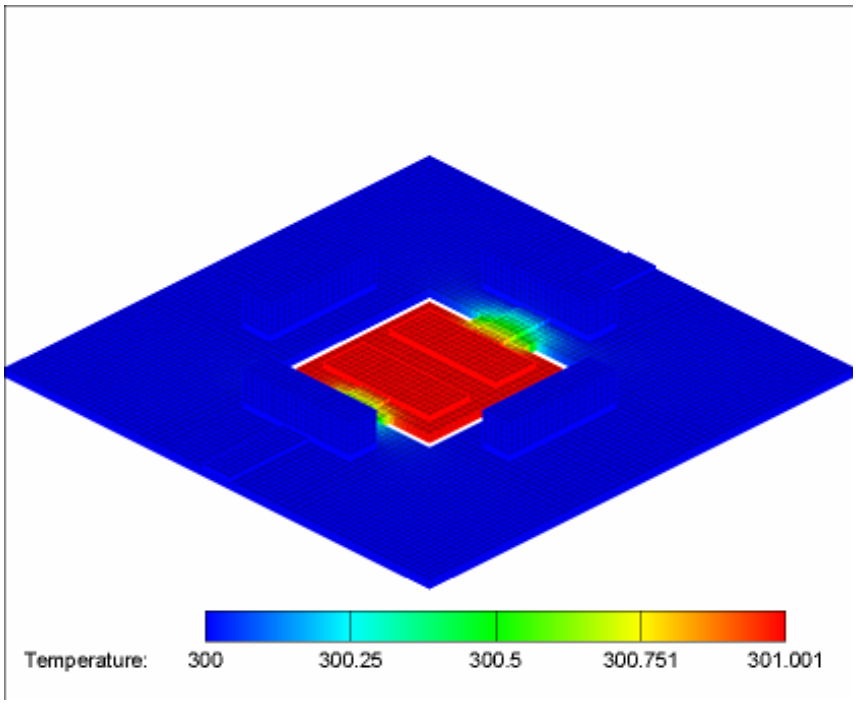

Figure 6.10 CoventorWARE® model of a micro cavity for thermal analysis.

6.4.4 Structural analysis

For the vacuum cavity to survive when subjected to the atmospheric pressure and the weight of the superstrate polyimide, the stresses induced on this window should be less than the yield stress of the material. This was investigated using computer simulations. A model of the vacuum package was created using CoventorWare® and analyzed to study feasibility (Figures 6.11). CoventorWare® creates a 3-D model using 2-D layout masks and a process flow based on deposit and etch steps. It employs finite element analysis for numerical computations. Table 6.2 lists the material properties employed for the simulations.

Based on the mechanical strength and optical transmission characteristics, materials suitable for the role of the optical window include Al_2O_3, ZnSe and Si. Amorphous Al_2O_3 has over 90% optical transmission in the infrared region up to 15 μm[77], while ZnSe has an optical transmission range up to 22 μm[7879]. Si has an optical transmission range up to 15 μm[75, 78]. All of these materials can be deposited by rf sputtering. The transmission properties of ZnSe and Si have been quoted for a single crystal material and would be poorer for amorphous films deposited by sputtering. For simulation purposes, optical window lateral dimensions were kept 100x100 μm^2 and a thickness of 2.5 μm was used. The top surface of the model was exposed to 1 atm pressure. The stress in the the optical window was computed using finite element analysis. Both Al_2O_3 and ZnSe were tested as a window material. It was concluded that Al_2O_3 is the more appropriate material as the stresses developed were less than the tensile strength of 260 MPa[78].

To mimic bending of the flexible substrate, one edge of the vacuum element was fixed in space while the opposite edge was moved towards the former edge along a straight line. Figure 6.11 shows a sample of the simulation. Despite being part of the original simulation, the optical window as well as the superstrate have been removed to show the cavity interior details. The stresses produced in the optical window were noted as a function of the radius of curvature which was in turn calculated from the measured linear displacements along the y and z axes. The bending was assumed to be circular and details of the calculation are given in APPENDIX A. Stresses produced in the Al_2O_3 optical window as a function of the radius of curvature are shown in Table 6.3. It

can be seen that the stresses produced in the optical window are less than the tensile strength of the material until the radius of curvature of the bent optical window is ~ 12 mm. This means the Al_2O_3 window will be able to hold the vacuum intact even when the cavity is bent over a radius of curvature of ~10-12 mm. This proves the feasibility of using Al_2O_3 in the role of an optical window to form a device level vacuum cavity around a micromachined microbolometer on a flexible substrate that can be applied to curved host surfaces.

Similar analysis with a ZnSe optical window showed a failure of the optical window because crystalline ZnSe has much lower yield strength of 55 MPa[78].

6.5 Fabrication

An implementation of this design was repeatedly attempted during fabrication. Initially spin-on-glass (SOG) was used as the LES to form the polyimide well. Honeywell products AccufloT11 and T12B were used for this purpose. However, the cast glass cracked due to thermal stresses during curing. This was because of the difference in the coefficient of thermal expansion of the SOG and the underlying polyimide. An attempt was then made to create the LES well using sputtered Si_3N_4 as the lateral etch stop instead of the SOG. This process also failed because although there was no thermal curing involved in it, the nitride cracked and broke up due to the large thickness. At this stage, it was felt that the process had to be modified and a new vacuum cavity was designed that used the existing masks. A bubble canopy replaced what had earlier been a sunken cavity. Figures 6.12 and 6.13 detail the modified

Table 6.2. Material properties used for finite element method (FEM) simulations

Material	Density ($kg/\mu m^2$)	Young's modulus E (MPa)	Poisson's ratio σ	Temp. coeff. of expansion TCE (%/K)	Thermal conductivityG (pW/(μmK))	Specific heat (pJ/kg.K)
Al	$2.7x10^{-15}$	$7.0x10^{4}$	0.30	$2.4x10^{-5}$	$2.4x10^{8}$	$9.0x10^{14}$
Al_2O_3	$4.0x10^{-15}$	$3.8x10^{5}$	0.24	$8.0x10^{-6}$	$2.5x10^{7}$	$7.7x10^{14}$
Au	$1.9x10^{-14}$	$8.0x10^{4}$	0.35	$1.4x10^{-5}$	$3.2x10^{8}$	$1.3x10^{14}$
Glass	$2.3x10^{-15}$	$5.2x10^{4}$	0.17	$5.9x10^{-7}$	$1.4x10^{6}$	$8.4x10^{14}$
Polyimide	$1.0x10^{-15}$	$7.5x10^{3}$	0.35	$3x10^{-6}$	$1.1x10^{5}$	$1.1x10^{15}$
Si_3N_4	$3.2x10^{-15}$	$2.9x10^{5}$	0.25	$2.1x10^{-6}$	$5.0x10^{7}$	$7.1x10^{14}$
Ti	$4.5x10^{-15}$	$1.1x10^{5}$	0.33	$8.4x10^{-6}$	$2.2x10^{7}$	$5.2x10^{14}$
YBCO	$6.1x10^{-15}$				$7.1x10^{6}$	$1.8x10^{16}$
ZnSe	$5.3x10^{-15}$	$7.0x10^{4}$	0.28	$7.1x10^{-4}$	$1.8x10^{7}$	$3.4x10^{14}$

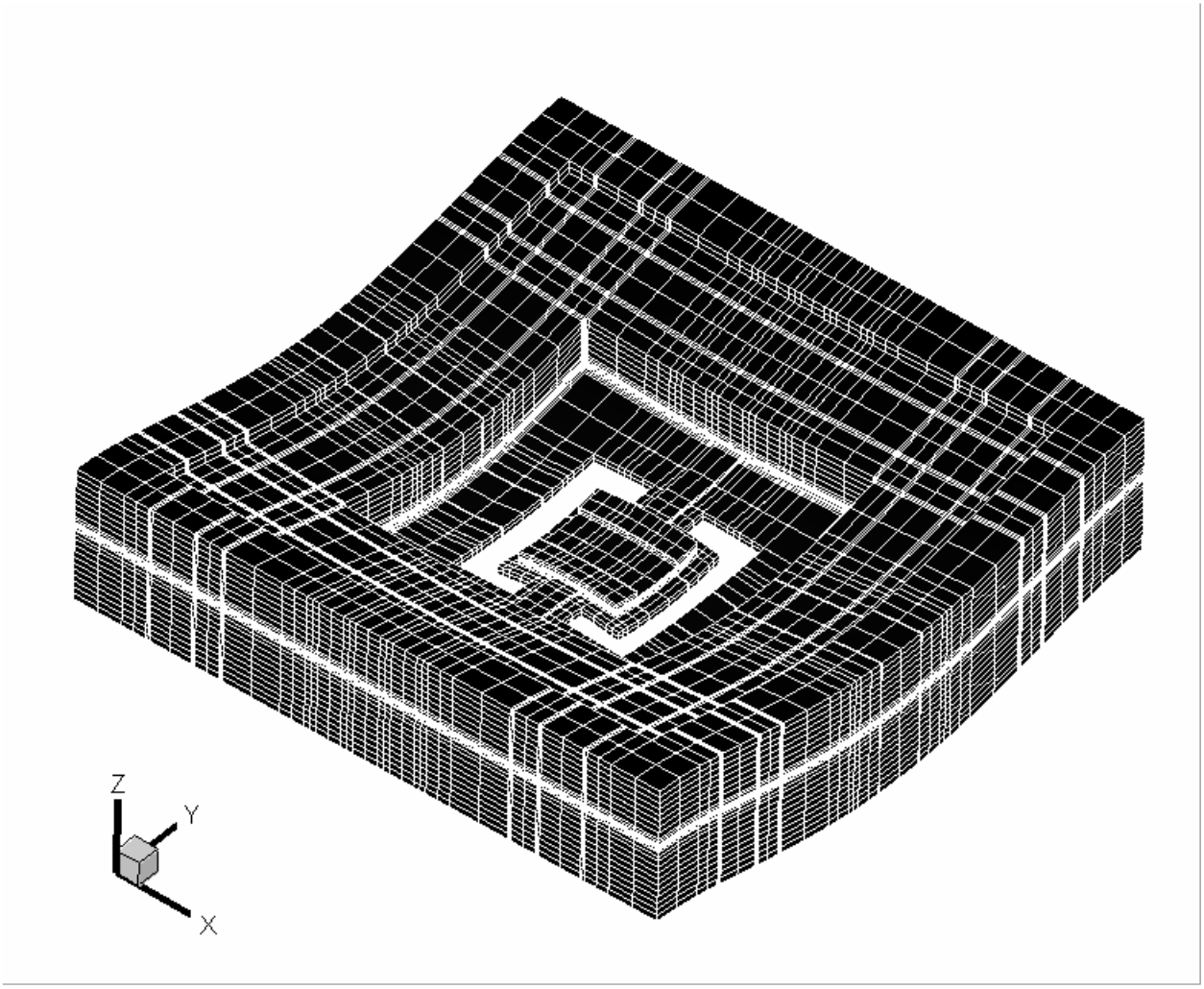

Figure 6.11 CoventorWARE® model of a flexible micro cavity.

Table 6.3 Induced Von Mises stress in bent microcavity optical window made of Al_2O_3. Al_2O_3 has a tensile strength of 260 MPa.

Radius of curvature (mm)	Max Mises Stress (MPa)
48.0	30
12.0	44
7.0	990
5.1	1300
4.2	1500
3.6	1600
3.2	1800
2.9	2000
2.6	2100

fabrication process flow. Liquid polyimide PI 5878G is used to form the flexible substrate by spin casting onto a Si wafer. A spin speed of 2500 rpm was used for spin casting followed by a soft bake at 115°C for six minutes. This combination corresponds to a thickness of 6 μm for cured polyimide. This process was repeated four times before loading the wafer into an oven preheated at 115°C. The oven temperature is gradually increased up to 275°C and the polyimide is cured for five hours. The final polyimide thickness was 24 μm. The glass transition temperature of the polyimide is about 400°C which is safe enough to protect the polyimide from reflow downstream. Rf sputtering was used for all depositions during fabrication except the Al mirror which was

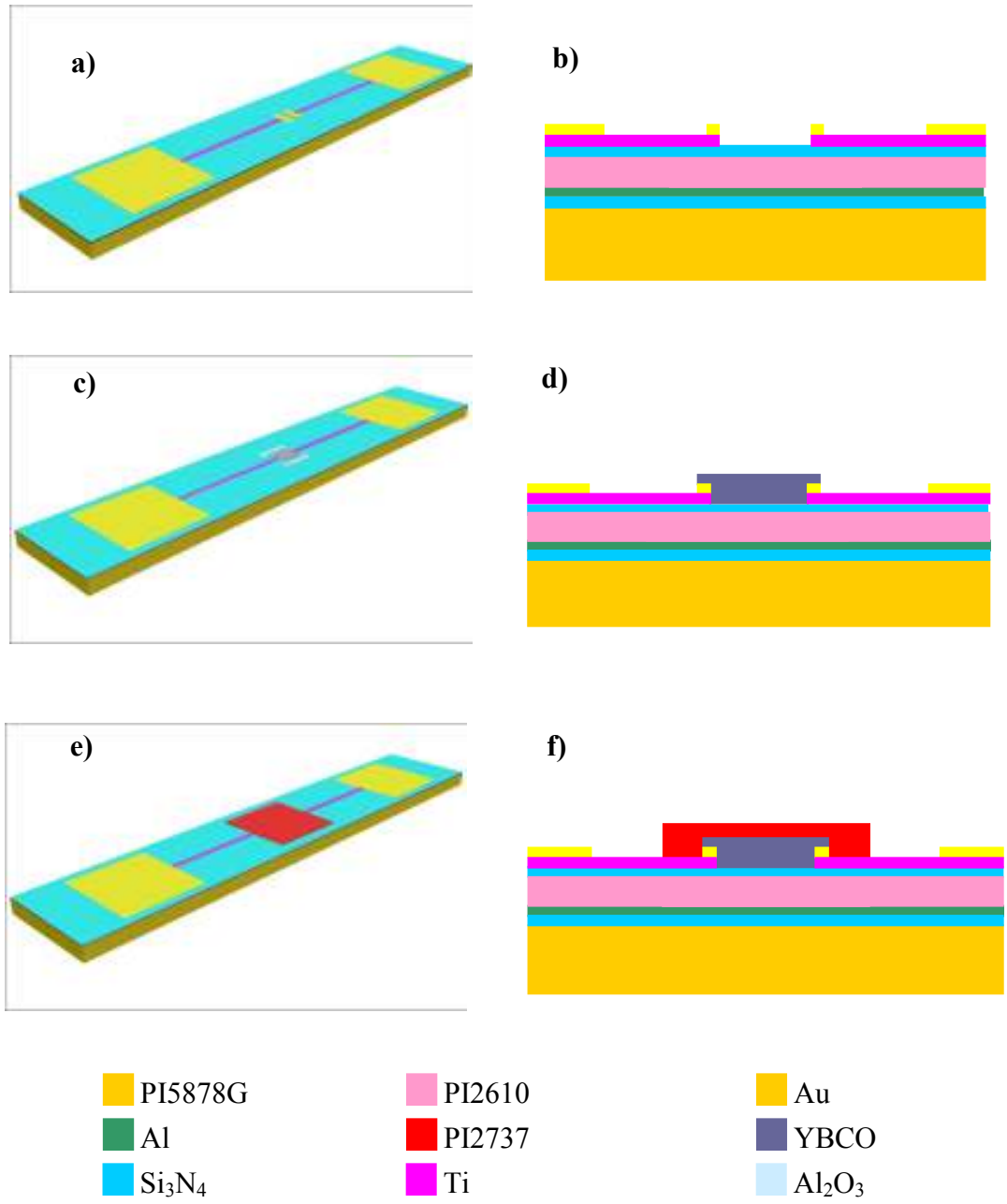

Figure 6.12. Modified process flow: a) Model of Ti arms and Au bond pads and contacts, b) sectioned view through the center of model, c) Model of YBCO pixel, d) sectioned view through the center of model, e) Model of photodefinable PI2737 sacrificial mesa, f) sectioned view through the center of model. (Dimensions not to scale)

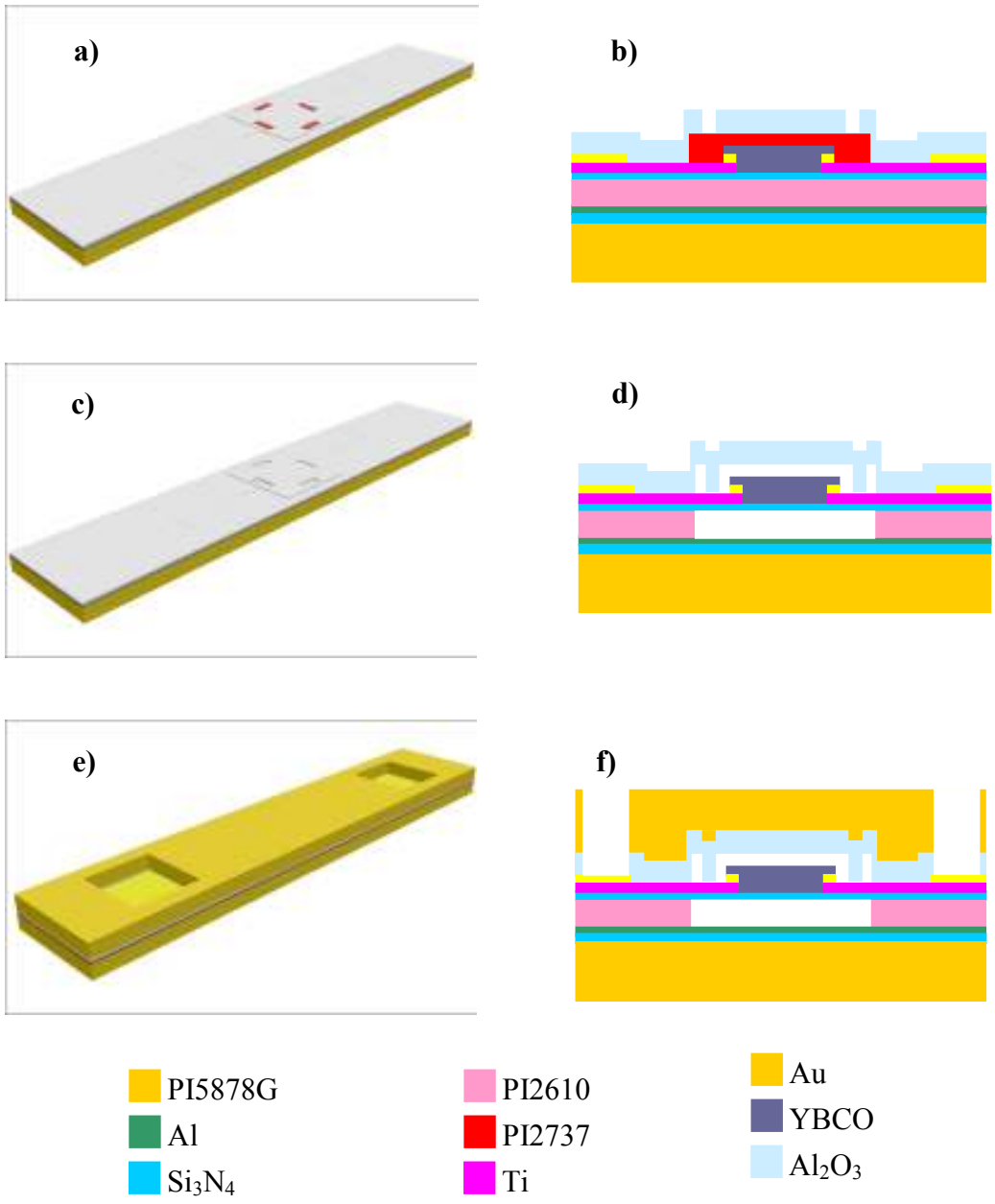

Figure 6.13 Modified process flow: a) Model of Al_2O_3 with trenches above sacrificial mesa, b) sectioned view through the center of model, c) Model of sealed vacuum cavity, d) sectioned view through the center of model, e) Model of superstrate PI5878G, f) sectioned view through the center of model. (Dimensions not to scale)

deposited using a thermal evaporator. Sputtering was done in a pure Ar environment at 10 mT pressure. The first deposition was a 3500 Å layer of Si_3N_4 on a cleaned Si wafer. This layer promotes adhesion to subsequent layers. This was followed by spin casting polyimide PI5878G on to a silicon wafer. A 3500 Å layer of Si_3N_4 is deposited on the polyimide to promote adhesion between the polyimide and subsequent layers. In case of detectors being made on rigid Si substrates, the preceding two steps can be skipped and further depositions can be continued on the initial nitride layer. 4000 Å of Al is then deposited to serve as the reflecting mirror. Sacrificial polyimide PI2610 was then spun onto the Al mirror at 2500 rpm. It was soft baked at 90°C for 90 s followed by hard bake at 150°C for 90 s. The PI2610 coated wafer was then loaded into an oven preheated at 150°C. The oven temperature was gradually increased to 265°C and the polyimide was cured for 5-6 hours. The final polyimide thickness was 2.5 μm. This layer serves as a sacrificial layer. This was followed by 3500 Å of nitride that serves as the support membrane for the detector. Negative photo resist lift off technique was employed to form the subsequent Ti arms and Au bond pads and Au contact pads. Negative photo resist NR7-1500P is spun onto the nitride layer at 2250 rpm. It is soft baked at 150°C for 60s. Photolithography through the 'arms' mask is done and the wafer is hard baked at 100°C for 60 s. It is then developed in a dilute developer solution. The developer RD6 made by Futurex corp. was used and diluted by deionized water in a ratio RD6:DI::50:25 by volume. 1500 Å thick Ti was then sputtered on to the

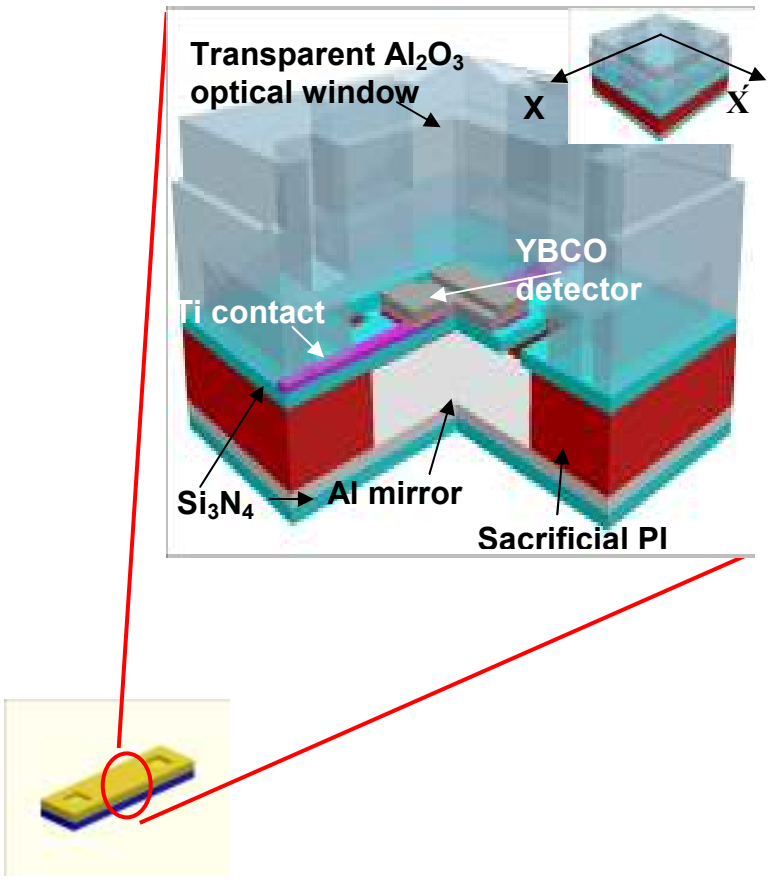

Figure 6.14 Computer generated model of fabricated microcavity (Dimensions not to scale)

wafer followed by 700 Å of Au. Ti is used as the electrical arm because for a conductor it has a low thermal conductivity whereas the Au contacts provide a good ohmic contact between the Ti and the YBCO as well as form the bond pads for subsequent characterization. The wafer was placed in an Acetone bath and ultrasonically agitated to remove the underlying NR7-1500P. This resulted in Ti covered with Au structures. The

Au was then patterned and etched away using positive photo resist. This leaves only the contacts and the bond pads of Au. 3600 Å of YBCO was then deposited, patterned and etched using dilute Al etchant to form the bolometer pixel. This completes the bolometer fabrication and subsequent steps are to create a cavity around it. Trenches were opened in the nitride layer to enable subsequent micromachining of the underlying sacrificial polyimide. Photo definable polyimide PI2737 is spun on at 2500 rpm for 55 s. It is soft baked at 65°C for 3 mins followed by a hard bake at 95°C for 3 mins. The polyimide is then exposed using a 'Large-well' mask and developed in developing solution D9040 followed by rinse in R1918 to remove the developed polyimide PI2737. The height of the PI2737 was measured to be about 2 μm. 1.5 μm of Al_2O_3 was then deposited to form the initial layer of the optical window above the mesa. Trenches were opened in the Al_2O_3 to make micromachining within the cavity possible. Micromachining was done using oxygen plasma ashing. The top mesa made of photo definable PI2737 is etched first, in the process exposing the underlying PI2610 through the trenches in the support Si_3N_4. Both the Al_2O_3 and Si_3N_4 layers are optically transparent and the progress in micromachining could be observed visually under a microscope. The extents of the lateral etch under the Si_3N_4 support layer indicates the extent of the etching under the bolometer pixel. After a satisfactory extent of micromachining has been achieved, further deposition of Al_2O_3 is used to seal the vacuum cavity. This deposition is done at 10mT pressure and this should be the pressure inside the vacuum cavity. PI5878G can be deposited on top of the device and the developed, exposed and etched above the bond pads. PI5878G is photosensitive but

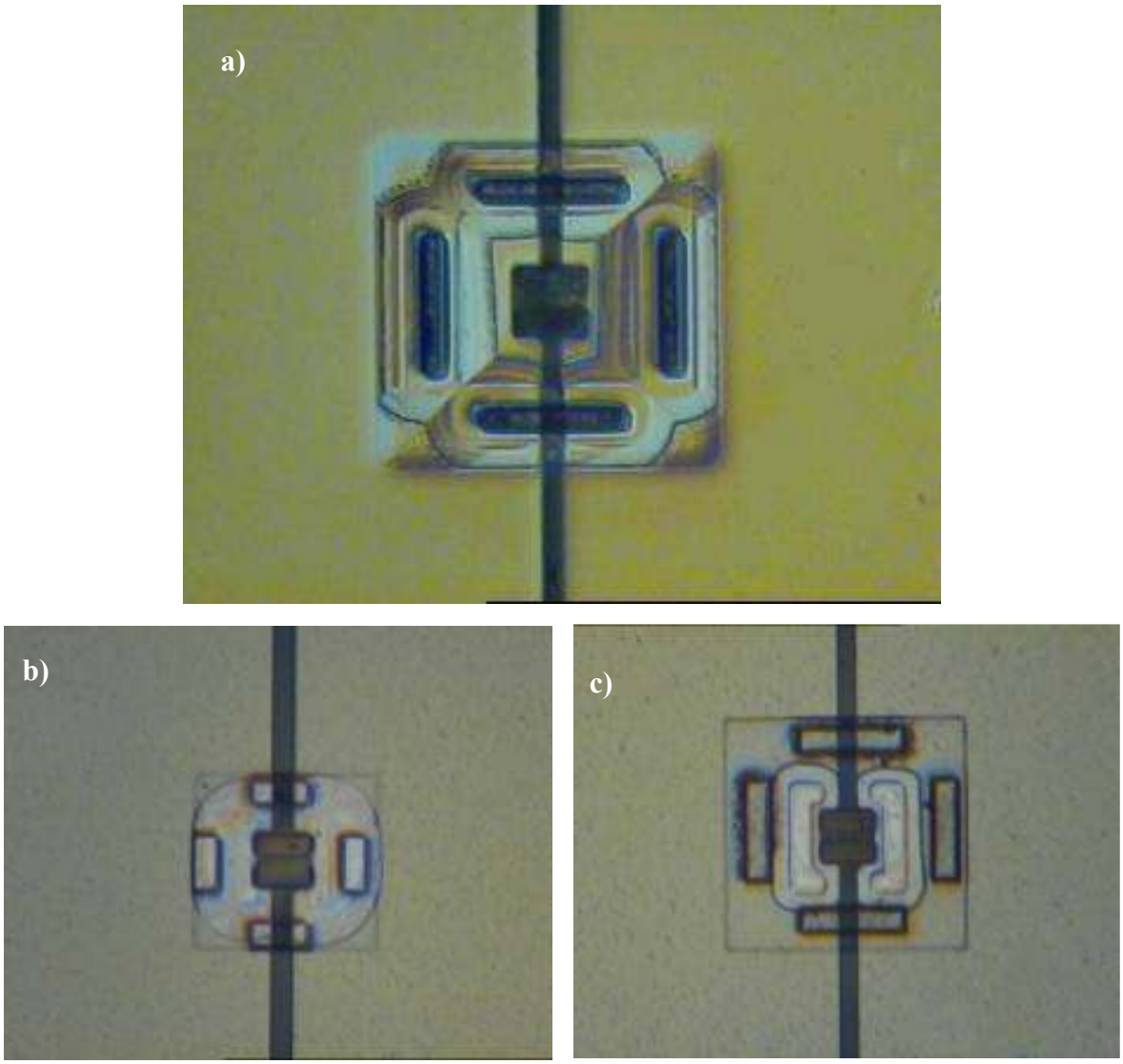

Figure 6.15. Various stages during fabrication under a microscope (a) Partially micromachined microbolometer. The sacrificial PI2737 can be seen receding from the trenches in the Al_2O_3: b) Completely micromachined cavity: c) Completely micromachined and sealed cavity.

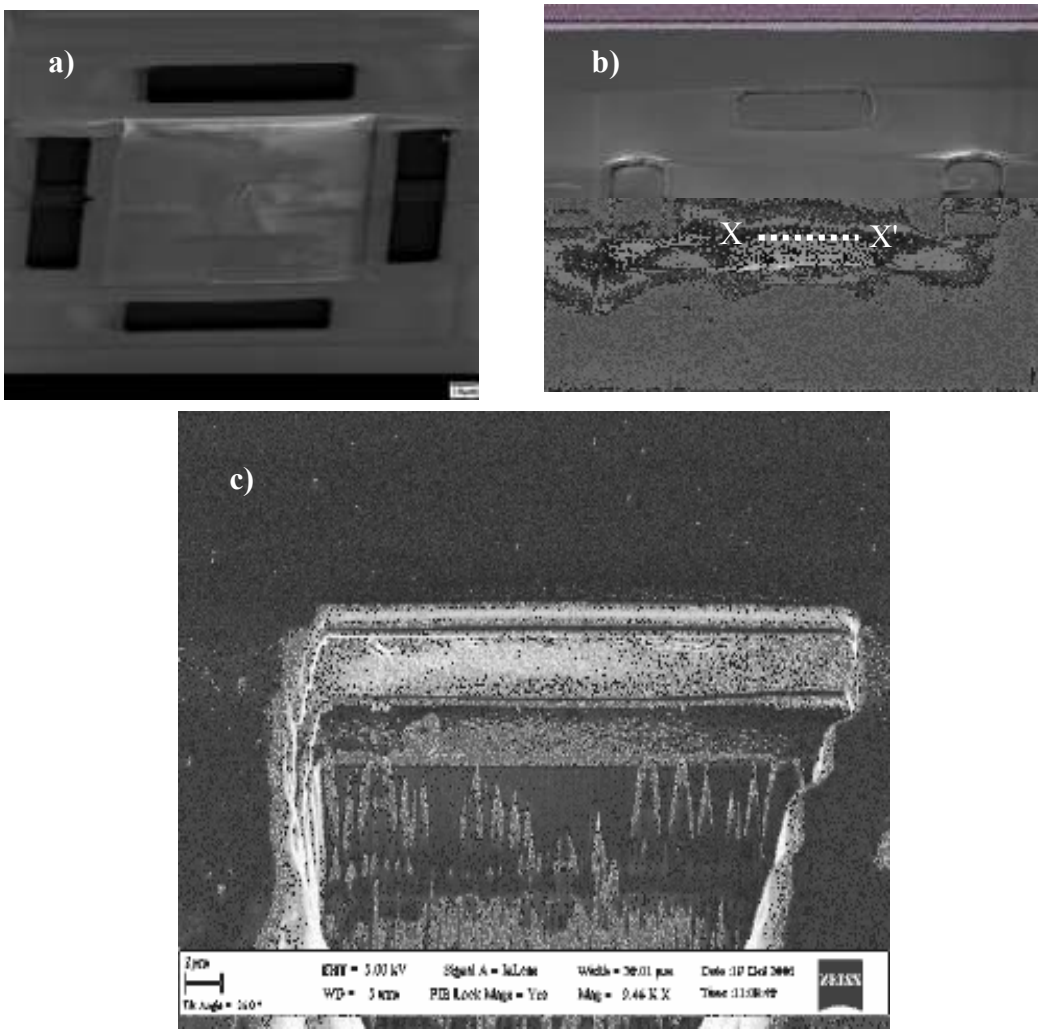

Figure 6.16. SEM graph of various stages of device level vacuum packaging. (a) Micromachined microbolometer prior to sealing: b) SEM graph of sealed microcavity c) Cross sectional view of vacuum cavity at XX´ in b) showing Si_3N_4 support membrane between micromachined spaces.

only if it is not thick. Successful developing has been done for 8μm thick polyimide but development does not work for thicker polyimide layers like 24 μm. The Al_2O_3 is etched away above the bond pads too to expose them. Figure 6.14 shows a cut away of a computer generated model of the vacuum cavity containing a microbolometer on a support nitride membrane. Figure 6.15 and 6.16 show pictures of the device during various stages of fabrication. Figure 6.15(a) shows partially micromachined PI2737 receding through the trenches in the top Al_2O_3. Figure 6.15(b) shows a fully micromachined cavity. The rectangular outline of the PI2737 as well as the round outline of the sacrificial PI2610 can be clearly seen. Figure 6.15(c) shows a sealed fully micromachined cavity. Figure 6.16 (a) shows an SEM graph of a micromachined device prior to encapsulation. Figure 6.16(b) shows an SEM graph of a complete vacuum cavity. Figure 6.16(c) shows the cross section of a vacuum cavity at XX′ in Figure 6.16(b). The support nitride membrane can be seen between micromachined spaces above and below it. The devices are diced and packaged in ceramic packages.

Ultrasonic wire bonding is used to make electrical connections and the devices are tested for electrical and optical properties.

6.6 Device characterization

Due to changes in the device design, the structural analyses was carried out again on the modified geometry. Figure 6.17 shows the bent Al_2O_3 layer only although the analysis was performed on the entire cavity. The other layers have been suppressed

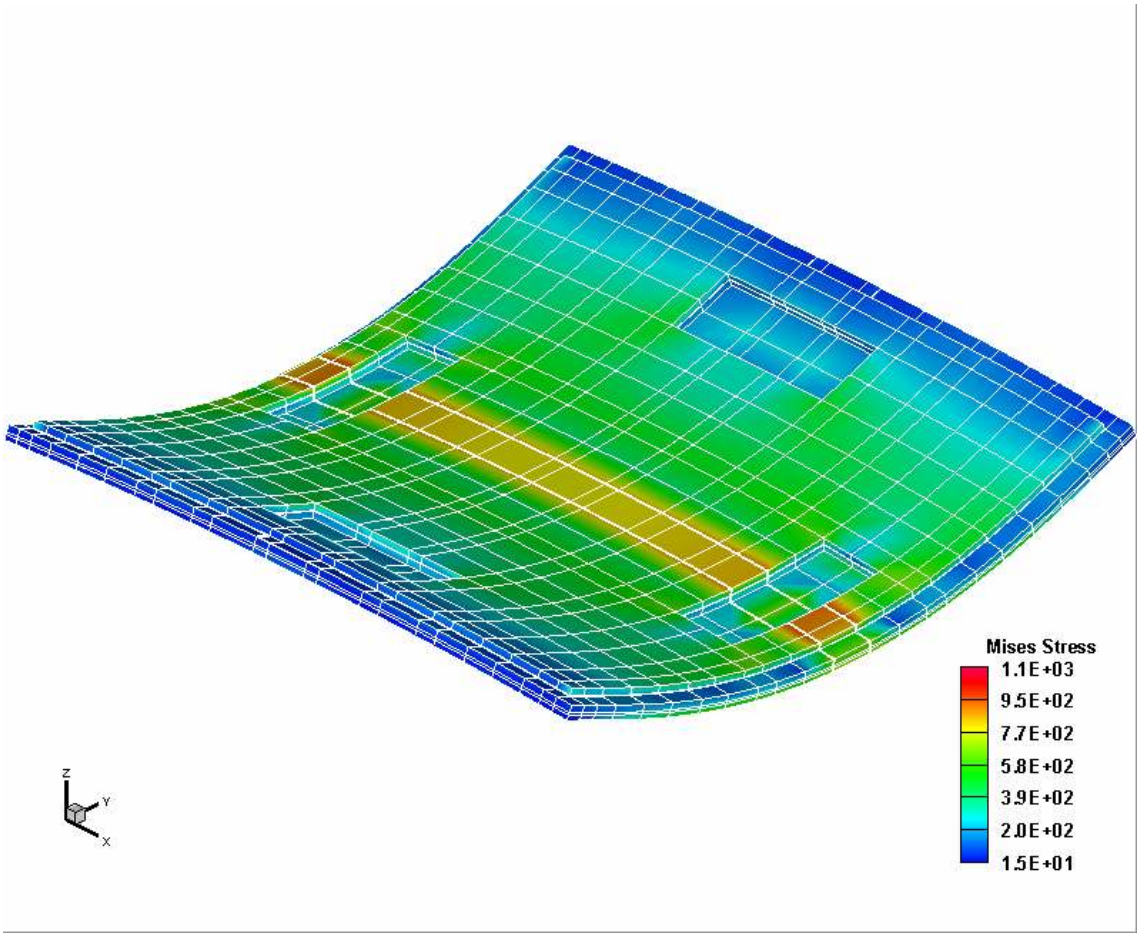

Figure 6.17. CoventorWARE® FEM simulation to calculate stresses produced in an Al_2O_3 optical window. The simulation was performed on an entire cavity but only the optical window is shown here for greater detail.

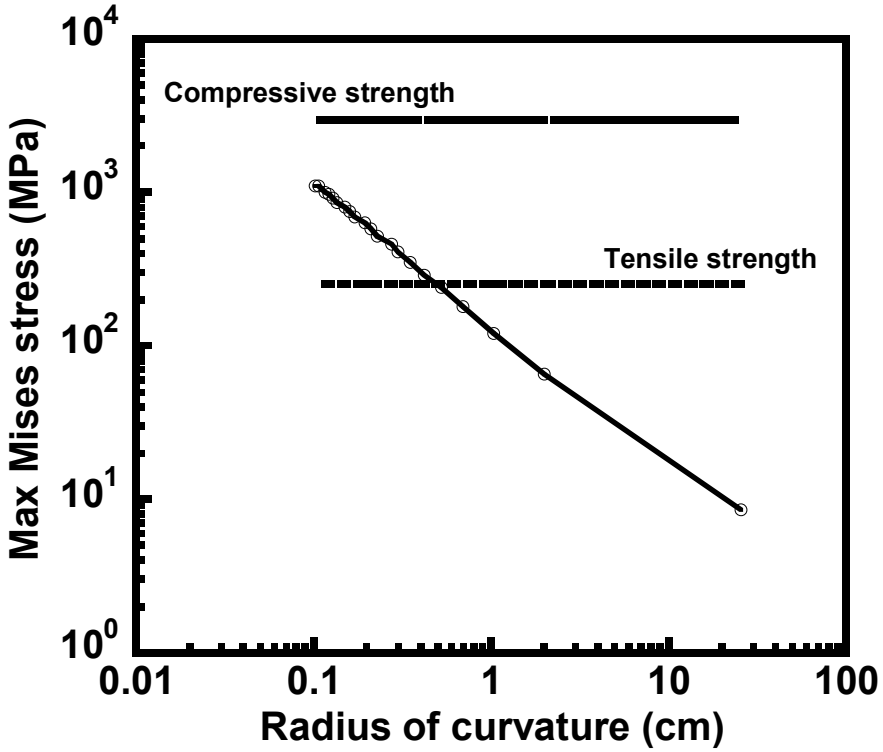

Figure 6.18. Mises stresses produced in the Al_2O_3 optical window of a vacuum cavity model versus the radius of curvature of the cavity. The data has been generated using FEM based CoventorWARE®. The tensile and compressive strengths of ceramic Al_2O_3 are also shown for reference.

for clarity. The detectors were characterized for electrical and optical properties. It was observed that the device resistance increased monotonically with time. Figure 6.18 shows the Mises stress produced as a function of the radius of curvature of the optical window. As in the previous analysis, it can be seen that the stresses are in the linear region up to a radius of ~ 1 cm.

The design resistance of the devices was 170 kΩ. Immediately after fabrication of the detectors, the resistances of devices was measured randomly and found to be in the expected range. Some devices had higher resistance but still remained in the few MΩ range. The device resistances however kept increasing as the sacrificial photo-definable polyimide PI2737 was deposited atop the detector. This continued until in some cases it was not possible to measure the resistance directly with a single Ohmmeter. It is possible that some acidic constituent of the sacrificial photo-definable PI2737 attacked the YBCO, thus reducing the thickness of the detector and increasing the resistance.

6.6.1 Voltage-Current (VI) and Temperature Coefficient of Resistance (TCR)

The DC resistance of the device on flexible substrate (henceforth called DEV-F) was measured to be 86.7 MΩ, while that of the device on rigid substrate (henceforth called DEV-R) was 39.3 MΩ. The device resistance as a function of temperature was also measured employing a probe station with a controllable variable temperature chuck. This was used to compute the temperature coefficient of resistance (TCR) of the bolometers as detailed in chapter 4. DEV-F had a TCR of -3.7 %/K at 300 K while

DEV-R had a TCR of -3.4 %/K at the same temperature. These values are in agreement with the earlier reported values of TCR for YBCO.

Figure 6.19(a) shows the TCR and resistance of DEV-R as a function of temperature. The VI curves of the same device at two different temperatures are also shown in Figure 6.19(b). Figure 6.20(a) shows the TCR and resistance of DEV-F as a function of temperature. The VI curves of the same device at two different temperatures are also shown in Figure 6.20(b).

6.6.2 Thermal conductance G_{th}

The thermal conductance of the device to the substrate was measured using the Joule heating method as detailed in chapter 4, albeit a linear fit was made to the power versus resistance plot using the expression $R(T) = R + P/G_{th}\, dR/dT$. G_{th} was calculated from the slope of the curve as explained by Rice et. al.[80]. An HP4155B semiconductor parameter analyzer was used for this purpose. In view of the high device resistance, the current sweep was kept between ±0.5 μA to minimize excessive heat dissipation in the bolometers. The non linear VI characteristics (Figures 6.19(b) 6.20(b)) show the effect of Joule heating. The devices had thermal conductances of 3.73×10^{-6} W/K (DEV-F) and 1.14×10^{-6} W/K (DEV-R) respectively. These values of G_{th} compare well with the calculated theoretical minimum values for the devices. Contact and spreading thermal resistances as well as the difference between the actual and modeled cavity dimensions are likely reasons for the difference between the calculated and measured values.

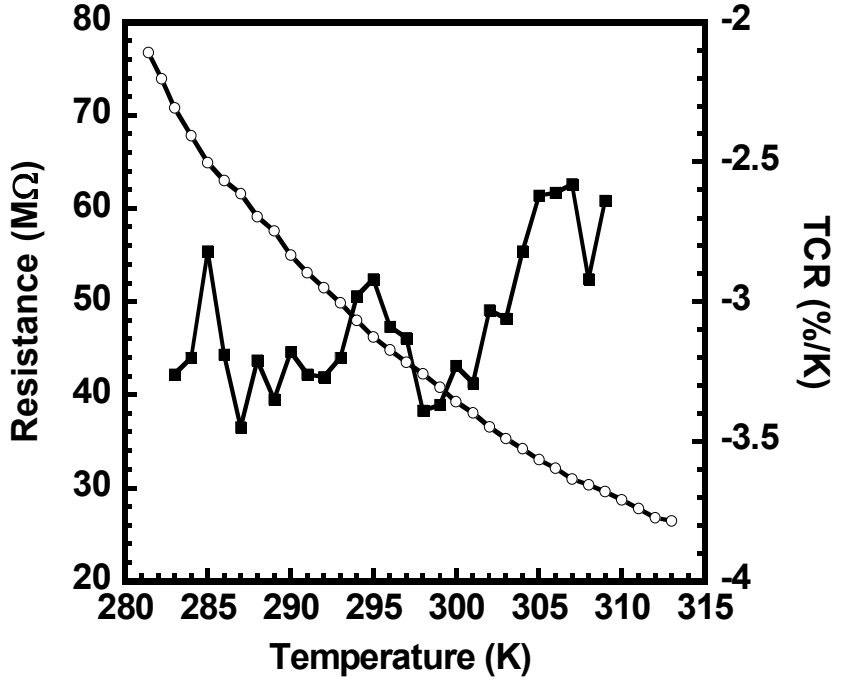

(a)

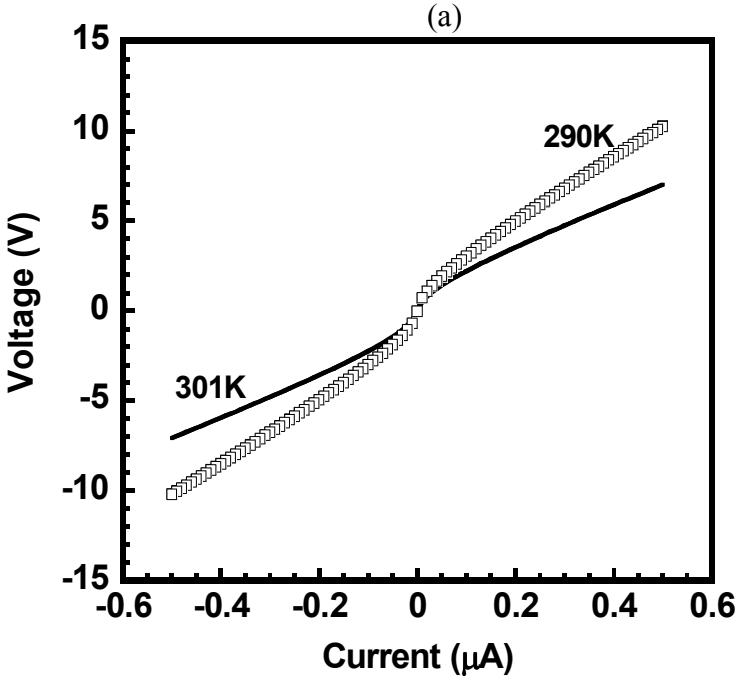

(b)

Figure 6.19. (a) Resistance and TCR vs. temperature of DEV-R. (b) Non linear VI characteristics of the same device at 301K and 290K.

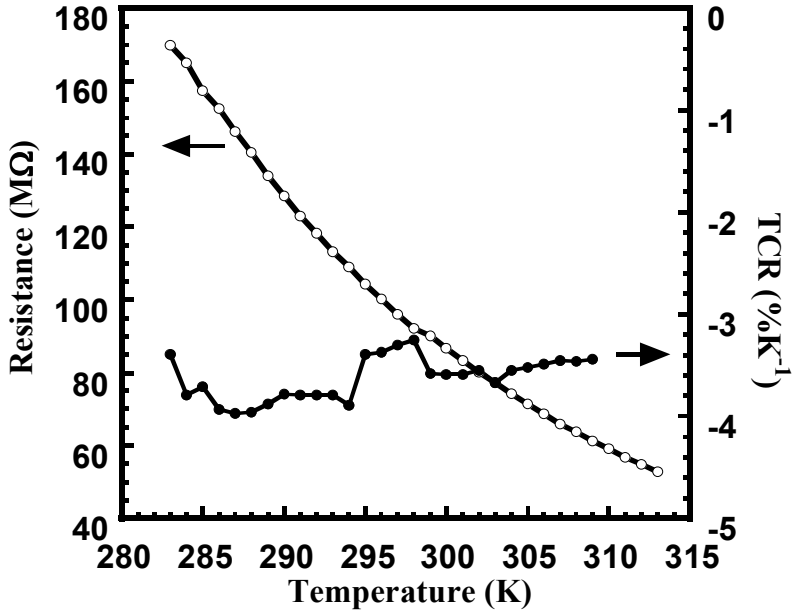

(a)

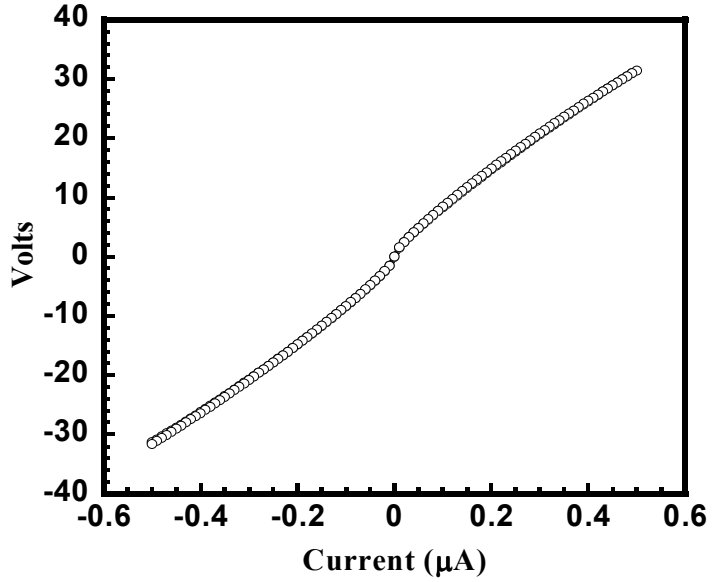

(b)

Figure 6.20 (a) Resistance and TCR vs. temperature of DEV-F. (b) Non linear VI characteristics of the same device at 301K

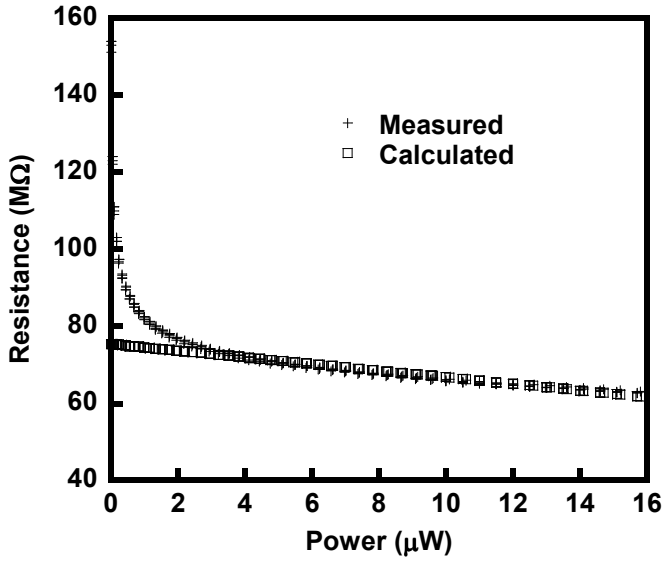

(a)

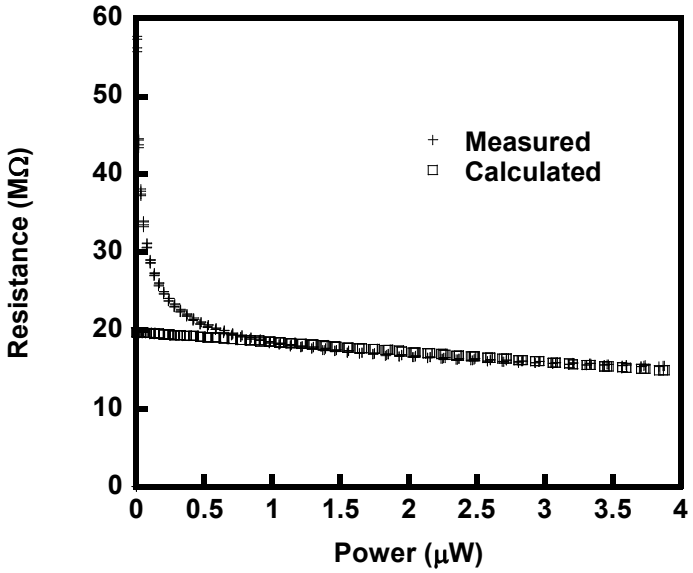

(b)

Figure 6.21. Measured and calculated resistance versus power dissipated of (a) DEV-F (b) DEV-R. The thermal conductance of the devices was calculated from the slope of the curves using the relation $R(T) = R + (P/G_{th})\, dR/dT$

Figure 6.21 shows the measured and computed resistances of the devices plotted against the power dissipated.

6.6.3 Responsivity and Detectivity measurements

The optical characterization was done using a QTH lamp made by Oriel industries. A ZnSe lens was used to focus the infrared radiation onto the detector. Hitherto, bolometer characterization has been done by placing the detector in a vacuum environment e.g. an evacuated cryostat with a ZnSe optical window. With the current device level packaging though, the need for a cryostat was eliminated and these measurements were carried out with the detector package in air. A chopper was used to modulate the optical signal. The devices were measured with a fixed voltage bias across the detectors. Figure 6.22 shows the responsivity and detectivity of DEV-F plotted as a function of chopper frequency. Figure 6.23 shows the responsivity of DEV-F versus the bias voltage at 5 Hz and 80 Hz. Figure 6.24 shows the responsivity and detectivity of DEV-R versus the chopper frequency. At a modulation frequency of 5 Hz, DEV-F had a current responsivity of 61.3 μA/W at a bias voltage, V_b = 10.1 V. At the same frequency, DEV-R had a current responsivity of 50.0 μA/W at a bias voltage, V_b = 1.4 V. Being a function of the power absorbed in the detector, the device responsivity is very sensitive to the dimensions of a terminated resonant structure like the vacuum cavity enclosing the detector. The cavity dimensions can be calculated to ensure maximum power dissipation in the YBCO detector plane. This will improve the absorptivity of infrared energy in the device and also improve the responsivity. The detectivity of the devices was also measured. DEV-F and DEV-R had maximum

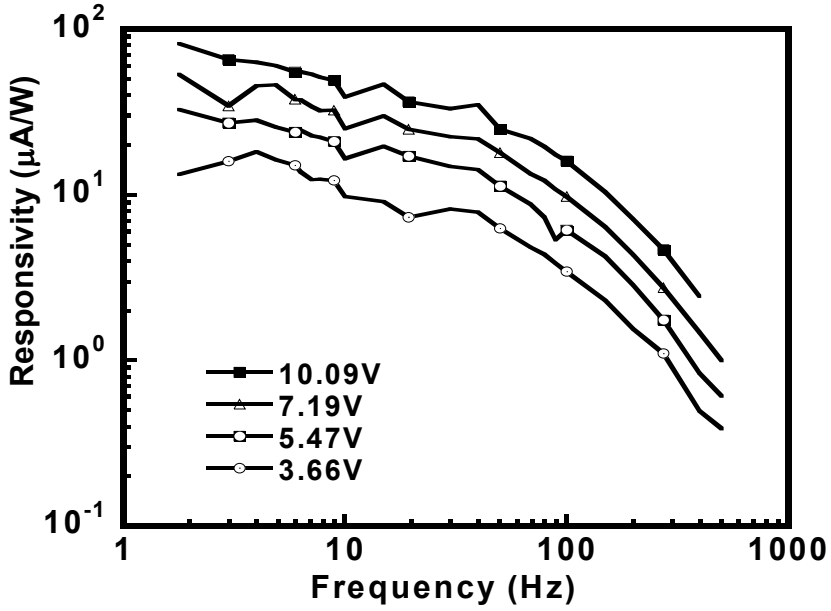

(a)

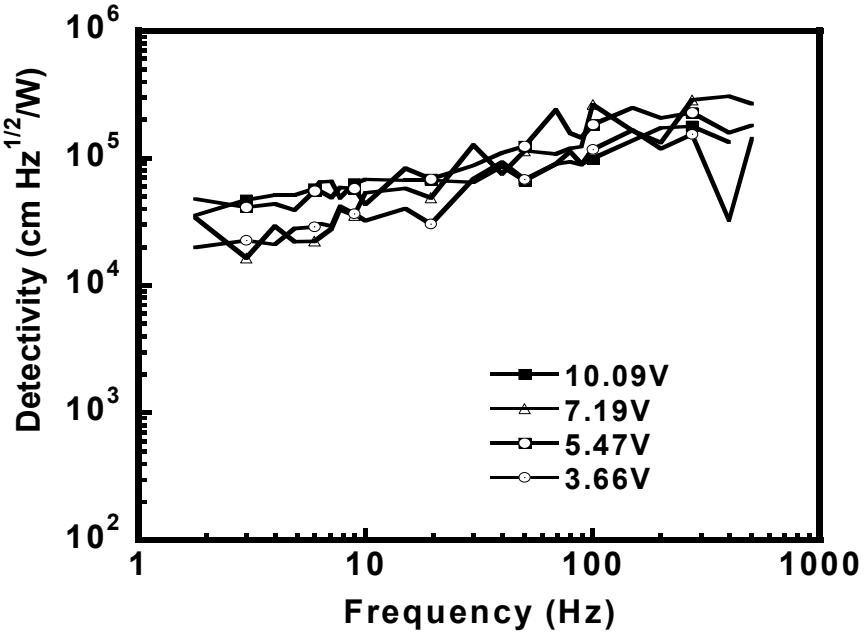

(b)

Figure 6.22. (a) Responsivity and (b) Detectivity versus chopper frequency for DEV-F.

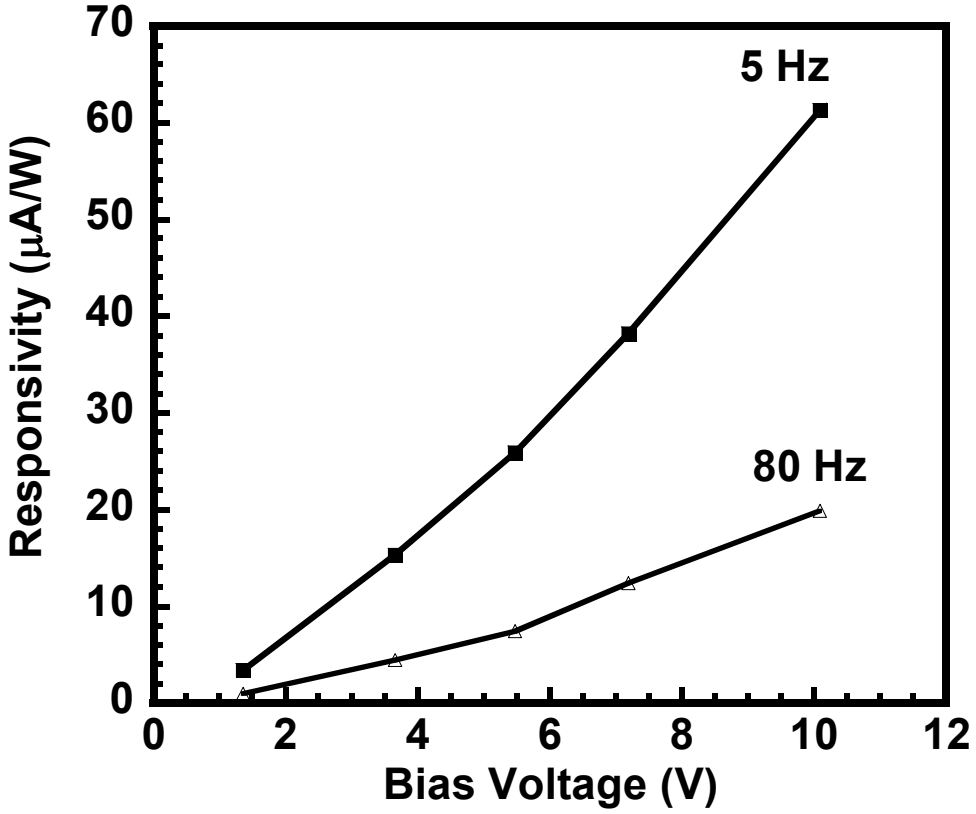

Figure 6.23 Responsivity versus bias voltage of DEV-F at broadband infrared radiation modulated at 5 Hz and 80 Hz.

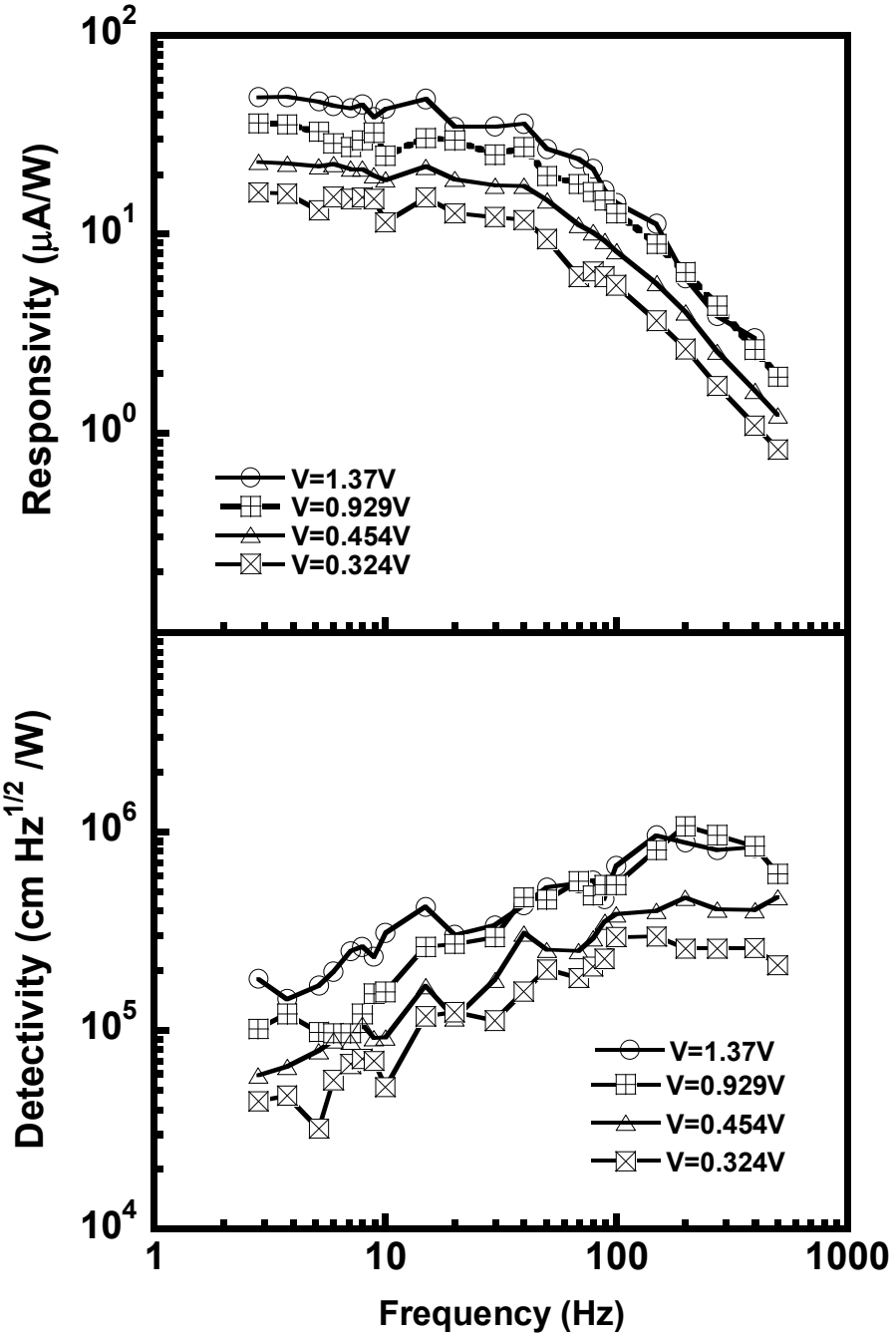

Figure 6.24. Responsivity and Detctivity versus optical modulation frequency of DEV-R.

detectivities of 3.1×10^5 cm-$Hz^{1/2}$/W and 1.1×10^6 cm-$Hz^{1/2}$/W respectively. The low detectivity is due to the low responsivity and high noise in the devices. The sources of the noise need to be investigated and eliminated in future work.

6.6.4 Noise equivalent power

Another important figure of merit is the noise equivalent power (NEP); the input power necessary to give a unity signal to noise ratio. An NEP at 5 Hz of 7.7×10^{-8} W/$Hz^{1/2}$ and 2.7×10^{-8} W/$Hz^{1/2}$ was measured for DEV-F and DEV-R respectively.

6.6.5 Absorptivity, thermal capacity and thermal time constants

The effective time constant of the device was measured from the responsivity data. The signal frequency corresponding to half the maximum responsivity f_{-3dB} was measured and the effective thermal time constant calculated from it as explained in chapter 4. Both the bolometers had $f_{-3dB} \approx 50Hz$ corresponding to effective thermal time constant $\tau_{eff} = 3.2ms$. The corresponding thermal time constants of the two devices were calculated from the expression $\tau_{th} = \tau_{eff}\left\{1 + \alpha\Delta T\left(\frac{R_b - R_s}{R_b + R}\right)\right\}$ [33]. DEV-F and DEV-R had thermal time constants of 3.0ms and 3.3ms respectively. The thermal capacitances of the devices were extracted from $C_{th} = G_{th}\tau_{th}$. The devices had thermal measured thermal capacitances of 1.1×10^{-8} J/K and 3.3×10^{-9} J/K for DEV-F and DEV-R respectively. Using the volume and specific heat capacity of each material on the micromachined bridge, The theoretical thermal capacitance of the devices was

computed to be 2.0×10^{-9} J/K. This is the same for both the devices as the geometry of the devices is the same

The absorptivity was calculated using the measured maximum responsivity and thermal conductance G_{th} as outlined in chapter 4. DEV-F and DEV-R had absorptivities of 4.7 % and 7.7 % respectively. To increase the absorptivity in the detector, the cavity dimensions along the optical axis have to be adjusted very carefully to cause maximum power absorption in the detector plane. Slight variations in the dimensions like layer thicknesses or inter layer spacing can change absorptivity significantly.

Table 6.4 presents a comparison of the measured parameters of DEV-F and DEV-R.

6.7 Conclusions

A new device-level vacuum-packaging scheme has been introduces in this chapter. A preliminary design was subjected to FEM analysis to validate the structural integrity of the vacuum element. The stresses produced in the optical window forming the cavity were found to be less than the fracture strength of the ceramic material used even when the substrate is bent to a radius of 10 mm. Optical masks were fabricated based on this design to fabricate the devices. During fabrication, modifications to the initial design had to be made changing the geometry originally envisaged. The modified geometry was also subjected to FEM based structural analysis and found to be satisfactory. The complex relative permittivity of ceramic Al_2O_3 was extracted using

Table 6.4 Summary of results

Name of device	DEV-F	DEV-R
Substrate	PI 5878G	Si
TCR (%/K) at 300K	-3.7	-3.4
R_0 (Ω)	902	2020
Activation energy E_a (eV)	0.30	0.26
G_{th} (measured) (W/K)	3.7×10^{-6}	1.1×10^{-6}
R_b (MΩ)	86.7	39.3
$\Re_I$ @ 5 Hz (μA/W)	61.3 V_b=10.1V	50.0 V_b=1.5V
Maximum $\Re_I$ (μA/W)	83.2 @ 2Hz, V_b=10.1V	50.0 @ 5Hz, V_b=1.5V
D* @ 5 Hz (cm $Hz^{1/2}$/W)	5.2×10^4 V_b=10.1V	1.5×10^5 V_b=1.5V
Maximum D* (cm $Hz^{1/2}$/W)	3.1×10^5 @ 398Hz, V_b=7.2V	1.1×10^6 @ 200Hz, V_b=0.9V
NEP @ 5Hz (W/$Hz^{1/2}$)	7.7×10^{-8}	2.7×10^{-8}
C_{th} (measured) (J/K)	1.1×10^{-8}	3.3×10^{-9}
τ_{th} (ms)	3.0	3.3
η (%)	4.7	7.7

infrared variable angle spectroscopy for wavelengths from 1 μm to 39 μm. Optical transmission properties of PI5878G were also measured. The thermal conductance from the device to the ambient was calculated using an equivalent circuit and also numerically using finite element method. Devices were fabricated, packaged and characterized. Table 6.4 presents a summary of results.

CHAPTER 7

TUNABLE INFRARED MICROSPECTROMETER

7.1 Introduction

A spectrometer is an optical instrument used to measure the properties of light over a certain portion of the electromagnetic spectrum. Generally the intensity of light is measured but other properties like the polarization can also be measured as a function of frequency or wavelength. The infrared spectrometer will measure the properties of light in the infrared region of the electromagnetic spectrum ranging from 700 nm to ~ 1 mm.

In the present work, a Fabry Perot cavity making use of the interference of light passing through it is employed as a spectrometer. Interferometry is the applied science of combining two or more waves. Based on the phase and amplitude of the interfering waves, constructive or destructive interference occurs. This can be used to make an optical filter.

A Fabry-Perot cavity consists of two parallel reflecting surfaces as shown in Figure 7.1. The absence of the side walls has the effect of reducing the conductor losses and also the number of possible resonant modes[81]. In order for the device to be useful, the plates must be large and highly planar. This serves to reduce the leakage of energy

from the sides due to edge diffraction. Moreover, in case a Fabry Perot cavity is being used as an optical filter based on its transmission properties, the reflecting surface must

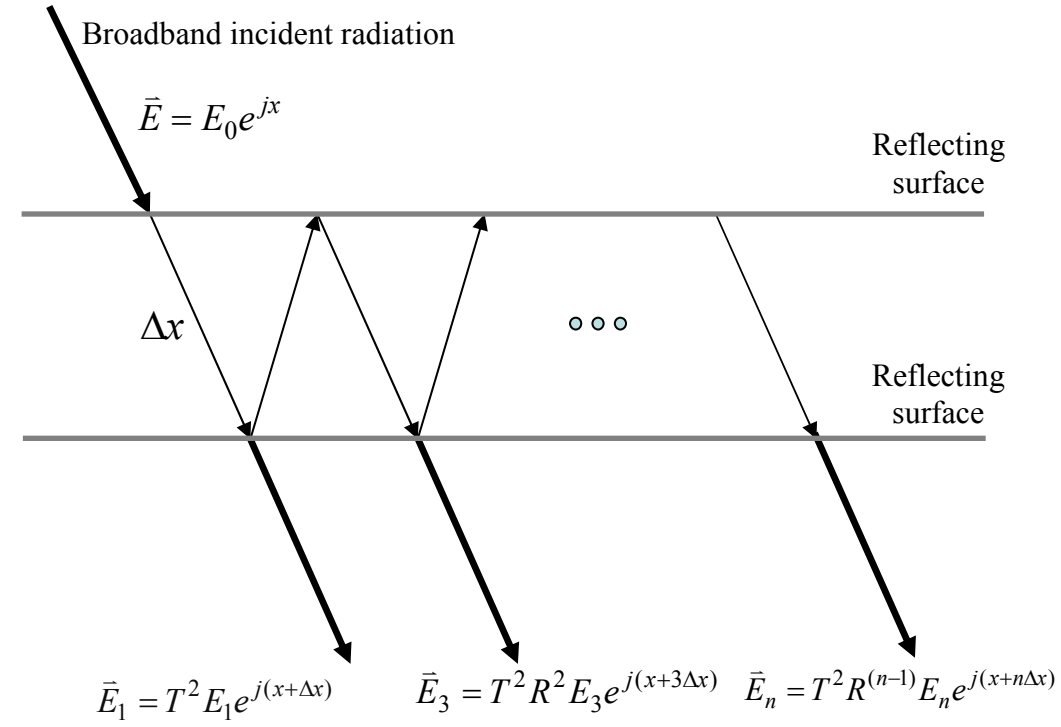

Figure 7.1 A model of transmission through a a Fabry Perot cavity.

be only partially reflective and partially transparent to allow electromagnetic energy through. $R = \frac{\eta_2 - \eta_1}{\eta_2 + \eta_1}$ is the reflection coefficient at the interface between two media with characteristic impedances η_1 and η_2 respectively. In an ideal lossless system,

$T = 1 + R = \frac{2\eta_2}{\eta_2 + \eta_1}$ is the transmission coefficient at the interface[82]. The transmission and reflection cofficients are associated with the electric and magnetic fields. The distribution of power between the transmitted and reflected components is governed by the Fresnel equations. The reflectance (reflected power per surface), is given as $r = \left(\frac{\eta_2 - \eta_1}{\eta_2 + \eta_1}\right)^2$, while the transmittance (transmitted power per surface), is given as $t = 1 - r = \frac{4\eta_1\eta_2}{(\eta_1 + \eta_2)^2}$[29].

From Figure 7.1, depending upon the separation between the reflecting surfaces Δx, the transmitted energy will interfere constructively or destructively at different wavelengths. For maximum constructive interference

$$\Delta x = (2n+1)\frac{\lambda}{2}$$

whereas for maximum destructive interference

$$\Delta x = (n+1)\lambda$$

where $n = 0,1,2,3...$ and λ is the wavelength.

7.2 Practical Fabry Perot cavity based tunable microspectrometer

Such a device has been implemented using standard MEMS deposition and etch techniques. The cross section of such a practical cavity is shown in Figure 7.2. The Fabry Perot cavity is made of thin Al layers deposited by thermal evaporation and

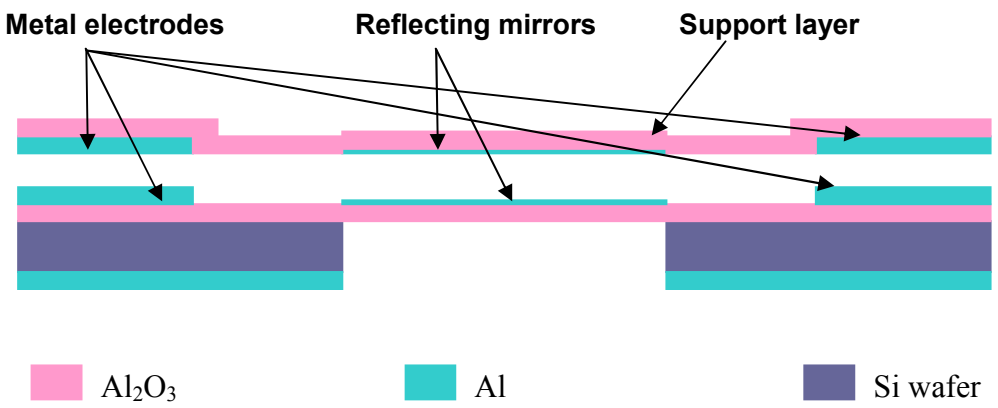

Figure 7.2 Cross section of a model Fabry Perot cavity based microspectrometer (Dimensions not to scale).

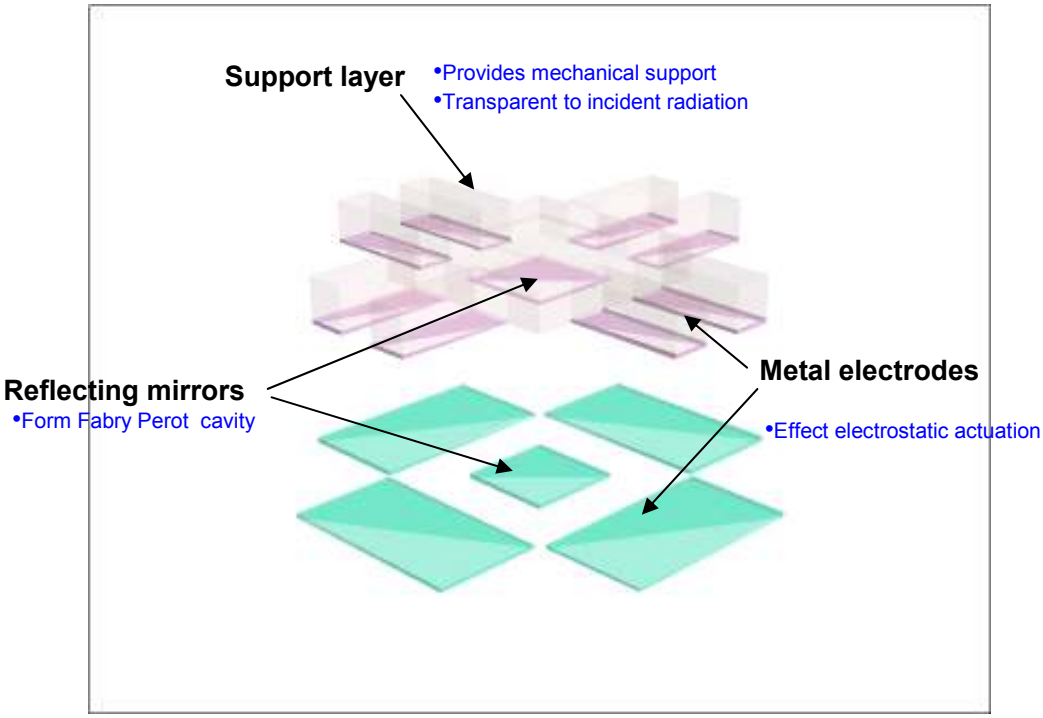

Figure 7.3 A computer generated model of a Fabry Perot cavity based microspectrometer.

patterned using standard photolithography and wet etch techniques. The finesse of the cavity defined as $F = \frac{\pi r^{1/2}}{1-r}$ [83] was used to determine the thickness of the reflecting surface, as well as the transmission of light through the cavity. Finesse is a kind of a measure of the selectivity of the filter. Higher finesse means higher selectivity and a sharper transmission peak. A sacrificial layer like polyimide or photoresist can be used to create the cavity at a particular size like 1-2μm. Metal electrodes made of Al can be used to electrostatically change the reflector spacing. This will make the spectrometer tunable. A support layer is required to hold moveable reflecting surface. The support layer is to be made of rf sputterd Al_2O_3. As discussed in chapter 6, Al_2O_3 has good transmission properties in the near and mid infrared region. Figure 7.3 shows a computer generated model of a Fabry Perot cavity based spectrometer. Deep reactive ion etch is to be used to etch through the Si carrier wafer from the back. The use of an Al hard mask is envisaged for this purpose. The Al mask also serves as an optical shield to prevent infrared radiation from illuminating the detector directly.

Various issues addressed in this process include the power incident on the spectrometer, the mechanical behavior of the structure including the electrostatic control of the inter reflector spacing and the flatness profile of the moveable reflector surface during deflection. The thickness of the reflector mirror was also calculated.

7.3 Infrared power transmission through an aperture

The power that can be received through an aperture determines the minimum possible size of the aperture to be employed in the design of the spectrometer. For a blackbody source

$$M(\lambda,T)=\int_{\lambda_1}^{\lambda_2}\frac{2\pi hc^2}{\lambda^5(e^{\frac{hc}{\lambda kT}}-1)}d\lambda \qquad \frac{W}{cm^2-\mu m} \tag{7.1}$$

Where L is the total spectral exitance between λ_1 and λ_2, h is Planck's constant, k is Boltzmann's constant, c is the speed of light, and T is the temperature in K[29]. Figure 7.4 shows the set up used for calculations. A ZnSe lens with a focal length of 6.6 cm, placed 20 cm away from a mock blackbody source at 900°C used to focus the infrared energy on to the image plain 9.9 cm away. The blackbody source aperture is 2.5 cm in diameter and the lens has a diameter of 3.81 cm. Assuming a lossless lens, the power density on the image plain and consequently the power through different apertures can be calculated and is listed in Table 7.1. Table 7.1 shows the power through apertures of different sizes at a bandwidth of 1 μm in different parts of the infrared electromagnetic spectrum. An Oriel 70124 pyroelectric detector with a broadband responsivity of 1000 V/W is to be used and the power through the aperture gives and indicator of the signal output from it.

A model of a Fabry-Perot cavity based microspectrometer was created using ConventorWARE®. Structural analysis was used to investigate the stresses produced in

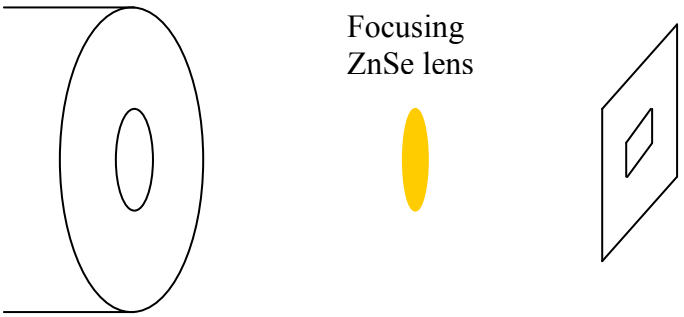

Figure 7.4 Set up for calculating the infrared power through a rectangular aperture in the image plane.

TABLE 7.1 SPECTRAL INFRARED POWER THROUGH A SQUARE APERTURE

Aperture area (μm^2)	Initial wavelength λ_1 (μm)	Final wavelength λ_2 (μm)	Power (μW)
100x100	2	3	10.46
150x150			23.54
200x200			41.85
250x250			65.39
100x100	3	4	8.32
150x150			18.72
200x200			33.28
250x250			52.00
100x100	4	5	5.389
150x150			12.13
200x200			21.56
250x250			33.68

the support structure and the deflection as a result of the applied voltage to the electrodes. The flatness profile of the deflected membrane was also investigated.

7.4 Mechanical analysis of the tunable Fabry Perot cavity

Initially, a geometry consisting of four (two pairs) of support arms/tethers was used. A small pressure was applied to the top surface to see the effect of the tether length on the diaphragm displacement. It was seen that for the same applied pressure of 0.005 MPa, the maximum displacement of the Al_2O_3 shuttle plate was 0.35, 0.65, 1.0 and 1.4μm corresponding to tether lengths of 30, 60, 90, 120 μm respectively. The stresses produced in the support Al_2O_3 increased monotonically but stayed in the linear region. Figure 7.5. shows the result of different simulations. Inter tether spacing did not have a significant effect on the diaphragm displacement. As expected, greater tether lengths produced greater deflection which in turn produced greater stresses in the support layer. Similar analysis with varying inter-tether spacing showed that the membrane deflection was not affected by it.

The effect of the bottom electrode size and position was also investigated using simulations. CoventorWARE® electromechanical solver was used for this purpose. A fixed voltage of 35 V was applied across the actuation electrodes while the size of the bottom electrode was changed to widths of 28, 56, 84, 112 and 140 μm. The top layer displacement varied from 0.032 to 0.97 μm. It was also seen that when the electrodes were kept closer to the fixed end of the tethers, the displacement was less for the smaller electrodes as compared to the fixed electrode being closer to the reflecting

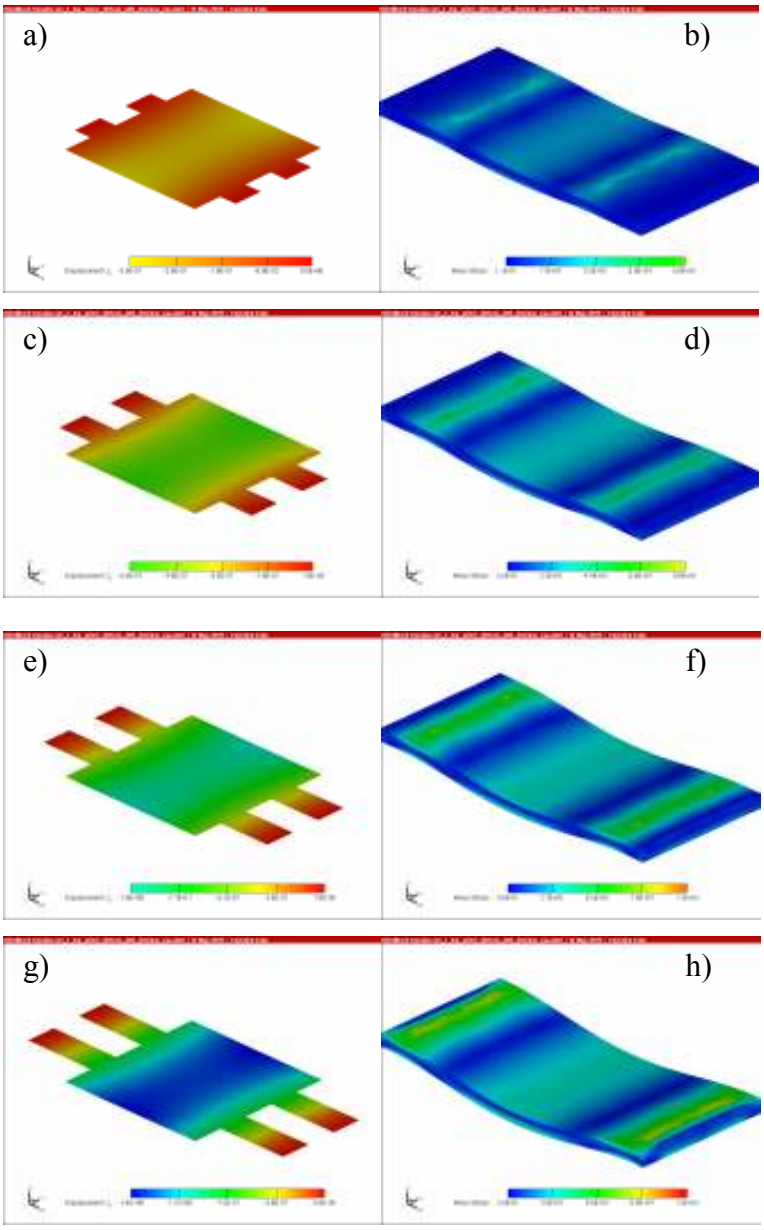

Figure 7.5 Effect of a 0.005MPa load on the top surface of a Fabry Perot cavity with different tether lengths. Deflecting membrane is 250x250μm^2 (a) Displacement in a device with tether length = 30μm, (b) Corresponding Mises stress produced in the support structure (c) Displacement in a device with tether length = 60μm, (d) Corresponding Mises stress produced in the support structure, (e) Displacement in a device with tether length = 90μm, (f) Corresponding Mises stress produced in the support structure (g) Displacement in a device with tether length = 120μm, (h) Corresponding Mises stress produced in the support structure (z dimensions exaggerated for greater detail).

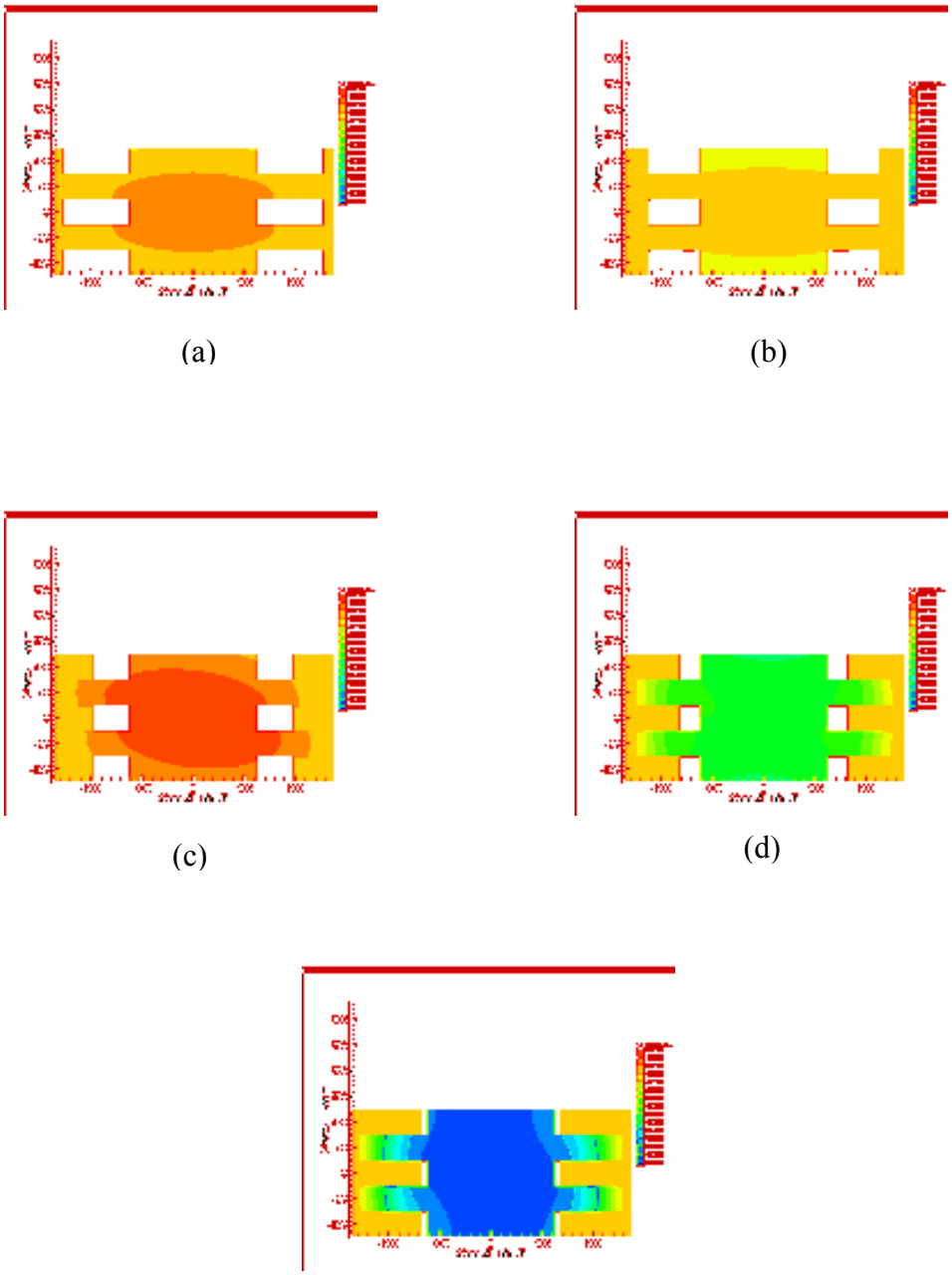

Figure 7.6 Effect of fixed electrode position and size on displacement. Notice relative displacement on the moveable surface (a)28 µm (b)56µm (c)84µm (d)112µm (e)140µm fixed electrode. (V_app = 35V).

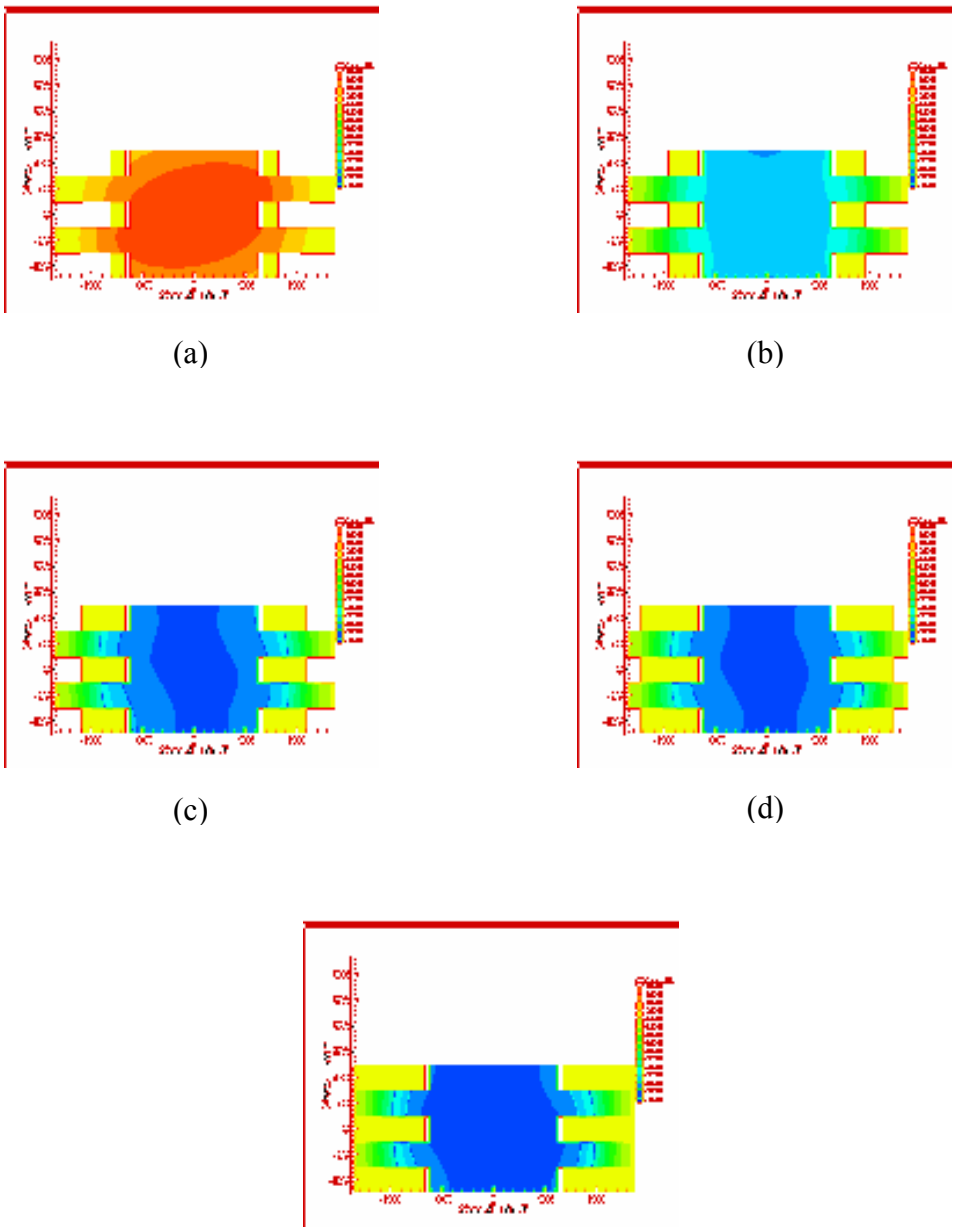

Figure 7.7 Effect of fixed electrode position and size on displacement. Notice relative displacement on the moveable surface (a)28 μm (b)56μm (c)84μm (d)112μm (e)140μm fixed electrode. (V_app = 35V).

mirror. Figure 7.6 and Figure 7.7 show these results. However, the apparent warping of the membrane during deflection was a cause for concern. This meant that the deflecting membrane was not flat during deflection and would have had a detrimental effect on the optical performance of the Fabry Perot cavity which assumes a perfectly flat pair of reflecting surfaces. It was seen that the flatness of the membrane and the top reflecting mirror improved by the introduction of eight (four pairs of) support tethers. This introduced symmetry to the structure and it was seen that the displacement of the top membrane became circularly symmetric. Figure 7.8 shows the displacement of the support diaphragm for a fixed applied voltage of 35 V for different bottom electrode widths with evident symmetry.

Based on these preliminary analyses, a model of a Fabry-Perot cavity based microspectrometer was created using ConventorWARE®. A variant with a partially corrugated support structure of Al_2O_3 was also created to study the effect of the corrugation on the deflection of the top reflector as well as the degree of flatness of the top reflector during deflection (Figure 7.9). To achieve a flat top reflecting surface during deflection, a design consisting of a moveable shuttle mass or diaphragm made of Al_2O_3 holding the top Al reflector supported by tethers on all four sides (as shown in Figure 7.3) was used. The tethers were 150 μm long and 50 μm wide. The tethers were spaced 50 μm apart. The support diaphragm was 250x250 μm^2. The thickness of the support kept 1 μm. The Al mirror was 120x120 μm^2 wide and negligibly (40 Å) thick. The Al electrodes were 4000 Å thick. The electrodes on the support diaphragm had the same lateral dimensions as the tethers. The fixed electrodes were kept 150x250 μm^2

wide. The inter reflector distance was kept 2.5 μm. A parametric electromecahnical analysis was done in which the voltage applied to the electrode was increased from 0V in increments of 10 V. Figure 7.10 shows the same model with the Al_2O_3 support layer suppressed in the figure to show the reflectors and the actuating electrodes. Figure 7.11 shows the deflection of the top reflector as a function of the applied voltage. Despite some difference in the two geometries used for the simulation, the maximum deflection of the top reflector is ~1.5 μm in both cases at a pull down voltage of ~130 V. This deflection will however not be entirely usable as the stresses produced in the support Al_2O_3 layer exceed the tensile strength of the material (260 MPa) at an applied voltage of ~ 100 V (Figure 7.12). The corresponding displacement of the top reflector is ~0.7 μm. This corresponds to the inter reflector spacing ranging from 1.8-2.5 μm. The spectrometer thus offers a theoretical tunability of 3.6-5.0 μm.

Figure 7.13 shows the flatness profile of the top reflector during different stages of its deflection. Results for both geometries are shown for comparison. It can be seen that using a corrugated support membrane contributes to better flatness of the top reflector albeit at the expense of deflection. The advantage in flatness however diminishes at lower deflections.

7.5 Transmission line model of the cavity

The actual Fabry Perot cavity is more complex than the theoretical model because of the greater number of layers involved. A transmission line model employing ABCD transmission matrices[81] was used to find the transmission of infrared energy through the device. Figure 7.10 shows the model of the transmission line. For a multi

section transmission line as in Figure 7.7, the product of the individual ABCD matrix of each segment is used to relate the input and output voltages.

$$ABCD = \begin{bmatrix} \cos\beta l & Z_0 \sin\beta l \\ \dfrac{1}{Z_0 \sin\beta l} & \cos\beta l \end{bmatrix}$$

where $Z_0 = \sqrt{\frac{\mu_0}{\varepsilon_0}}\sqrt{\frac{\mu_r}{\varepsilon_r}}$ is the characteristic impedance of the material, $\beta = \frac{2\pi}{\lambda}\sqrt{\mu_r \varepsilon_r}$ is the phase constant of the medium and l is the length of the of the transmission line. A value of $\mu_r = 1$ was used in the analysis while the extracted complex relative permittivity ε_r of Al_2O_3 were used. The complex relative permittivity of Al was used from[84] for the analysis. Figure 7.15 shows the normalized transmission through the cavity for inter reflector spacing of 2 μm, 2.5 μm and 3 μm. As expected transmission is seen at 4 μm, 5μm and 6 μm respectively. The Al_2O_3 thickness was kept at 1.5 μm while the Al reflector was kept at 40 Å.

Using an FEM based field solver (Ansoft HFSS), the transmission through the Fabry Perot cavity was also attempted to be modeled. This was done primarily to investigate the edge diffraction effects of the reflector and the support layer, and secondarily the effect of the curvature in these layers due to deflection, on the resonance of the cavity. This attempt did not meet with success as HFSS a geometry modeling such minute curvature could not be created in HFSS and rational results could not be obtained for a cavity made of flat components for different reflector spacing. Moreover,

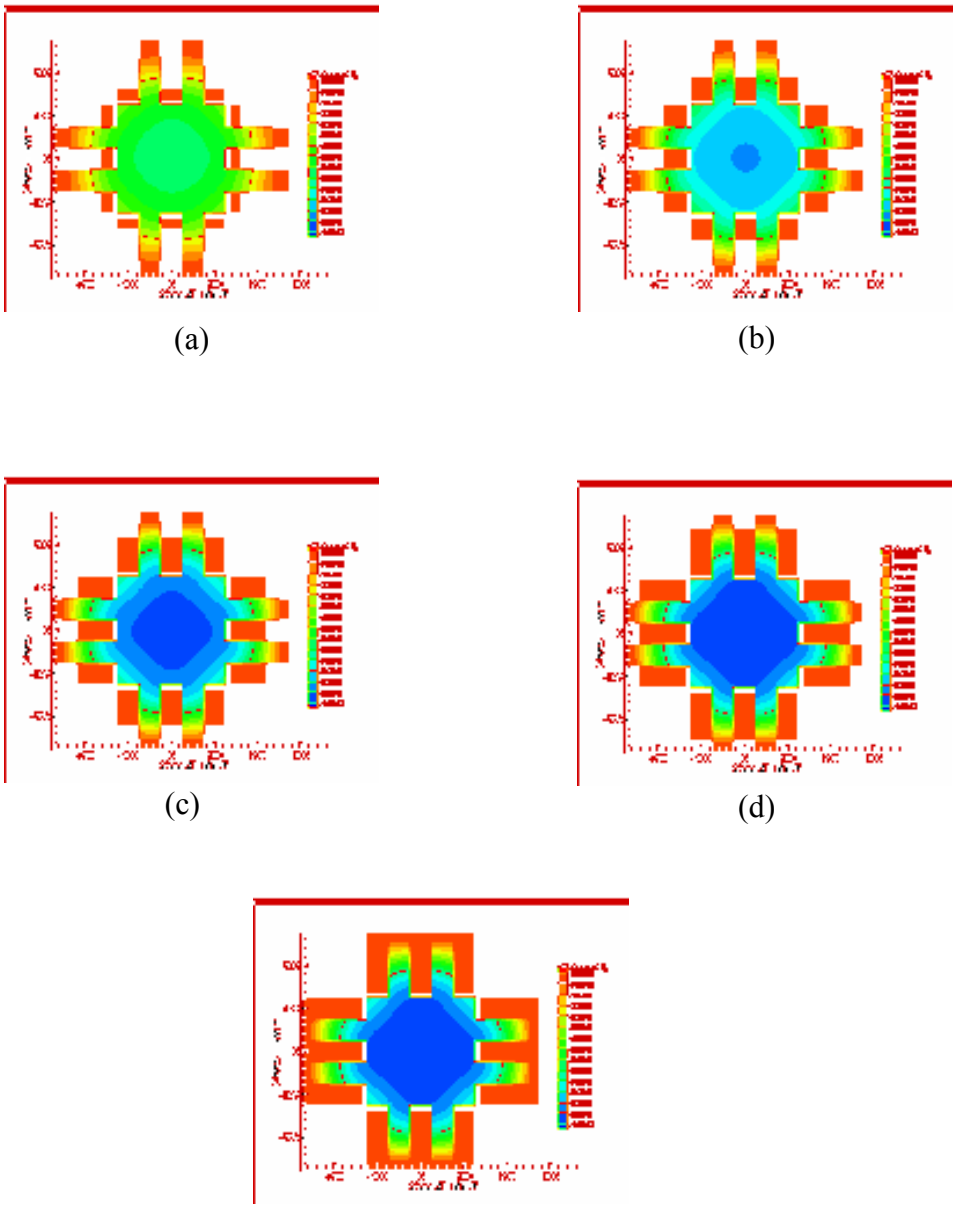

Figure 7.8 Electrode position and displacement for 8 tether geometry. Notice circularly symmetric relative displacement on the moveable surface (a)28 μm (b)56μm (c)84μm (d)112μm (e)140μm fixed electrode. (V_app = 35V).

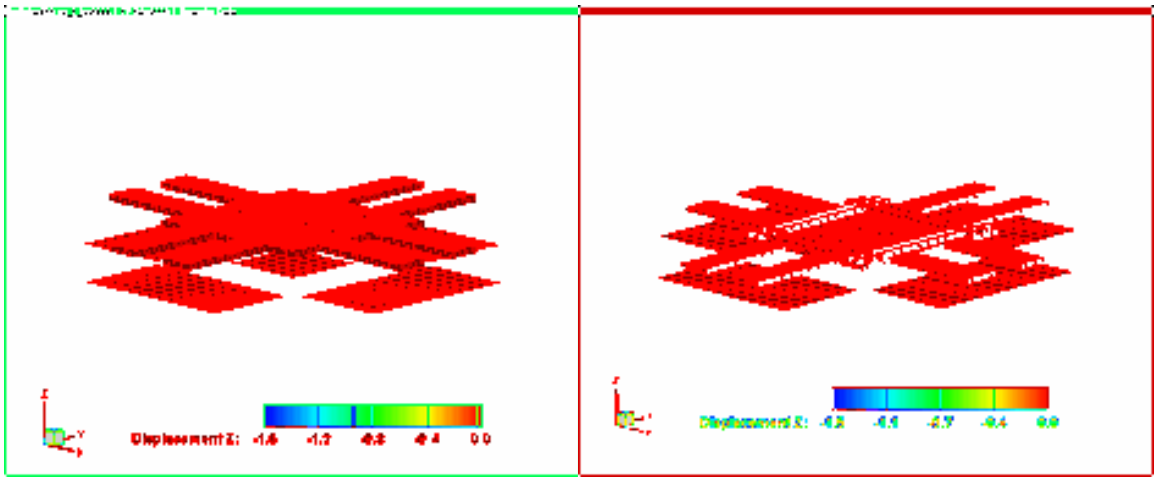

(a) (b)

Figure 7.9 CoventorWARE® generated models of the Fabry Perot cavity based spectrometer for finite element analyses. (a) A device with a plane Al_2O_3 support layer and (b) A device with a partially corrugated Al_2O_3 support layer. (z dimension magnified to show greater detail).

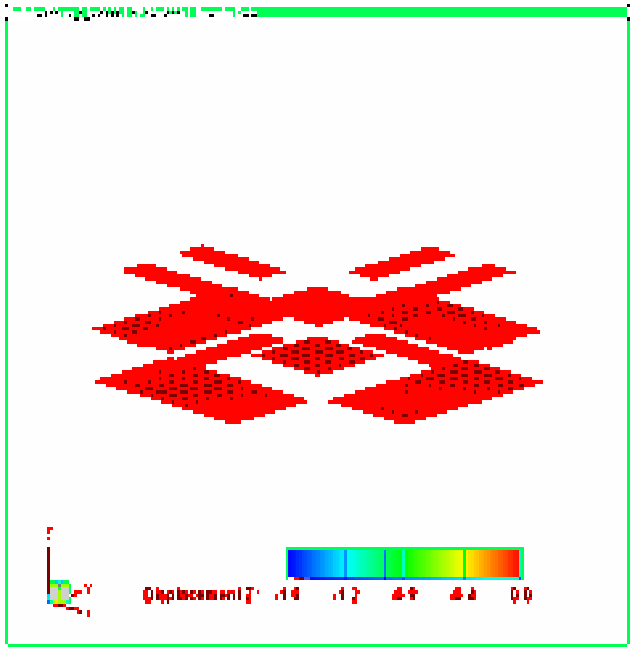

Figure 7.10 CoventorWARE® generated model of the Fabry Perot cavity based spectrometer for finite element analyses. The Al_2O_3 support layer ahs been suppressed in the figure to show the reflectors and the actuating electrodes (z dimension magnified to show greater detail).

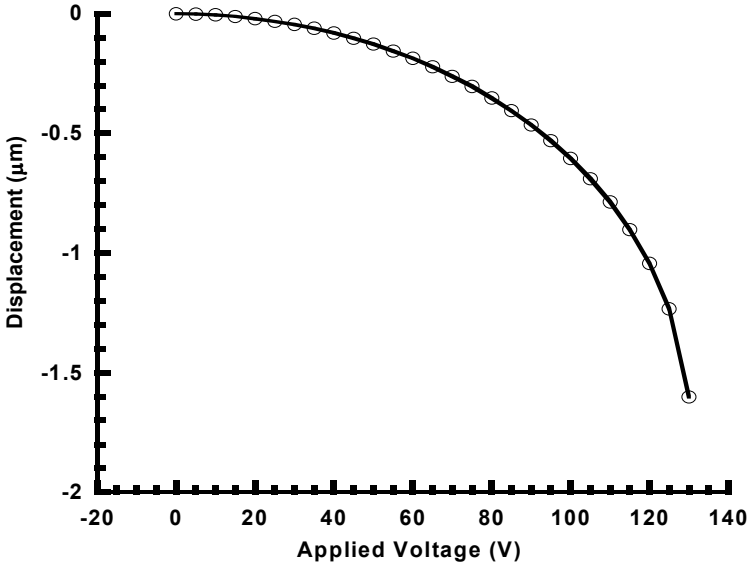

(a)

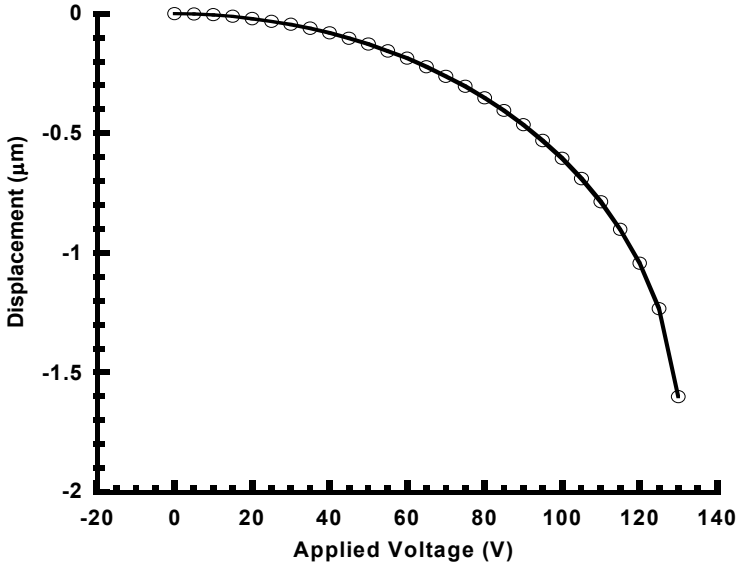

(b)

Figure 7.11 FEM analysis results of simulations carried out on devices shown in Figure 7.9(a) and (b). Top reflector displacement as a function of voltage applied to the actuator electrodes. (a) A device with a plane Al_2O_3 support layer and (b) A device with a partially corrugated Al_2O_3 support layer.

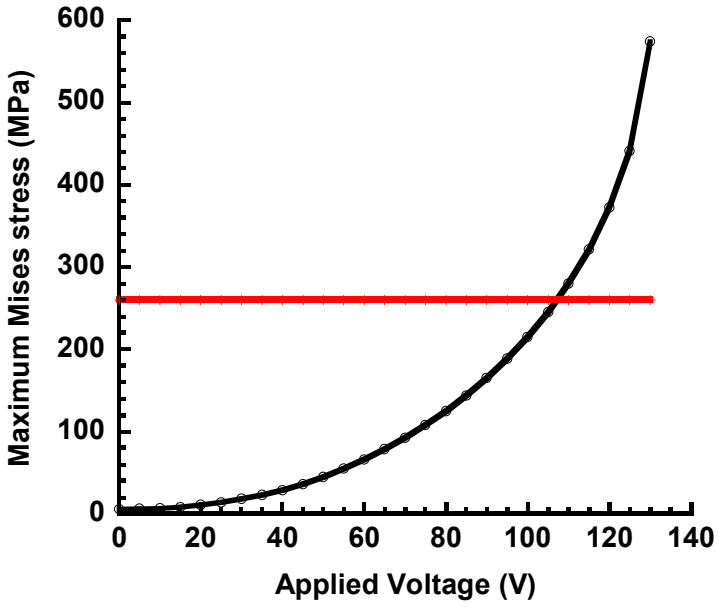

(a)

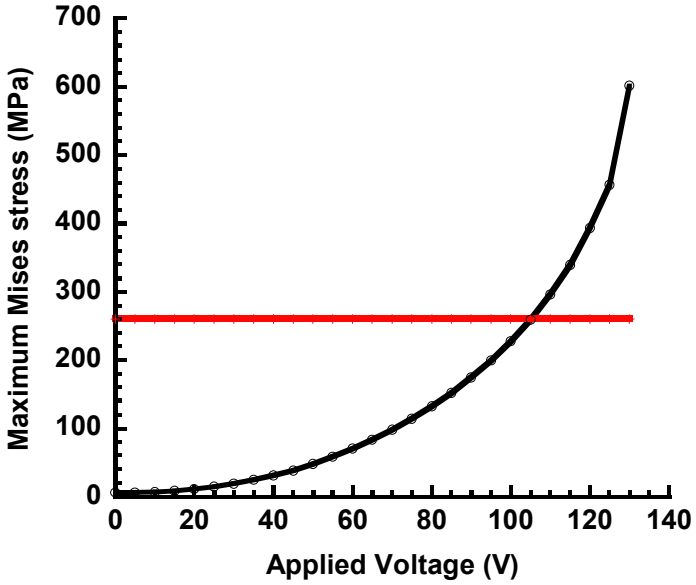

(b)

Figure 7.12 FEM analysis results of simulations carried out on devices shown in Figure 7.5(a) and (b). Von Mises stresses produced in the support Al_2O_3 layer as a function of the applied actuation voltage. (a) plain support layer and (b) corrugated support layered. The tensile strength of Al_2O_3 is 260 MPa is also shown.

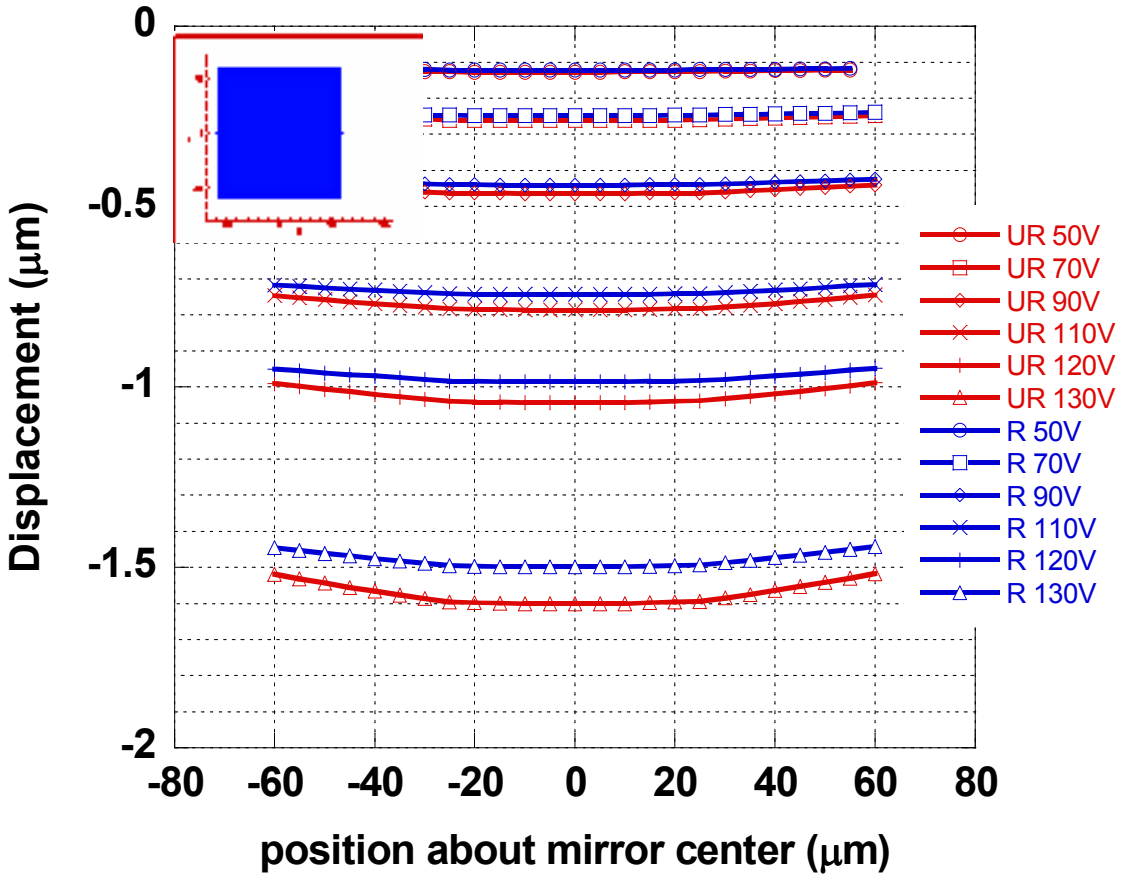

Figure 7.13 FEM analysis results of simulations carried out on devices shown in Figure 7.5(a) and (b). Flatness profile of the top reflector during deflection. Both the plain support layer (UR) and the corrugated support layered (R) devices are shown. Inset is a picture of a top reflector and the path traversed for the deflection measurement.

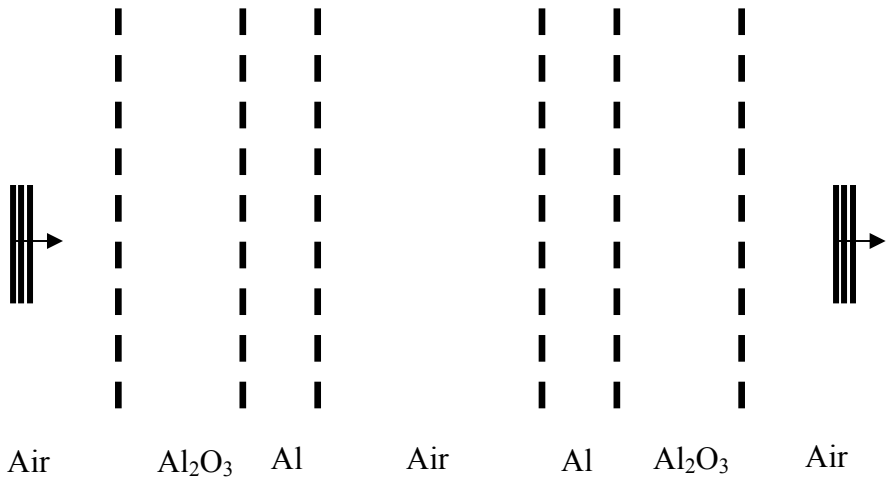

Figure 7.14. Model of Fabry Perot cavity based microspectrometer used for transmission line model.

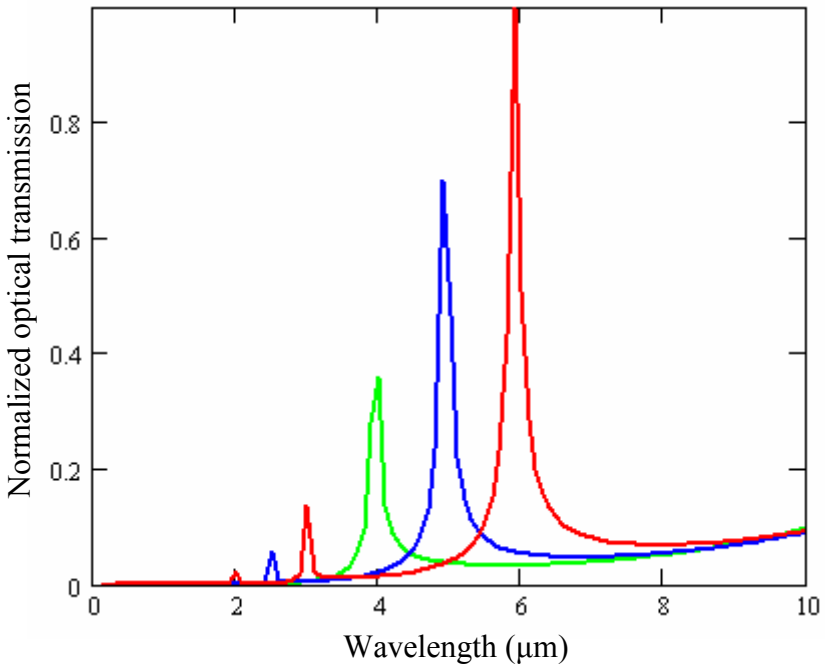

Figure 7.15. Normalized transmission through a Fabry Perot cavity at inter-reflector spacings of 2.0μm, 2.5μm and 3.0μm

for operational wavelengths around 5μm, the reflector size of 12 μm is electrically large and edge diffraction effects can be neglected[85]. It has been shown that a transmission line model based on the ABCD matrix as used here is quite accurate and agrees very well with experimental data[86].

7.6 Conclusions

The development of a tunable infrared spectrometer for near and mid infrared region application has been discussed in this chapter. A Fabry Perot cavity based design was analyzed using finite element method based simulations. The modeling was done to investigate the strength of the support layer during deflections as well as the flatness profile of the of the deflected layer. A design consisting of eight support tethers (four pairs) was found to yield a circularly symmetric deflection. The spacing of the support tethers as well as the location and size of the actuating electrodes on the deflection was also studied. IT was seen that for an inter-reflector spacing of 2.5 μm, the current design could be tuned from 3.6-5.0 μm. A transmission line model using the ABCD matrices was used to model the cavity for optical transmission.

CHAPTER 8

SUMMARY AND CONCLUSIONS

8.1 Micromachined microbolometers on flexible substrates

Micromachined microbolometers on flexible substrate have been fabricated and characterized. These detectors are supported by thin micromachined layers of silicon nitride on flexible polyimide PI5878G. This was done to investigate the feasibility of low bolometers with low thermal conductance on support membranes for potential applications in integrated sensors. The devices were characterized for R(T), TCR, responsivity, detectivity and thermal conductance.

The device had a resistance of 3.76 MΩ and a TCR of -2.63 %/K at 301K. The measured thermal conductance was $G_{th} = 5.61 \times 10^{-7}$ W/K. The device displayed a voltage responsivity of 9.2×10^2 V/W. The responsivity improved to 7.4×10^3 V/W when the same device as measured in vacuum, pointing to good thermal isolation because of the micromachining. The maximum recorded detectivity of the device was 6.6×10^5 $cmHz^{1/2}/W$. During fabrication, 500 Å $SrTiO_3$ was used as a protective layer above Si_3N_4 to protect the nitride from CF_4 using in dry etching Ti. It was seen in SEM pictures that the $SrTiO_3$ had adhesion problems and flaked off the nitride after the

micromachining. The use of $SrTiO_3$ was discontinued and in subsequent fabrication Ti was patterned using lift-off technique. The effect of substrate heating on the detector response was also investigated and found to be negligible. This becomes significant in case these detectors are employed in imaging arrays where cross talk between adjacent pixels is an undesirable property.

8.2 Device level vacuum packaged microbolometers on flexible substrates

A new device-level vacuum-packaging scheme has been introduced in this work. A preliminary design was subjected to FEM analysis to validate the structural integrity of the vacuum element. The stresses produced in the optical window forming the cavity were found to be less than the fracture strength of the ceramic material used even when the substrate is bent to a radius of 10 mm. Optical masks were fabricated based on this design to fabricate the devices. During fabrication, modifications to the initial design had to be made changing the geometry originally envisaged. The modified geometry was also subjected to FEM based structural analysis and found to be satisfactory. The complex relative permittivity of ceramic Al_2O_3 was extracted using infrared variable angle spectroscopy for wavelengths from 1μm to 39 μm. Optical transmission properties of PI5878G were also measured. The thermal conductance from the device to the ambient was calculated using an equivalent circuit and also numerically using finite element method. Devices were fabricated, packaged and characterized. DEV-R is a device-level vacuum packaged microbolometer on a rigid Si substrate while DEV-F is a similar device on polyimide. The measured TCR of the devices was -3.7 %/K and -3.4 %/K for DEV-F and DEV-R respectively. DEV-F had a

responsivity of 61.3 μA/W at a chopper frequency of 5 Hz when biased with a voltage of 10.1 V across the bolometer. DEV-R had a responsivity of 50.0 μA/W at a chopper frequency of 5 Hz when biased with a voltage of 1.5 V across the bolometer. Corresponding detectivities were $5.2\text{x}10^4$ $\text{cmHz}^{1/2}/\text{W}$ and $1.5\text{x}10^5$ $\text{cmHz}^{1/2}/\text{W}$ for DEV-F and DEV-R resspectively. The thermal conductance from the devices to the ambient was used to measure the quality of the vacuum inside the cavity. DEV-F had a measured thermal conductance $G_{th} = 3.7 \times 10^{-6}$ W/K while DEV-R had a measured thermal conductance of $G_{th} = 1.1 \times 10^{-6}$ W/K. The measured thermal conductances for the devices is lower than the theoretical value calculated with a thermal equivalent circuit. It is however comparable in magnitude. The reason for the lower value of thermal conductance for DEV-R needs to be investigated further. The resistance of these devices was also very high. The design value of the bolometer resistance was ~150 kΩ. Resistances of the same order of magnitude were measured immediately after the fabrication of the detectors. The resistance however kept increasing after the sacrificial polyimide PI2737 mesa was deposited on top of the detectors. DEV-F and DEV-R had resistances of 86.7 MΩ and 39.3 MΩ respectively. There is a likelihood, the acidic constituents in the polyimide attacked the YBCO, reducing the effective cross section of the resistor and increasing the resistance. The calculated absorptivity in the devices is 4.7 % and 7.7 % for DEV-F and DEV-R respectively. This is very low and the cavity dimensions along the optical axis need to be set so as to ensure maximum power dissipation in the detector plane. The optical transmission properties of Al_2O_3

used as the optical window also need to be determined experimentally. During fabrication n of the devices on flexible substrate, no sacrificial layer was used to facilitate removal of the flexible polyimide substrate off the silicon carrier wafer after the fabrication had been completed. It was seen that the 24 μm thick substrate polyimide became very brittle and crumbled when it was attempted to peel it off. The use of a sacrificial layer will remove this problem as it is a standard practice reported elsewhere in literature.

8.3 Tunable Fabry Perot cavity based microspectrometer

The development of a tunable infrared spectrometer for near and mid infrared region application has also been presented. A Fabry Perot cavity based design was analyzed using finite element method based simulations. The modeling was done to investigate the strength of the support layer during deflections as well as the flatness profile of the deflected layer. A design consisting of eight support tethers (four pairs) was found to yield a circularly symmetric deflection with maximum flatness for the moveable reflecting mirror. The spacing of the support tethers as well as the location and size of the fixed actuating electrodes on the deflection was also studied. It was seen that for an inter-reflector spacing of 2.5 μm, the moveable top mirror could safely be pulled down by 0.7 μm. This corresponds to a tenability from 3.6-5.0 μm. A transmission line model using the ABCD matrices was used to model the cavity for optical transmission. It was seen that the resonant wavelength of the spectrometer is a function of the inter-reflector spacing as expected.

Masks have been fabricated and the fabrication of these spectrometers is underway. This will be followed by characterization of the spectrometers using a pyroelectric detector.

APPENDIX A

RADIUS OF CURVATURE OF A THIN STRIP SQUEEZED AT THE ENDS

Radius of curvature of a thin strip being squeezed in at two opposite ends

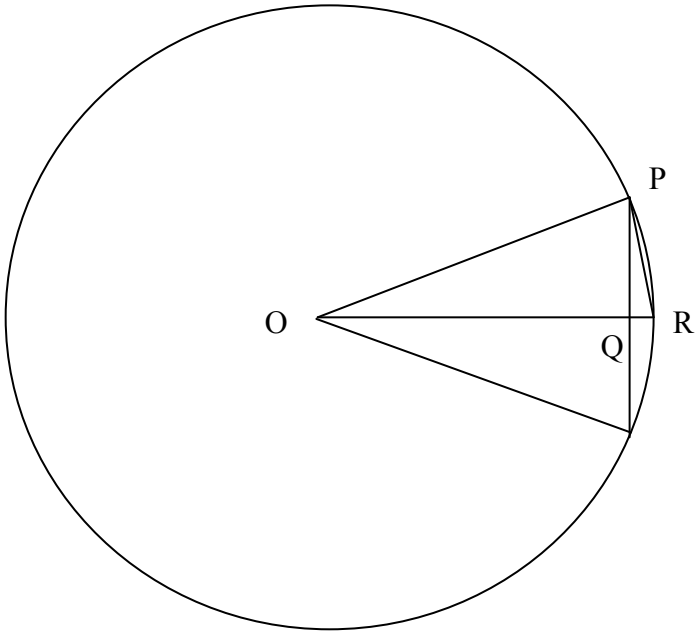

In ΔPQR

$$\overline{PQ} = \frac{length}{2} - U_y$$

where $length$ is the length of device (~ 800 um in this simulation) and U_y is the inward displacement of the edge.

$$\overline{PR} = \sqrt{\overline{PQ}^2 + \overline{QR}^2} = \sqrt{(\frac{length}{2} - y)^2 + U_z^2}$$

$$< QPR = \tan^{-1}(\frac{\overline{QR}}{\overline{PQ}}) = \tan^{-1}(\frac{U_z}{\frac{length}{2} - U_y})$$

$$< QRP = 90 - < QPR \quad :: \qquad < PQR = 90^\circ$$

In ΔOPR

Using the sine law

$$\frac{\overline{PR}}{\sin(< POR)} = \frac{\overline{OP}}{\sin(< ORP)} = \frac{\overline{OR}}{\sin(< OPR)}$$

$< ORP =< QRP$ in ΔOPR and ΔQRP respectively.

Therefore the radius of curvature "r" of the bent strip is

$$r = \overline{OR} = \overline{OP} = \overline{PR}\frac{\sin(< QRP)}{\sin(< POR)}$$

REFERENCES

1 K. Bock, "Polytronics-Electronics and Systems on Flexible Substrates", 2005 IEEE VLSI-TSA. International Symposium on VLSI Technology (VLSI- TSA-TECH) Piscataway, NJ, USA, pp. 53-56, 2005.

2 J. W. Balde (Ed.), Foldable Flex and Thinned Silicon multichip packaging technology, Kluwer Academic publishers for IMAPS (Worwell 2002), pp. 106-114.

3 C. Landesberger et. al., "New dicing and thinning concept improves mechanical reliability of ultra thin Silicon," Proc. International Symposium on Advanced Packaging Materials Processes, Properties and Interfaces 2001, pp. 92-97, 2001.

4 www.newscientist.com/article.ns?id=dn4602, Jan 2004

5 T.F. Waris, R. Saha, and J.K. Kivilahti, "Manufacturing and reliability of flexible integrated module boards," Proc. POLYTRONIC 2002. *2nd* International IEEE Conference on Polymers and Adhesives in Microelectronics and Photonics, pp. 73-77, 2002.

6 P. Salonen and J. Rantanen, "A Dual-Band and Wide-Band Antenna on Flexible Substrate for smart clothing," Proc. The 27th Annual Conference of the IEEE industrial electronics society, IECON '01 vol. 1, pp. 125 -130, 2001.

7 T. Steiglitz, M. Schuettler and K. P. Koch, "Implantable biomedical Microsystems for neural prostheses – Flexible, Polyimide-Based and Modular", IEEE Engineering in Medicine and Biology magazine, Vol. 24, Issue 5, pp. 58- 65, Sept.-Oct. 2005.

8 N. Alteheld, G. Roessler, M. Vobig and, P. Walter, "The retina implant – a new approach for a visual prosthesis," Biomed. Technol., vol. 49, no. 4, pp. 99-103, April 2004.

9 T. Steiglitz and J. -U. Meyer, "Microtechnical interfaces to neurons", in Topics in Current Chemistry Series, Microsystem Technology in Chemistry and Life Science, A. Manz and H. Becker Eds., Berlin: Springer 1998, vol. 194, pp. 131-162.

10 P. Heiduschka and S. Thanos, "Implantable bioelectronic interfaces for lost nerve functions," Progress in neurobiology, vol. 55, no. 5, pp 433-461, 1998.

11 W.L.C. Rutten, "Selective electrical interfaces with the nervous system," Annu. Rev. Biomed. Eng., vol. 49, No. 4, pp. 20-25, April 2004.

12 P. J. Rousche, D. S. Pellinen, D. P. Pivin Jr. J. C. Williams, R. J. Vetter and D. R. Kipke, "Flexible polyimide-based intracortical electrode arrays with bioactive capability," IEEE Trans. Biomed. Eng., vol. 48, no. 3, pp. 361-371, March 2001.

13 H. Takahashi, T. Ejiri, M. Nakao, N. Nakamura, K. Kaga and T. Herve, "Microelectrode array on folding polyimide ribbon for epidural mapping of functional evoked potentials," IEEE Trans. Biomed. Eng., vol. 50, no. 4, pp. 510-516, April 2003.

14 H. Saito, K. Hoshino, K. Matsumoto and I. Shimoyama, "Compound eye shaped flexible organic image sensor with a tunable visual field," Proc. 18th IEEE International Conference on Micro Electro Mechanical Systems, pp. 96-99, 2005.

15 A. Tognetti, F. Lorussi, M. Tesconi, D. De Rossi, "Strain sensing fabric characterization," Proc. IEEE Sensors 2004, vol.1 ,Oct. 24-27, pp.527 – 530, 2004.

16 B. Majeed, J. –B. V. S. Jans, I. Paul, J. Barton, S. C. O'Mathuna, K. Delany , "Material characterisation and process development for miniaturized wireless sensor network module," Research in Microelectronics and Electronics. 2005, vol. 1, Jul. 25-28, 2005, pp. 237–240, 2005.

17 J. Sinius, R. Gaska, M. S. Shur, "Flexible semiconductor films for sensitive skin", Proc. 2000 IEEE/RSJ International Conference on Intelligent Robots and Systems (IROS 2000), vol.2, pp. 1511-15, 2000.

18 B. Sadeghi Makki, M. Moradi, A. Moafi, S. Mohajerzadeh, B. Hekmatshoar, and D. Shahrjerdi, "Fabrication of poly-Ge-based thermopiles on plastic" IEEE Sensors Jnl., vol.4, no.6, pp. 743-8, Dec. 2004.

19 N. Chen, J. engel, J. Chen, Z. Fan, C. Liu, "Micromachined thermal imaging mesh for conformal sensing system," 4th IEEE international conference on sensors, Irvine, Calfornia, October 31-November 1, 2005.

20 V. K. Kapur, A. Bansal, P. Le and O. Asensio, "Non-vacuum printing process for CIGS solar cells on rigid and flexible substrates", Conference Record of the Twenty-Ninth IEEE Photovoltaic Specialists Conference 2002, pp. 688-91, 2002.

21 A. F. Hepp, "Multi-junction thin-film solar cells on flexible substrates for space power," 37th Intersociety Energy Conversion Engineering Conference (IECEC'02), 2002, p.197, Jul. 29-31, 2004.

22 G. Dennler, N. S. Sariciftici, "Flexible conjugated polymer-based plastic solar cells: From basics to applications" Proc. of the IEEE, vol. 93, no.8, pp. 1429-39, Aug. 2005.

23 D. J. Hoffman, T. W. Kerslake, A. F. Hepp, A. F. Jacobs, M. K. Ponnusamy, "Thin-film photovoltaic solar array parametric assessment," Collection of Technical Papers. 35th Intersociety Energy Conversion Engineering Conference and Exhibit (IECEC) 2000, vol.1, pp. 670-80, 2000.

24 A. Yaradanakul, D. P. Butler and Z. Celik-Butler, "Uncooled Infrared Microbolometers on a Flexible Substrate", IEEE Transactions on Electron Devices, **49**, pp. 930-933, 2002.

25 A. Yildiz, Z. Celik-Butler and D. P. Butler, "Microbolometers on a Flexible Substrate for Infrared Detection", IEEE Sensors Journal, **4**, pp. 112-117, 2004.

26 S. A. Dayeh, D. P. Butler, Z Çelik-Butler, "Micromachined infrared bolometers on flexible polyimide substrates," Sensors and Actuators A, vol. 118, pp. 49-56, 2005.

27 A. Mahmood, S. A. Dayeh, D. P. Butler, and Z. Çelik-Butler, "Micromachined infrared sensor arrays on flexible polyimide substrates", Proc. IEEE Sensors Conference, vol. 2, pp. 777 – 782, October, 2003.

28 A. Mahmood, D. P. Butler, and Z. Çelik-Butler, "Micromachined bolometers on polyimide", Sensors and Actuators A, accepted for publication.

29 E.L. Dereniak, G.D. Boreman, Infrared Detectors and Systems, John Wiley & Sons Inc. New York, 1996.

30 S. A. Dayeh, D. P. Butler, Z Çelik-Butler, "Micromachined infrared bolometers on flexible polyimide substrates," Sensors and Actuators A, vol. 118, pp. 49-56, 2005.

31 A. Yildiz, Z. Celik-Butler and D. P. Butler, "Microbolometers on a Flexible Substrate for Infrared Detection", IEEE Sensors Journal, **4**, pp. 112-117, 2004.

32 A. Yaradanakul, D. P. Butler and Z. Celik-Butler, "Uncooled Infrared Microbolometers on a Flexible Substrate", IEEE Transactions on Electron Devices, **49**, pp. 930-933, 2002.

33 P. W. Kruse, D. D. Skatrud, "Uncooled infrared imaging arrays and systems; Semiconductors and semimetals vol. 47,"Academic Press, San Diego, CA 1997.

34 P. C. Shan, Z. Celik-Butler, D. P. Butler and A. Jahanzeb, "Semiconducting YBaCuO thin films for uncooled infrared bolometers", Jnl. of Applied Physics, **78** (12) pp 7334-7339, 1995.

35 P. C. Shan, Z. Celik-Butler, D. P. Butler, A. Jahanzeb, C. M. Travers, W. Kula and R. Sobolewski, "Investigation of semiconducting YBaCuO thin films: A new room temperature bolometer", Journal of Applied Physics, **80** (12) pp 7118-7123, 1996.

36 S. Mathews, "Thermal imaging on the rise", Laser Focus World, March 2004

37 W. Radford, D. Murphy, M. Ray, S. Propst, A. Kennedy, J. Kojiro, J. Woolayaw and K. Soch, R. Coda, G. Lung, E. Moody, D. Gleichman, and S. Baur, "320x240 Silicon Microbolometer Uncooled IRFPAs With On-Chip Offset Correction", SPIE, Vol. 2746, pp. 82-93, 1996.

38 B.E. Cole, R. E.. Higashi, and R. A. Wood, "Monolithic Arrays of Micromachined Pixels for Infrared Application," IEEE Proc. International Electron Devices Meeting, pp. 459-462, 1998.

39 T. Breen, N. Butler, M. Kohin, C. A. Marshall, R. Murphy, T. Parker, R. Silva, "More Applications of Uncooled Microbolometer Sensors," SPIE, vol. 3436, pp. 530-540, 1998.

40 B. Meyer, R. Cannata, A. Stout, A. Gin, and P. Taylor, "Amber's Uncooled Microbolometer LWIR Camera," SPIE, vol. 2746, p. 13, 1996.

41 P. W. Kruse, D. D. Skatrud, "Uncooled Infrared Imaging Arrays and Systems," Semiconductors and Semimetals, vol. 47, pp. 43-121, Academic Press, New York, 1997.

42 R. A. Wood, "Use of Vanadium Oxide in Microbolometer Sensors," Patent No. 5450053, 1993.

43 R. A. Wood, "Use of Vanadium Oxide in Microbolometer Sensors," Patent No. Re.36615, 1997.

44 R. E. Higashi, "Thermal Sensor and Method of Making same," Patent No. 6144285, 2000.

45 N. R. Butler, "Ambient Temperature IR Focal Plane Arrays," *SPIE*, vol. 4028, pp. 58-65, 2000.

46 J. Brady, T. Schimert, D. Ratcliff, R. Gooch, B. Ritchey, P. McCardel, K. Rachels, S. Ropson, M. Wand, M. Weinstein, and J. Wynn, "Advances in Amorphous Silicon Uncooled IR Systems," SPIE, vol. 3698, pp. 161-167, 1999

47 T. Schimert, D. Ratcliff, J. Brady, S. Ropson, R. Gooch, B. Ritchey, P. McCardel, K. Rachels, M. Wand, M. Weinstein, and J. Wynn, "Low Cost, Low Power Uncooled a:Si Based Micro Infrared Camera for Unattended Ground Sensor Applications," SPIE, vol. 3713, pp. 101-111, 1999.

48 C. Vedel, J. L. Martin, J. L. Ouvrier Buffet, J. L. Tissot, M. Vilain, and J. J. Yon, "Amorphous Silicon Based Uncooled Microbolometer IRFPA," SPIE, vol. 3698, pp. 276-283, 1999.

49 W. Radford, R. Wyles, J. Wyles, J. Varesi, M. Ray, D. Murphy, A. Kennedy, A. Finch, E. Moody, F. Cheung, R. Coda, and S. Baur, "Microbolometer Uncooled Infrared Camera with 20 mK NETD," SPIE, vol. 3436, pp. 636-645, 1998.

50 S. Sedky, P. Fiorini, K. Baert, L. Hermans, and R. Mertens, "Characterization and Optimization of Infrared Poly SiGe Bolometers," IEEE Transactions on Electron Devices, vol. 46, p. 675-682, 1999.

51 M. S. Liu, J. S. Haviland and C. J. Yue, "Integrated Infrared Sensitive Bolometers," Patent No. US005260225A, 1992.

52 P. Fiorini, S. Sedky, M. Caymax and C. Baert, "Method of Fabrication of an Infrared Radiation Detector and Infrared Detector Device," Patent No. US009194722B1, 2001.

53 J. Wauters, Doped Silicon Creates New Bolometer Material," Laser Focus World, pp. 145-149. 1997.

54 A. Tanaka, S. Matsumoto, N. Tsukamoto, and N. Teranishi, "Silicon IC Process Compatible Bolometer Infrared Focal Plane Array," 8th International Conference

on Solid-State Sensors and Actuators, and Eurosensors IX. Stockholm, Sweden, June 25-29, 1995.

55 M. V. S. Ramakrishna, G. Karunasiri, U. Sridhar, and G. Chen, "Performance of Titanium and Amorphous Germanium Microbolometer Infrared Detectors," SPIE, vol. 3666, pp. 415-420, 1999.

56 R. B. Lee III, B. R. Barkstorm, H. C. Bitting, D. A. H. Cormmelynck, J. Paden, D. K. Pandey, K. J. Priestley, G. L. Smith, S. Thomas, K. L. Thornhill, and R. S. Wilson, "Prelaunch Calibrations of the Clouds and the Earth's Radiant Energy System (CERES) Tropical Rainfall Measuring Mission and Earth Observing System Morning (EOS-AM1) Spacecraft Thermistor Bolometer Sensors," IEEE Transactions on Geoscience and Remote Sensing, vol. 36, pp. 1173-1185, July 1998.

57 P. Eriksson, j. Y. Andersson, and G. Stemme, "Thermal Characterization of Surface-Micromachined Silicon Nitride Membranes for Thermal Infrared Detectors," IEEE Jnl. of Microelectromechanical Systems, vol. 6, pp. 55-61, 1997.

58 J. S. Shie, Y. M. Chen, M. O. Yang, and B. C. S. Chou, "Charaterization and Modelling of Metal-Film Microbolometer," IEEE Journal of Microelectromechanical System*s,* Vol. 5, No. 4, December 1996.

59 P. R. Gray, P. J. Hurst, S. H. Lewis, R. G. Meyer, Analysis and Design of Analog Integrated Circuits, John Wiley & Sons Inc., New York, 2001.

60 N. Chen, J. Engel, J. Chen, Z. Fan, C. Liu, "Micromachined thermal imaging mesh for conformal sensing system," 4th IEEE international conference on sensors, Irvine, Calfornia, October 31-November 1, 2005.

61 S. Wolf and R. N. Tauber, "Silicon Processing for the VLSI Era, Volume 1 – Process Technology", 2nd ed., Lattice press, Sunset Beach, CA, 2000.

62 R.R. Tummala, Fundamentals of Microsystems packaging, New York, McGraw-Hill, 2001.

63 K. Gilleo, Area Array Packaging Handbook, New York, McGraw-Hill, 2002.

64 B. Lee, S. Seok and K. Chun, "A study on wafer level vacuum packaging for MEMS devices," Jnl. Micromech. Microeng., vol. 13, pp. 663-669, 2003.

65 Y. -T. Cheng, H. Wan-Tai, K. Najafi, C. T.-C. Nguyen and L. Lin, "Vacuum Packaging Technology Using Localized Aluminum/Silicon-to-Glass Bonding," IEEE/ASME J. Microelectromech. Syst., vol. 11, no. 5, pp. 556-565, 2002.

66 H. Clearfield, J. young, S. Wijeyeskera, and L. Logan, "Wafer-Level Chip Scale Packaging: Benefits for integrated passive devices." IEEE Transactions, Advanced Packaging, 2000.

67 S. Denda and S. Otake, "Wafer level packaging technology in Japan," Proceedings of the IEMT/IMC symposium. Omiya, Japan, 2000, pp. 4-9.

68 P. Elenius, "Wafer-level packaging gains momentum" Solid state technology, pp 45, April 1999,.

69 P. Elenius, S. Barrett and T. Goodman, "Ultra-CSP—A wafer level package" IEEE Transactions, Advanced Packaging, pp. 220, 2000.

70 Elshabini-Riad, ed. "High density thin film packaging: Materials, Processes and Applications," Handbook of Thin Film Technology, New York: McGraw- Hill, 1998.

71 P.E. Garrou, "Wafer level chip scale packaging (WL-CSP): An overview." IEEE Transactions, Advanced Packaging, Vol. 23, 2000, pp. 198.

72 P.E. Garrou, "Wafer level packaging has arrived" Semiconductor International, Vol. 23, Oct 2000, pp. 119.

73 P.E. Garrou and I. Turlk eds MCM-D, Thin film materials, Processes and applications. New York: McGraw-Hill, 1998.

74 T. W. Goodman, R.T. Crowley and J.E. Vardaman, "Chip size packages: Comparisons and structure performance relationships," Proceedings of the 9th international Microelectronics conference, Omiya, Japan, 1996, 62.

75 www.crystran.co.uk

76 J. Shelby, Handbook of gas diffusion in solids and melts, ASM international, Materials Park OH, 44073

77 M. Aguilar-Frutis, M. Garcia, C. Falcony, G. Plesch and S. Jimenez-Sandoval, A study of the dielectric characteristics of aluminum oxide thin films deposited by

spray pyrolysis from Al(acac)3, Thin Solid Films, vol. 389, No. 1-2 (2001) 200 206.

78 www.almazoptics.com

79 J. F. Shackelford (ed.), W. Alexander (ed.), CRC Materials science and engineering handbook, 3rd Edition, CRC press Boca Raton, 2001.

80 J.P. Rice, E. N. Grossman, L. J. Borcherdt, and D. A. Rudman, "Higher T_c superconducting antenna-coupled microbolometer on silicon," Proc. SPIE vol. 2159, pp 98-109, 1994.

81 D. M. Pozar, Microwave Engineering, 2nd ed., John Wiley and Sons Inc., New York NY 2001.

82 C. A. Balanis, Advanced Engineering Electromagnetics, John Wiley and Sons Inc., New York 1989.

83 B. E. A. Saleh and M. C. Teich, Fundamentals of Photonics, John Wiley and Sons Inc., New York 1991.

84 J. H. Weaver, C. Krafka, D. W. Lynch, E.E. Koch, Optical properties of metals, Pt I and II, Fachinformationzentrum Energie, Physik, Mathematic, GMBH, Karlsruhe (1981).

85 A. Mahmood, "Electromagnetic scattering analysis of three dimensional structures using physical optics," MSEE dissertation, UET Lahore Pakistan 1999.

86 Y. Kim, "Application of micromachining techniques for Fabry-Perot cavity based microsensors", Ph.D. dissertation, University of Texas at Austin, August 1995.

BIOGRAPHICAL INFORMATION

Aamer Mahmood was born in Pakistan in 1970. He got a BE degree in electrical engineering from N-W.F.P. University of Engineering and Technology, Peshawar, in 1992. He got an MS degree in electrical engineering from the University of Engineering and Technology, Lahore in 1999. He completed his Ph.D. in electrical engineering from the University of Texas at Arlington, USA, in August 2006.

He has worked in industry in Pakistan and his graduate and professional experience spans the areas of electromagnetic scattering, optical and optoelectromechanical MEMS sensors development.